RCA Review

June 1973 Volume 34 No. 2
RCARCI 34(2) 215-382 (1973)

RCA Review, published quarterly in March, June, September and December by RCA Research and Engineering, RCA Corporation, Princeton, New Jersey 08540. Entered as second class matter July 3, 1950 under the Act of March 3, 1879. Second-class postage paid at Princeton, New Jersey, and at additional mailing offices. Effective Jan. 1, 1971, subscription rates as follows: United States and Canada: one year $6.00, two years $10.50, three years $13.50; in other countries, one year $6.40, two years $11.30, three years $14.70. Single copies (except for special issues) up to five years old $3.00.

RCA Review

A technical journal published quarterly
by RCA Research and Engineering
in cooperation with the subsidiaries
and divisions of RCA.

Contents

June 1973 Volume 34 Number 2

ferences in the performance–cost requirements for such a camera in the consumer, commercial, and military markets. However, the fundamental concepts developed in the evaluation of single-tube color-camera systems described in this paper may be successfully applied to each of these areas when considered within the context of the specific application.

The objective of the single-tube stripe-color TV camera research program was to evaluate color-encoding techniques and to provide experimental and theoretical data regarding system performance characteristics in support of various programs involved in adapting such systems to specific applications. This paper summarizes the performance evaluation of four such systems.

2. Stripe-Color Spatial Encoding Background

The basic techniques for color-encoded pictures are (1) spatial or area sharing of chrominance and luminance information, (2) time multiplexing, (3) line and frame sequential systems, and (4) combinations of space and time sharing. While all these approaches are potentially useful for encoding color images on a monochromatic medium or pickup device, the desire for a system that inherently eliminates such problems as color breakup and flicker, registry of multiple images, stability, and equipment complexity has led to the use of area-shared (stripe-color filters) techniques.

The stripe-color-encoded single-frame systems may be divided into two general categories. One category involves phase modulation of the color information on a suitable reference subcarrier with an accompanying index signal, while the other category employs amplitude modulation of multiple subcarriers to encode the chrominance information. Amplitude-modulated carrier systems place considerably less stringent requirements on fabrication tolerances and the stability of scan size and linearity.

The basic stripe-color-encoding system involves a set, or sets, of stripe spatial filters interposed in the optical path between the object and the target of a TV pickup device. The stripe filter is either placed or imaged at the plane of the photosensitive target of the pickup device. The video output consists of a baseband signal and a subcarrier, or subcarriers, with attendant modulation sidebands resulting from the electron beam scanning the spatial image of the stripe filters superimposed upon the image of the object scene. The output signal is electronically decoded to recover the color modulation sidebands of the spatially generated carriers and matrixed with the low-frequency baseband components to form the red, green, and blue signals to feed a conventional color viewing system. A variety of stripe color filter designs and appropriate decoding techniques are possible. Four such systems are described, and evaluation data is presented as to colorimetry, signal-to-noise ratio, available bandwidth (resolution), decoding circuitry complexity, stripe-filter type and complexity, light sensitivity, spot focus requirements, intermodulation products, and optics. For convenience, these systems are referred to as stripe-color amplitude-modulation systems I, II, III, and IV. An amplitude-modulation system already in commercial production, referred to as the Kell/SRI system,[1,8,9] was used as a benchmark for the basis of comparison.

3. Experimental Setup

Stripe-color-encoding principles are adaptable to most raster scanned light sensors. For this study, the standard 8507A one-inch, separate mesh, antimony trisulfide (Sb_2S_3) vidicon was chosen as the common pickup device for encoding-systems comparisons. A relay otpical system afforded a high degree of flexibility in evaluating a variety of systems and was adopted as part of the experimental setup.

In addition to theoretical analysis and computer programs relating to colorimetry and signal-to-noise characteristics, it is appropriate to actually assemble representative systems to provide both experimental and subjective evaluations. The test facilities consisted of the following functions and apparatus as shown in Fig. 1:

1. An 8507A vidicon camera chain with appropriate drive circuitry.
2. An optical bench including a calibrated light box, slide projector, a relay-optical system, stripe filter holders, vibrating optical filter, and camera system.
3. A receiver/monitor system consisting of a 21-inch color viewer requiring red, green, and blue signal inputs, a 10-inch wideband monochrome monitor, a standard NTSC color signal decoder and a monitor r-f/i-f receiver for off-the-air signals.
4. A transmitter system consisting of a TG-3 sync generator with color signal accessories, a TG-4 color bar generator and NTSC encoder, and an rf signal generator.
5. A Processor–Decoder–Matrix (PDM) system consisting of a single-channel variable linearizer unit, a three-channel fixed-gamma reinsertion unit, and a variety of special stripe-filter decoder-matrix units representative of the systems being tested.

6. Special signal measuring facilities including waveform monitors, vectorscope, spectrum analyzer, noise-measuring apparatus, frequency counter, signal generator, and oscilloscopes.

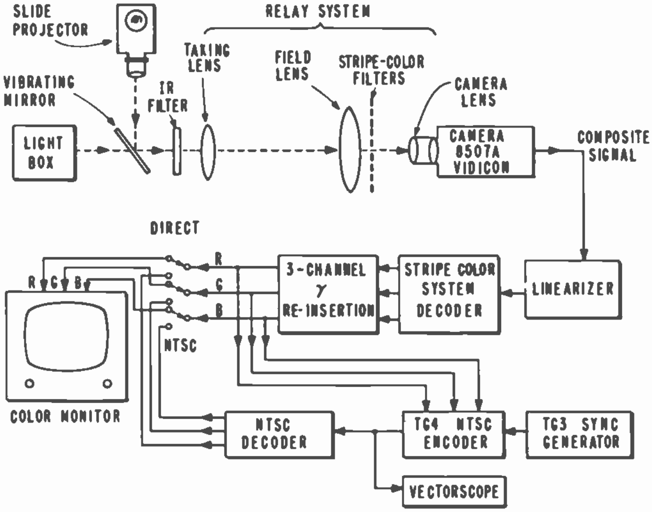

Fig. 1—Stripe-color-encoding test setup.

In the interest of consistency, the same camera system (GPL 1000) and the same vidicon (8507A) was used for all system comparative tests. The tungsten light source was corrected with IR-rejecting filters to represent a source equivalent to 6500°K (Fig. 2). Variations of light intensity were accomplished either by means of an iris or by introducing the appropriate neutral density filters. The relay optical system, which consisted of a taking lens, a six-inch diameter field lens, and a 55 millimeter camera lens, was adjustable over an intermediate image size of from 1.5 × 1.5 inches to almost 3 × 3 inches. Thus, the same stripe-color filters could be used over a wide range of spatial frequencies depending upon the intermediate image size chosen. Since the filters were on individual glass substrates they could be independently rotated to the desired angular position with respect to the vertical axis of the optical system. The same yellow–clear and cyan–clear filters were used for all system comparison tests. The filters were 100 lpi and were purchased from an outside vendor (see Fig. 3 for spectral characteristics). A third magenta–clear stripe-color filter, fabricated at RCA Laboratories, was included for three-color systems tests (see Fig. 4) and was supplied at 87.5, 100 and 125 lpi.

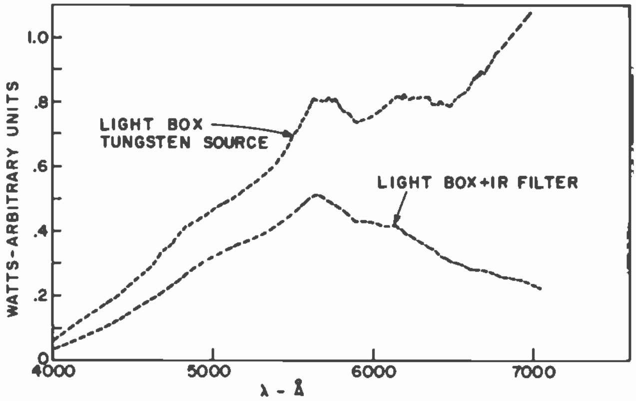

Fig. 2—Light-source spectral characteristic.

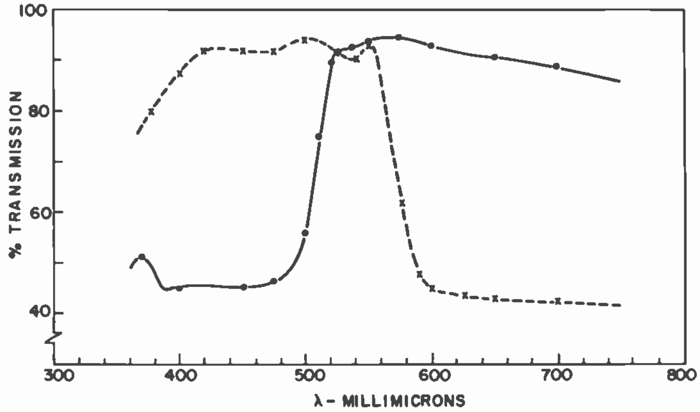

Fig. 3—Stripe-color-filter spectral characteristics (cyan-clear and yellow-clear).

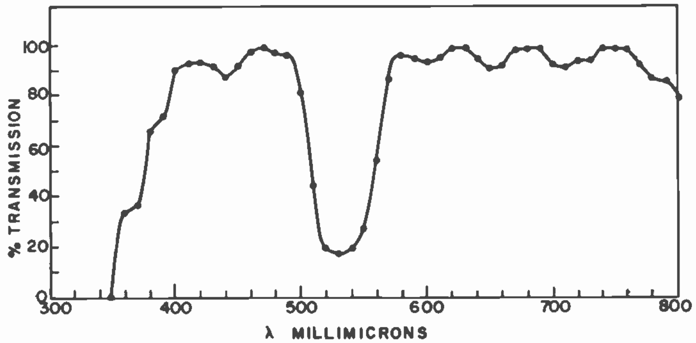

Fig. 4—Typical spectral characteristic for magenta-clear stripe filter.

The camera lens has an *F* stop range of from *F*3.5 to *F*32 and was capable of imaging the superimposed object image and stripe-filter plane on the vidicon photosensitive target in the conventional ½ × ⅜ inch raster size.

4. Basic System Considerations

4.1 Gamma

The 8507A vidicon chosen for the evaluation tests has a nonlinear light input to signal output transfer function with an average gamma of 0.65. The actual gamma varies and has been found to be in the range of 0.5 to 0.8. Since the effects of the overall gamma characteristic of a system is an important factor in determining system performance, the following signal-processing approach was taken to best facilitate individual system measurement. The composite signal from the vidicon, after amplification and frequency compensation, was passed through a transfer-function "linearizer" unit that corrected the signal to a gamma of unity over a contrast range of at least 10 to 1 (see Fig. 5). The signal may therefore be decoded and matrixed in linear circuits to produce red, green, and blue output signals in linear form. A three-channel gamma-reinsertion unit with matched characteristics was used in the red, green, and blue channels prior to feeding the viewing monitor in order to restore the appropriate overall light-in-to-light-out transfer function. This experimental approach allowed the greatest flexibility in signal processing with a minimum of intermodulation products being generated and with optimum colorimetry performance characteristics.

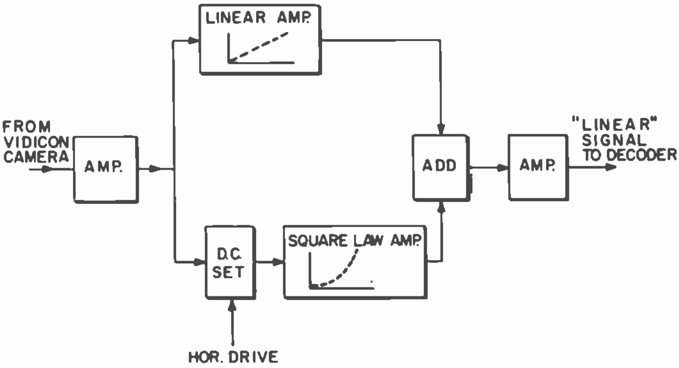

Fig. 5—Linearizer circuit.

The linearizer circuit uses the square-law characteristic of an FET in one channel that is operated in parallel with a linear amplifier channel. By combining the outputs of the two channels, the linearizer overall transfer function exponent may be adjusted between the limits of 1.0 and 2.0; the break point can also be adjusted depending on the point to which picture "black" is set on the FET operating characteristic.

The three-channel gamma-reinsertion amplifier employs a conventional dc restorer and a two-diode, adjustable-break-point, nonlinear circuit operating over a 10 to 1 gain ratio. The gamma value was adjusted to approximate a typical value of about 0.5, and the three channels were matched to within about 1% over the 10 to 1 operating range.

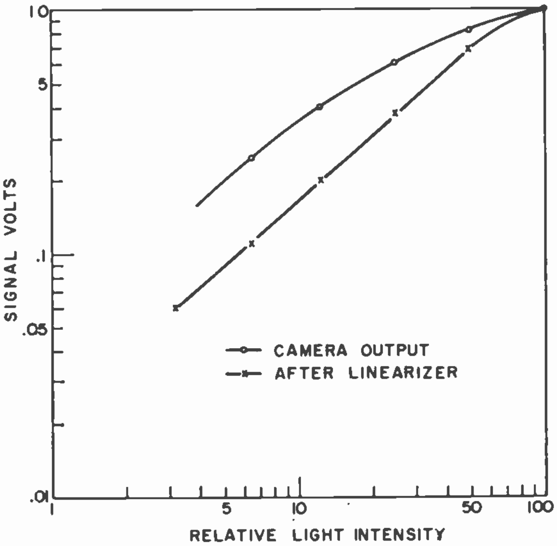

Fig. 6—Camera and linearizer gamma characteristics.

Fig. 6 indicates the measured gamma characteristic of the vidicon used for the tests, as well as the output of the composite-signal linearizer prior to the decoding process. The slight deviation from constant gamma at the highlight end of the range results from the compromise necessary in vidicon beam adjustment to obtain optimum spot focus. The individual systems being evaluated treat the final output color signals differently with respect to overall effective transfer function characteristics, and are discussed later in more detail.

4.2 Resolution

Figs. 7 and 8 are photographs taken from a line-selector oscilloscope indicating the center and corner resolution of the combination of the relay optical system and the particular vidicon camera used for the system tests. Fig. 9 is a modulation-transfer-function curve plotted from this data. The limiting resolution is about 650 TV lines in the center and about 575 TV lines in each of the four corners.

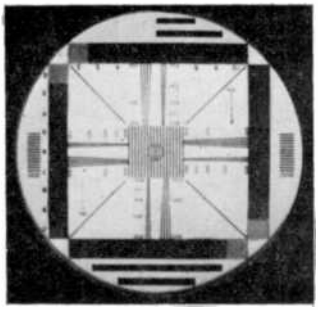

TEST PATTERN

200 LINES - 400 LINES

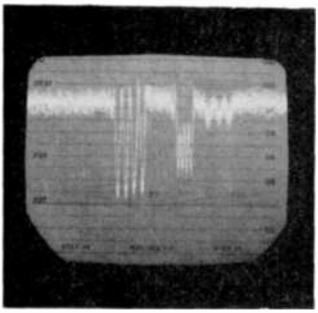

250 LINES - 500 LINES

300 LINES - 600 LINES

Fig. 7—Center resolution of camera used for tests.

The preamplifier amplitude-versus-frequency response was flat to between 6 and 7 MHz (550 to 600 TV lines)* with approximately a 6-dB-per-octave roll-off thereafter. (An exception to this case is described in detail in the section on signal-to-noise measurement.) The post-amplifier response was adjusted to provide overall flat amplitude response, up to about 6 MHz, from input light to output signal voltage by observing the test pattern response on a wide-band monochrome

---

* 80 TV lines = 1 MHz.

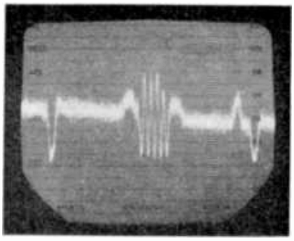

300 LINES

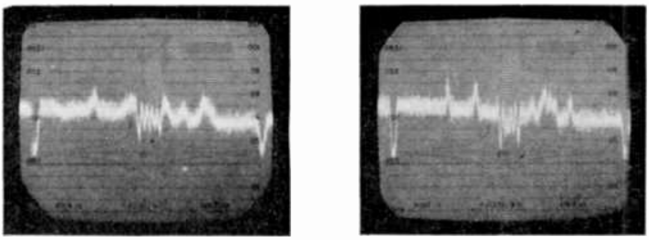

400 LINES

500 LINES

Fig. 8—Corner resolution (4 corners alike) of camera used for tests.

monitor and by measurement with the line-selector oscilloscope. The composite signal linearizer unit was also flat to at least 6 MHz, so that the final picture resolution was determined by the limitations of the bandwidth of the luminance channel of the particular color system being evaluated.

The overall chrominance channel resolution was 500 kHz at the half-power response point and was maintained the same for all systems being tested.

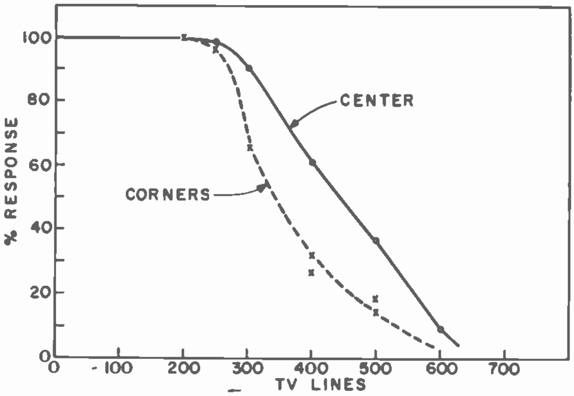

Fig. 9—Camera MTF curves.

4.3 Signal-to-Noise

The signal-to-noise ratio was measured for all systems tested at the individual red, green, and blue outputs of the decoder prior to gamma reinsertion. The following procedure was used in all cases: The signal to be measured was observed with the line-selector oscilloscope to eliminate shading and hum variations. The peak-to-peak signal was measured from picture black (or from setup, if any) to picture white. The peak-to-peak noise variations were observed by taking the highest value that occurred more than once in a time period of at least one minute. Since the signal at this point was linear, the noise could be measured at any signal pedestal level, but the data was usually taken at about midway in the range between black and white. The signals at this point consisted of the individual color low frequencies up to 500 kHz and luminance mixed highs above 500 kHz. A standard IRE roll-off characteristic filter (20 dB rejection at 3.6 MHz) was always inserted and used as a standard pass-band-measuring characteristic. The peak-to-peak noise was divided by a factor of six to convert to rms values. The ratio of peak-to-peak signal to rms noise was computed and expressed in dB as a measure of the signal-to-noise ratio.

The initial noise characteristic spectrum of the vidicon plus the preamplifier and of the postamplifier units were measured with a selective microvoltwetr and is shown in Figs. 10(a) and 10(b).

The crominance information is carried by the modulation sideband components of amplitude modulated high-frequency subcarriers in all the systems tested. The chrominance information is recovered by detection and band limiting to about 500 kHz. Thus, the high-frequency noise in the video spectrum at the subcarrier frequency is converted to relatively low-frequency noise and becomes subjectively the major contributor to the overall noise as observed in the pictures.

A Percival coil was used in an effort to improve the high-frequency signal-to-noise ratio *(above the 1/f noise range)*.[1,8,9] In this technique, a tuned coil is used in conjunction with the preamplifier input capacitance to boost the signal response at a frequency slightly higher than that of the highest subcarrier. Thus, the signal level is increased prior to the addition of noise from the first preamplifier input circuit. Care must subsequently be taken to correct the frequency and phase response at a later stage in the preamplifier.

Fig. 11 is a diagram of the circuit used, and the frequency-versus-amplitude curves indicate the degree of signal increase at 5 MHz and the degree of compensation obtained. An improvement in signal-to-noise ratio of about 6 dB was measured by "A" (with the Percival

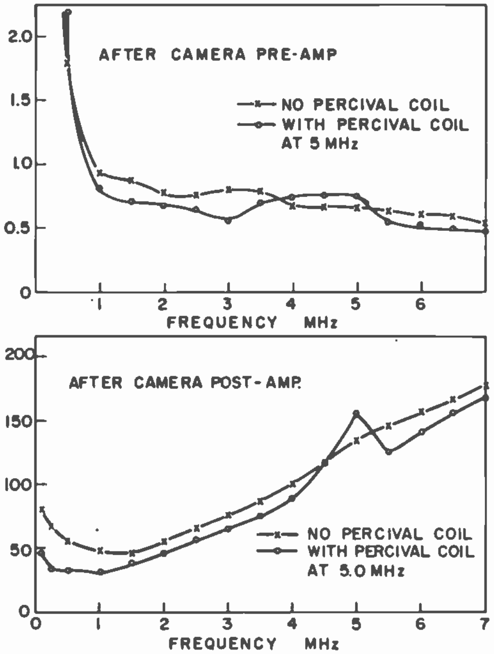

Fig. 10—Camera noise spectrum.

coil) versus "B"(without the Percival coil) tests, but the actual improvement could not be verified by measurements with the selective microvoltmeter. The absolute amount of improvement obtainable by this approach depends upon the specific noise-source characteristics and upon the amount of incidental circuit feedback introduced by the tuned circuit.

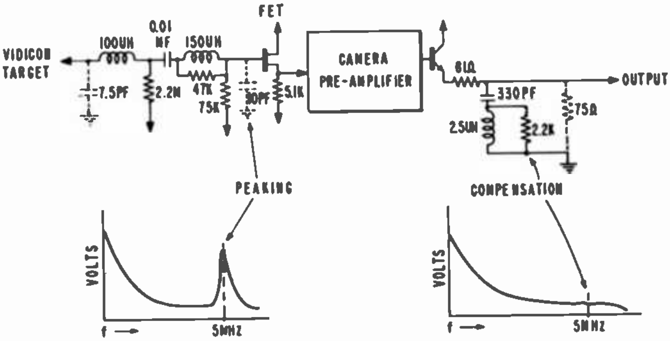

Fig. 11—Frequency-compensation circuit used in camera preamplifier.

4.4 Colorimetry

The basis for colorimetry performance was described by the NTSC broadcast standards.*[11-13] The test-setup instrumentation included a vectorscope that was fed from a standard NTSC encoder unit (TG4). The encoder, in turn, was fed from the red, green, and blue outputs of the decoder for the system being tested. Thus, the colorimetry performance was directly translated into terms of hue and saturation as represented by points on the vectorscope.[11] Radial distance on the vectorscope is related to saturation (although not a direct measure), while angular position is a direct measure in terms of phase angle of the color hue. The EIA chrominance amplitude tolerance of ± 10% and the phase tolerance of ± 5° were used as criteria for the colorimetric performance of the stripe-filter camera systems.[13]

The optical factors that determine the overall colorimetry performance include the color temperature of the illumination source, the spectral transmission characteristics of the encoding filters stripes, the spectral response of the vidicon, and the spectral response of any trimming filters or antireflective coatings used on any of the optical elements in the system.[2,10]

Once the source illuminant is shown, the spectral characteristics of the encoding filters can be calculated assuming that the vidicon spectral response is known along with any other trimming filter effects that may exist. This procedure is discussed in detail in Reference (2). The transmission spectral characteristics actually used for the tests for the yellow–clear, cyan–clear, and magenta–clear filters are shown in Figs. 3 and 4, respectively.

The spectral characteristic of the vidicon is important in determining the overall system colorimetry. A typical spectral response curve is shown in Fig. 12.

Small deviations from the ideal spectral characteristics may be compensated by adjustment of the electronic matrix circuits in the decoder. However, when taken to extreme, colorimetric errors may result and the color signal-to-noise ratio and luminance-to-color crosstalk effects are aggravated by the increased matrix circuit gain necessary to restore the loss of a particular color sensitivity.[2,10]

A special color slide was developed consisting of large areas of red, green, blue, and reference white to allow proper adjustment of the

---

* FCC broadcast standards are ± 10° phase and ± 20% amplitude for the chrominance subcarrier. The EIA standards of good practice are ± 5° phase and ± 10% amplitude.

matrix circuitry when the optical system spectral characteristics are as specified (see Appendix 2 for details.)

In each of the systems tests, the matrix circuitry was adjusted, with the test slide as the object scene, to place the vectors representing the red, green and blue primary colors within the tolerance area represented by ± 10% amplitude and ± 5° phase as indicated on the vectorscope. At the same time, the white balance was maintained near illuminant C (6500°K). The nature and extent of the colorimetric variations from this starting point could be measured by observing the vectorscope presentation and translating the results in terms of NTSC values.

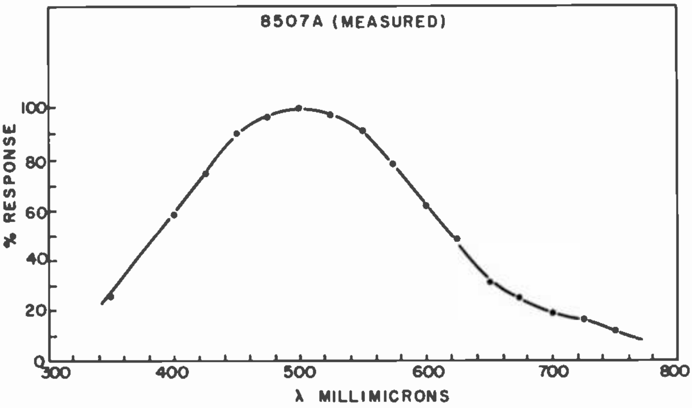

Fig. 12—Vidicon spectral characteristics.

After the proper spectral characteristics are determined, two sources of dynamic operating colorimetric errors exist. The first is variation in the ability of the scanning electron beam to resolve the stripe-color filters equally over the entire raster area, which results in large-area color saturation and hue errors. The variations in spot size and shape result from a complex combination of beam-focus and magnetic-deflection fields. Considerable effort has gone into the development of an optimum deflection–focusing package that provides uniform spot resolution of the stripe filters in the frequency range between 3.5 and 5.0 MHz and stripe-filter angles that vary from the vertical to ± 45° orientation.

The second source of colorimetric error is improper tracking of the transfer function characteristic for the red, green, and blue signals over the operating dynamic range from low-lights to highlights. Although the envelope detector circuits may be operated in a linear mode, the beam size and shape changes slightly from one subcarrier frequency to the other as the scene content varies from dark to light. Thus, the effective transfer characteristic can vary for the different colors and produce color errors in mixture colors that vary with scene content. This variation is particularly evident in the case of two-stripe color-carrier systems where the third color is obtained by mixing the envelope detected signals with the baseband signal. In these systems, it is usually necessary to provide individual color-channel transfer-function correction circuitry to obtain suitable tracking. Three-stripe color-carrier systems suffer considerably less in this respect, since all three-color low-frequency components are derived from the detection of modulated carriers and then matrixed with a common baseband signal. The degree of tracking was measured for each system without individual channel correction circuits and the results are indicated in Figs. 13, 14, 15, and 16.

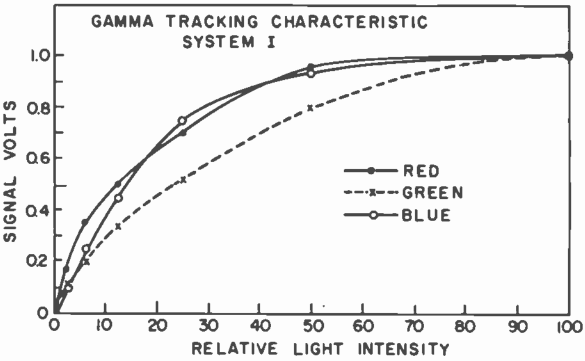

Fig. 13—Gamma tracking characteristic for system I.

Several of the system alternatives are aimed at improving the color uniformity situation. Systems that rely upon a baseband signal and two color subcarriers have an inherent disadvantage in that inequalities in the ability to resolve the color subcarriers results in colorimetric shifts in hue in the direction of the color represented by the information contained within the baseband (usually green). On the other hand, systems that employ three color subcarriers plus a baseband signal have a partial failure mode that is considerably less noticeable to the human eye, in that the color saturation is the predominate error produced as a result of the failure to properly resolve the color stripes. Experience indicates that, within the specific system application restraints, the so-called "fail-to-gray" three-stripe-color systems are supe-

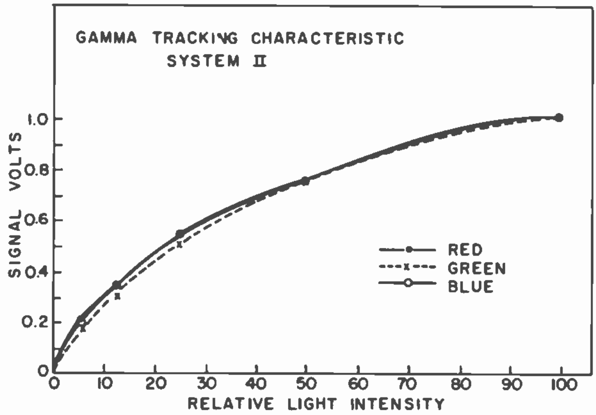

Fig. 14—Gamma tracking characteristic for system II.

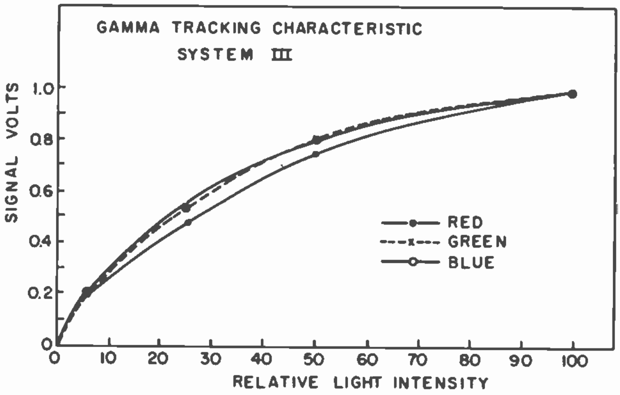

Fig. 15—Gamma tracking characteristic for system III.

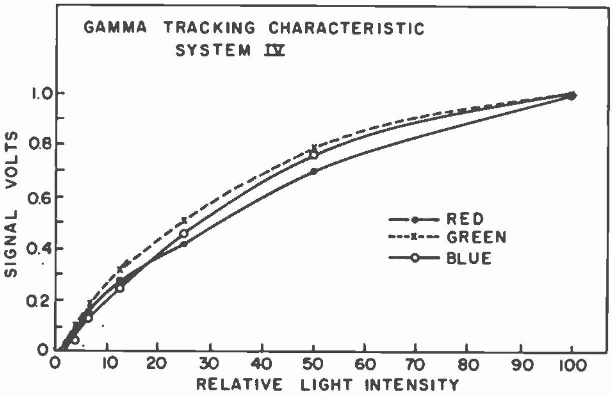

Fig. 16—Gamma tracking characteristic for system IV.

rior in color uniformity and are considerably less sensitive to beam-spot nonuniformities.

4.5 Spatial Beats

A problem that confronts all single-tube stripe-color-encoded camera systems is the optical beat that occurs when the equivalent spatial frequency of the detail content in the scene coincides with the spatial frequency of the color stripes themselves. This pattern manifests itself in the form of low-frequency color beats on edges of objects in the scene.

These beats may be essentially eliminated by a variety of optical means for producing a "trap" effect that reduces the scene energy content at a spatial frequency equivalent to the horizontal component of the stripe-color-encoding filters.

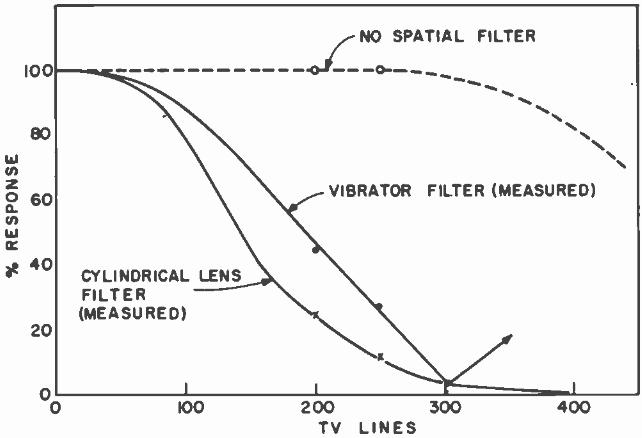

Fig. 17—Amplitude-versus-frequency response for cylindrical lens filter and vibrator filter.

A cylindrical lens that defocuses the scene in the horizontal direction may be used in a fixed-focus situation but is not readily usable for live camera operation. The resulting measured modulation transfer function, as shown in Fig. 17, is cosine shaped and deteriorates the horizontal resolution excessively at frequencies considerably below that of the color subcarrier.

A method that provides a more acceptable modulation-transfer-function characteristic is an amplitude grating oriented in the vertical direction and with a pitch chosen to produce interference pattern cancellation at a spatial frequency equal to that of the horizontal component of the stripe-color-encoding filters. The light loss, which may be as much as two-to-one, may be tolerated in a film-chain camera but would be undesirable in a live pickup. Phase gratings have been used with little light loss, but are difficult to construct and require accurate adjustment.

From a performance point of view, the best method employed to date utilizes birefringent materials such as calcite or quartz.[14,15] These materials have two indices of refraction, and a single light ray is split into orthogonally polarized components called the "ordinary" and "extraordinary" rays. In calcite, the maximum splitting angle is 6° 13′, and the two rays exit from the crystal parallel to each other and parallel to the direction of entry into the crystal. Thus, two displaced images are created whose physical separation is dependent upon the splitting angle and the path length through the crystal. The crystal position between the camera lens and the vidicon faceplate is noncritical since the crystal is not an image-forming element. The rotational position is adjusted so that the two images are displaced along the horizontal axis of the scanning raster. When the splitting angle is known, the crystal thickness can be calculated to produce a physical displacement equal to the horizontal component of the width of one color stripe. For calcite, with a splitting angle of 6°, the thickness is approximately 0.010 inch for a stripe-color filter whose pitch is 530 lpi oriented in the vertical direction. The thickness would be increased in proportion to the secant of the angle between the stripes and the vertical. Quartz is used in the same manner, but has a considerably smaller splitting angle (about 0.24°), so that a filter for the same 530 lpi stripes would have a thickness in the order of 0.250 inch.

A convenient and flexible method used with the experimental relay optics setup was to produce controlled lateral motion of the image by vibrating the taking lens or the right-angle mirror in the experimental relay optics system with a solenoid fed by 60-Hz alternating current. The degree of image displacement could be adjusted by controlling the current through the solenoid, and, thus, the equivalent frequency of the rejection "trap" could be varied to match the system conditions under test. Fig. 17 indicates the measured modulation-transfer-function characteristic for such a vibrator system.

5. Kell/SRI Reference System

The basic reference color-encoding technique used in these studies is called the Kell/SRI system, which has been described in detail in various publications and exists in the form of a commercial product in both live camera (PK730) and film chain (PFS710).[9] Therefore, its fundamental concepts and operating characteristics will be only briefly reviewed.

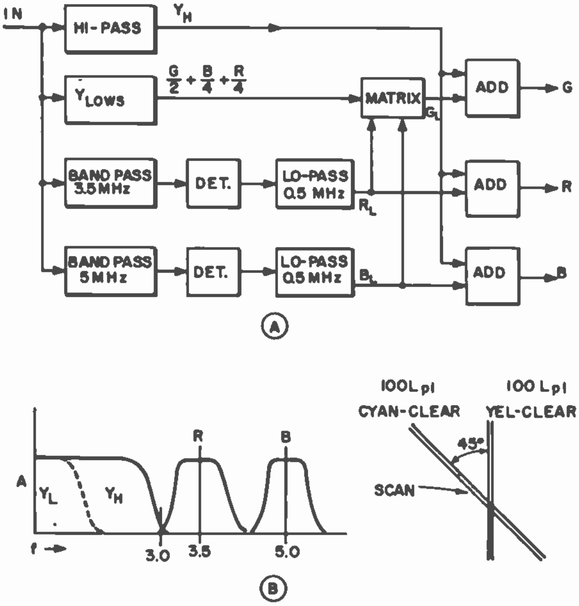

Fig. 18—Kell/SRI system: (a) decoder functions and (b) composite-signal frequency spectrum.

Fig. 18(a) is a block diagram of the required decoder functions while Fig. 18(b) indicates the composite-signal frequency spectrum. One stripe-color filter, comprised of cyan and clear stripes and oriented in the vertical direction (right angles to the direction of horizontal scan), causes an electrical signal at 5 MHz to be generated. This signal carries the red color information as amplitude-modulation sideband components. Another set of stripe-color filters of the same pitch, comprised of yellow and clear stripes and oriented at an angle of 45 degrees to the vertical, produces an electrical signal at 3.5 MHz whose modulation sideband components contain the blue color information. The baseband signal is band limited to about 3.0 MHz, and the two color subcarriers are extracted from the composite signal by appropriate band-pass filters, and are then individually envelope detected to recover the red and blue color signals. The green color signal is derived from the baseband signal in an appropriate matrix circuit, and the individual red, green, and blue color signals are fed to a conventional color viewing system.

Two serious shortcomings of this system are the relatively inefficient use of the available frequency spectrum of the pickup device and the colorimetric errors introduced by nonuniform resolution of the stripes that produce the color subcarriers. The vidicon electron-beam spot shape and size determines the ability to resolve the color stripes, and controls the amplitude of the resulting red and blue color signal components relative to the green color components contained in the low-frequency baseband signal. Thus, as the beam scans the raster area, differences in spot focus and/or astigmatism result in variations of color mixture relationships of red and blue versus green. Mixture colors are therefore colorimetrically shifted toward the green, and the system "fails to green" in the limit when no subcarriers are generated, such as in highlight overload or extremely poor corner-focus conditions. Considerable effort, with reasonable success, has gone into the design and development of deflection–focusing systems that result in relatively uniform focus fields, but this area remains as a critical problem from both an initial design and an operating point of view for this color-encoding system.

The new systems being evaluated are aimed at minimizing or eliminating the problems of bandwidth utilization and colorimetric variations relating to beam-spot focus, while still providing acceptable or improved performance in areas such as signal-to-noise ratio, colorimetry, operational simplicity and stability beats, and resolution.

6. Stripe-Color Amplitude-Modulation System I

6.1 System Description

The upper frequency limit usable for color subcarriers in single-tube stripe-color systems is largely dictated by the available signal-to-noise ratio in a one-inch pickup device such as the 8507A. For example, the Kell/SRI system utilizes two independent subcarriers for the red and blue color information with one located at about 5 MHz and the other at 3.5 MHz. A baseband resolution limit of about 3 MHz results when 500-kHz color-channel resolution (1 MHz band pass for each color) with sufficient guard space has been allowed. It would be highly desirable to somewhat relax this upper frequency requirement in the interest of better spot-focus uniformity (color uniformity) and improved signal-to-noise performance, while at the same time providing higher resolution in the baseband channel. These seemingly conflicting requirements have been met to a high order in a system designated as stripe-color amplitude-modulation system I.

System I makes more efficient use of the available frequency spectrum by causing the carriers and sideband modulation components representing the red and blue color information to occupy the same band of frequencies. Thus, the upper frequency limit required from the vidicon may be reduced, while an increase is still allowed in the upper frequency limit of the baseband signal. The red and blue color signals are made to occupy the same portion of the frequency spectrum simply by rotating the cyan–clear and yellow–clear stripe filters (equal pitch) such that they are symmetrically disposed on either side of the vertical axis of the scanned raster. Thus, on an instantaneous basis, the carrier frequencies are identical; however, the angular displacement is such that a time delay difference equal to ± 90° at the subcarrier frequency exists when the signals are compared on a line-to-line basis. This causes the two signals to be frequency interlaced with respect to each other, and the independent color modulation components can be identified and separated from each other by means of a "comb filter" circuit involving a 1-H delay line (see Appendix 1). The absolute value of the subcarrier frequency is proportional to the pitch of the stripes and to the cosine of the angle of inclination from the vertical. Thus, a relationship exists that allows the angle to be determined that results in ± 90° time displacement at the particular carrier frequency involved when one line is compared to the following line. The 180° total displacement from the red signal to the blue signal results in the interleaved energy spectrum and allows separation to be accomplished by means of a comb filter. Fig. 36, Appendix 1, is a plot indicating the relationship between spatial frequency, electrical frequency, and angle of inclination required for the line-to-line 180° relationship to exist.

Fig. 34, Appendix 1, indicates the vector diagram relationships and the block diagram of the functions performed in a 1-H delay line comb-filter circuit. Fig. 19(a) is a block diagram indicating the functions required to apply this technique to a complete color-camera decoding circuit. Fig. 19(b) indicates the frequency spectrum for system I with the particular values of frequency relationships chosen for the experimental evaluation. The value of 4.2 MHz for the subcarrier frequency, being somewhat lower than the 5 MHz value previously required, places less stringent demands upon the beam spot focus and results in better color uniformity and improved signal-to-noise ratio, while at the same time allowing the resolution limit of the baseband signal to be increased to at least 3.6 MHz.

As can be seen from the block diagram on Fig. 19, the changes from the Kell/SRI system required in order to realize these performance gains are minimal. The same optical stripe-color filters are used; they are merely reoriented to be symmetrically disposed at the appropriate angle around the vertical scan axis. The same luminance channel circuits, amplitude detectors, and matrix functions are required. Only one band-pass filter is required in order to select the red and blue color information, while a 1-H delay line comb filter circuit is added to provide means for separating the red and blue information prior to envelope detection.

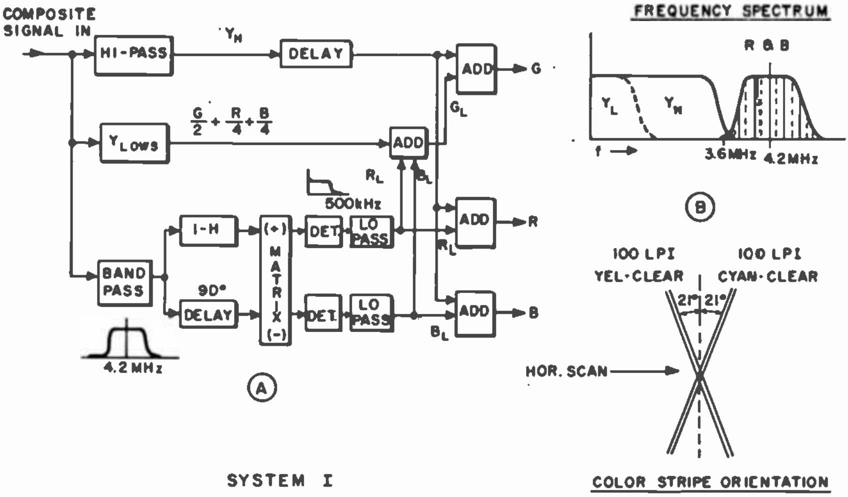

Fig. 19—System I: (a) decoder employing 1-H delay comb filter and (b) frequency spectrum.

6.2 System I Performance Characteristics

As previously stated, system I makes efficient use of the frequency spectrum available from the pickup device. Considerable freedom is available for the choice of specific system parameters and the system can therefore be effectively tailored to the particular application under consideration. For evaluation purposes, the NTSC broadcast standards as practiced in consumer products were used as the measurement criteria. A color subcarrier frequency of 4.2 MHz was chosen, which, along with 500 kHz color bandwidth (1-MHz band pass), allows a luminance-channel limiting resolution of 3.6 MHz. This choice results in an approximate match to the typical response found in commercial color TV receivers.

[a] Signal-to-Noise Ratio:

System I has an inherent advantage over the Kell/SRI system in signal-to-noise performance of at least 3 dB, assuming all other factors to be equal. This advantage occurs as a result of the interleaving of the two color signals into a common band-pass region, thereby reducing the required color signal band-pass by a factor of two. An additional gain may be realized by the ability to reduce the upper frequency requirement from the vidicon, while still maintaining the same baseband resolution (5 MHz was lowered to 4.2 MHz in the case of the test setup). The combination of the two effects resulted in a measured improvement of 6-8 dB when the two systems were compared, with all other factors maintained equal, i.e., the same vidicon, the same optical stripes, the same preamplifier.

Table 1 gives the actual signal-to-noise measurements as measured at the red, green, and blue decoder outputs prior to gamma reinsertion.

Table 1—S/N Measurements for Kell/SRI and System I

Color	Kell/SRI	System I
Red	40.6 dB	47.0 dB
Green	45.2 dB	53.1 dB
Blue	39.2 dB	43.5 dB

[b] Colorimetry:

System I is similar to the Kell/SRI system in that variations in the ability of the electron beam spot to resolve the color subcarriers results in colorimetric errors that shift toward the green portion of the spectrum, since the baseband signal contains the green information while the red and blue information is in the subcarriers. System I has improved color uniformity, since the blue- and red-signal color stripes are equally resolved (same frequency) by the spot and are less subject to differences arising from spot astigmatic problems.

In the test setup, the matrix adjustments were made by observing a color-bar scene made of appropriate gelatin filters and causing the red, green, and blue signals to fall within ± 5° phase and ± 10% amplitude as observed on a vectorscope after re-encoding the signal by means of a TG4 NTSC standard encoder. Photographs in Figs. 20(a) 20(b) and 20(c) indicate typical waveforms and vectorscope presentation for system I. Fig. 21 is a reproduction of a typical slide using system I.

The ability of the red, green, and blue signals to track each other over the dynamic operating range as the input light level varies is indicated in the measured "effective" gamma characteristics as shown in Fig. 14. These curves represent the uncorrected signals, and appropriate circuit nonlinear functions must be introduced to compensate for these colorimetric variations.

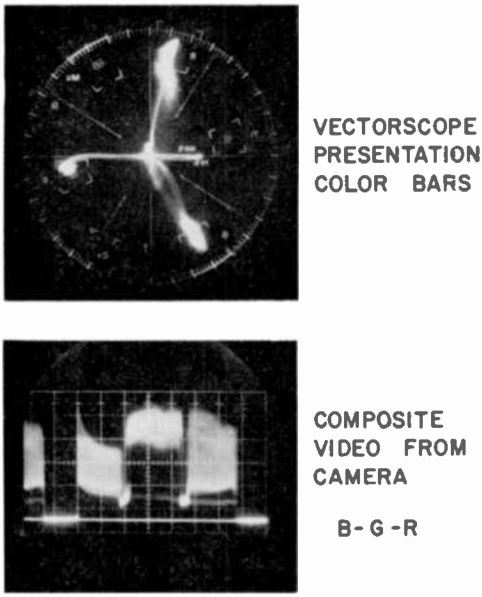

Fig. 20(a)—System I vectorscope presentation and composite video signal from camera.

[c] Beats and Spurious Signals:

Moiré beats occur in the optical systems for the single-tube color camera as a result of scene content having high-frequency components that coincide with the pitch of the stripe-color filters. These beats must be minimized by means of an optical filter having a rejection point corresponding to the hoizontal component of the pitch of the stripes. Filters of this type have been discussed previously (Sec. 4.5).

"Cross-color" electrical signal beats occur on edges of colored objects and represent color-modulation sideband components that correspond to high-frequency baseband signal components. The amplitude of these beat components is determined by the shape of the baseband modulation-transfer-function characteristic and is usually a compromise between beat visibility and resolution as determined by the system designer.

In the Kell/SRI system, an electrical signal beat of 1.5 MHz may

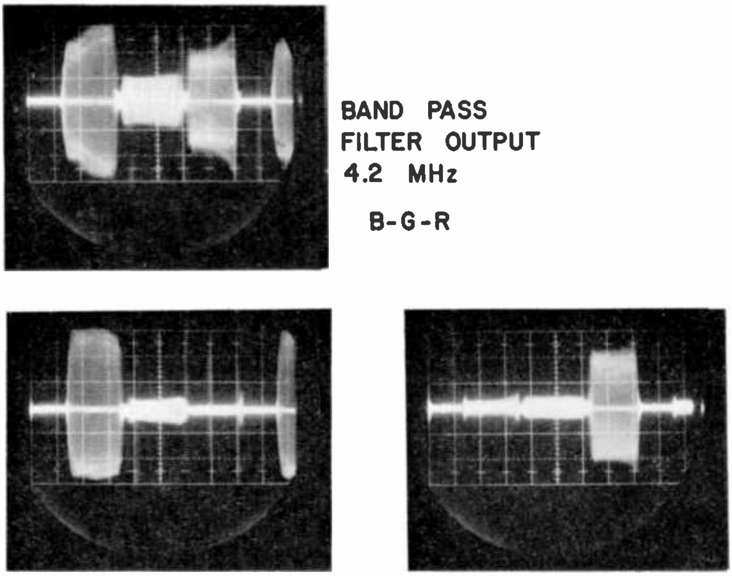

BAND PASS FILTER OUTPUT 4.2 MHz

B-G-R

BLUE-COMB. FILTER OUTPUT

RED-COMB. FILTER OUTPUT

Fig. 20(b)—System I filter outputs.

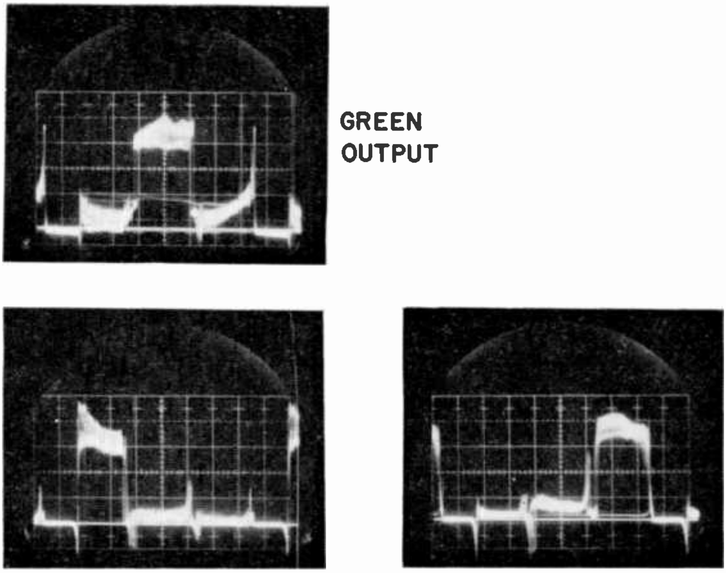

GREEN OUTPUT

BLUE OUTPUT

RED OUTPUT

Fig. 20(c)—System I color output signals.

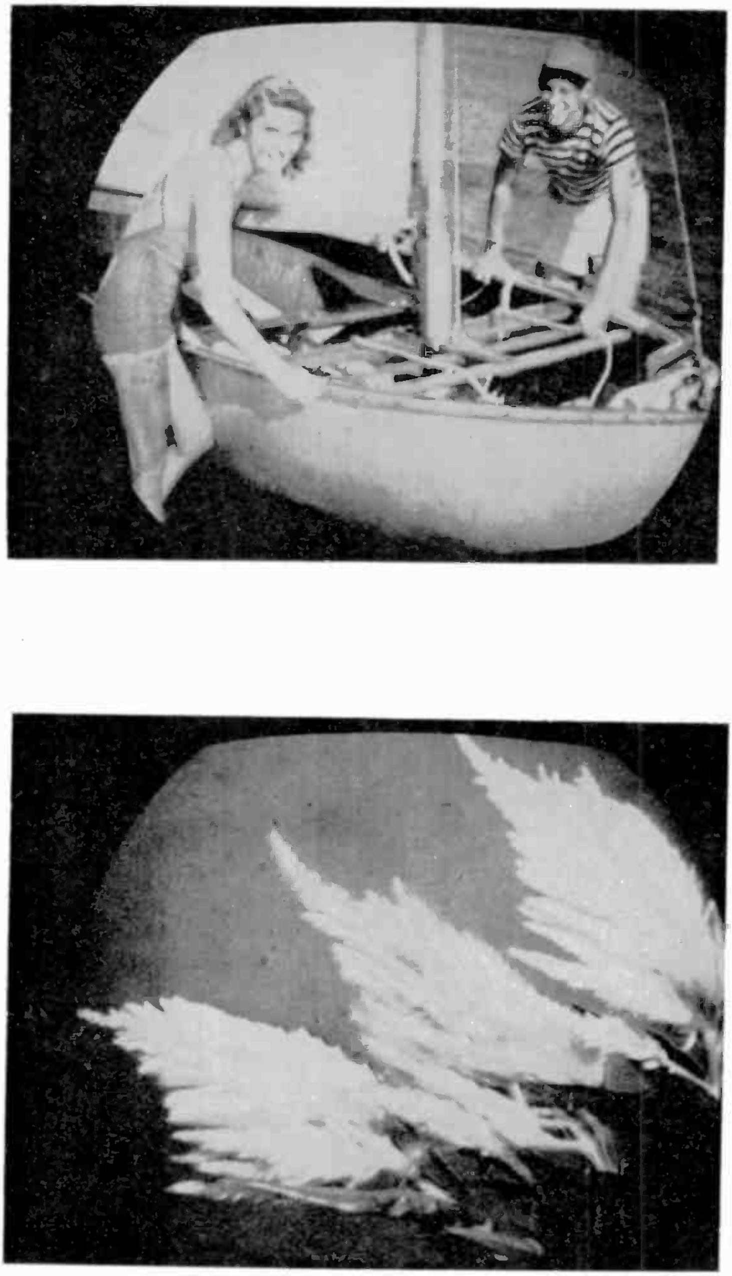

Fig. 21—Reproduction of typical slide using system I.

occur between the two subcarriers at 3.5 MHz and 5 MHz and will appear in large-area color-mixture portions of the scene. In system I, the red and blue color subcarrier frequencies are the same on an instantaneous basis. However, the signals are separated by comparing each line with the succeeding line in a comb filter. Thus, an interline (7.875 kHz) beat can occur if the filter circuits become sufficiently unbalanced or if the timing of one horizontal scan line with respect to the other varies excessively. Measurements indicate that a timing jitter of 2-3 nanoseconds is insignificant, but values above 8-12 nanoseconds become objectionable and result in excessive loss of comb-filter rejection. Comb-filter circuit balance that results in rejection of the undesired color signal by 30-40 dB is easily achieved with color-broadcast-quality sync-generator timing circuits. A simple solution to the horizontal timing jitter experienced in some industrial-quality sync generators is to use a flywheel-driven deflection circuit, which completely eliminates the effects of timing variations from one line to the next. The sync-generator source must be locked from a crystal (usually 3.58 MHz) in order to ensure long-term stability and matching of the horizontal line to the 1-H delay-line length employed in the comb filter.

7. Stripe-Color Amplitude-Modulation System II

7.1 System Description

System I suffers a colorimetry problem if the spot fails to resolve the color stripes uniformly over the scanned area. System II reduces this problem at some sacrifice in bandwidth utilization efficiency by introducing a third color subcarrier at a frequency higher than that of the two interlaced color subcarriers. Thus, all the color information exists as modulation components of the color subcarriers, and the luminance information is carried by the baseband signal. If the subcarriers are not resolved by the spot, the saturation of the scene changes, as opposed to the color hue, and provides a much more acceptance failure mode described as "fail-to-gray" operation.

Fig. 22(a) is a block diagram of system II, indicating the necessary circuit functions for a complete camera decoder. Fig. 22(b) indicates the frequency spectrum for system II with the particular values of frequency relationships chosen for the experimental setups.

The red and blue color information is carried by interlaced carriers at 3.6 MHz with equal-pitch yellow–clear and cyan–clear stripe filters located symmetrically about the vertical axis at ± 24°. The red and blue color information is separated by a 1-H delay comb filter exactly as accomplished in system I. A third color signal is generated by the addition of magenta–clear stripes oriented in the vertical direction and having a pitch suitable to produce an electrical frequency of 4.92 MHz. This subcarrier provides the green color information and is combined with the red and blue decoded signals in a suitable linear matrix to produce the R-Y, B-Y and G-Y color difference signals. These signals are then individually combined with the baseband signal to produce the final red, green, and blue output signals.

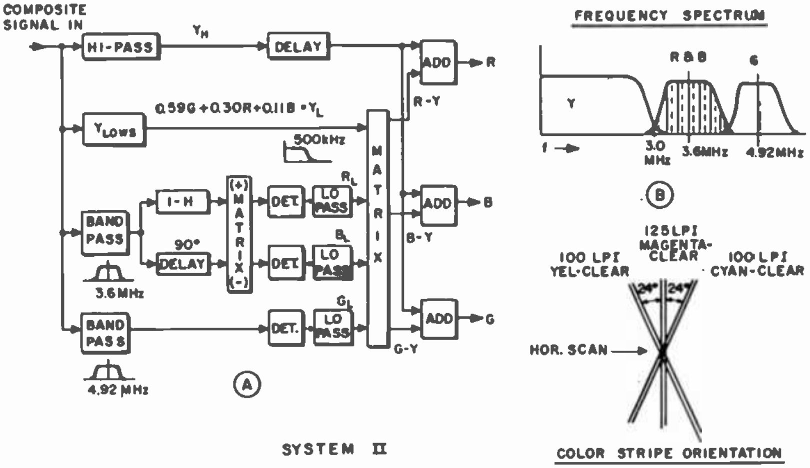

Fig. 22—System II: (a) decoder and (b) composite signal.

7.2 System II Performance Characteristics

The most outstanding performance characteristic of system II arises from its fail-to-gray feature. In actual operation the relative lack of sensitivity to changes in electrical focus is readily apparent since the color errors occur primarily as changes in saturation as opposed to color hue.

[a] Signal-to-Noise Ratio

With all elements of the system being maintained the same except for the addition of the magenta–clear stripe filter and the appropriate decoder circuit changes, the signal-to-noise ratio for system II is essentially the same as that of system I. This occurs in spite of the fact that an additional subcarrier has been added to the system at 4.92 MHz that contains the green-color-signal information. Normally, the additional bandwidth at the high end of the spectrum would degrade the overall signal-to-noise performance. However, three compensating effects result in approximately the same signal-to-noise performance as obtained with previous two-subcarrier systems. First, the interlaced red and blue color signals are at a slightly lower electrical frequency (3.6 MHz versus 4.2 MHz) and therefore contribute slightly less noise. Second, the spectral response of the Sb_2S_3 photoconductor peaks in the green portion of the spectrum and is therefore more sensitive in that region, which more than offsets the optical loss due to the introduction of the additional stripe-color filter. Third, if the spectral characteristics of the color stripe filters are tailored to produce a baseband signal whose luminance values are in accordance with the NTSC Y values (0.59G, 0.30R, 0.11B), the absolute amount of signal from the green subcarrier required by the matrix to produce the final green output signal is minimized relative to the red and blue components and, thus, the visibility of the noise contained in the green signal is minimized.

Table 2 gives the actual signal-to-noise values as measured in the red, green, and blue decoder outputs prior to gamma reinsertion.

Table 2—S/N Measurements for System II

Color	System II
Red	47.6 dB
Green	51.1 dB
Blue	46.0 dB

The principle of constant luminance may be easily utilized in the three-subcarrier systems to further reduce the visibility of the noise as viewed on a standard color monitor. If the spectral characteristics of the stripe-color filters, in combination with the vidicon characteristic, are tailored to produce the NTSC luminance values for the baseband signal,[11,12] the decoder matrix circuit must then be adjusted to produce K_1(R-Y), K_2(G-Y) and K_3(B-Y). The values of K_1, K_2, and K_3, when individually added to the Y signal to reproduce the red, green, and blue output signals, are such as to provide constant-luminance operation.[11] The reduction in visible noise in the viewing monitor has been measured as being as high as an additional 8 dB in the experimental setup. This value can be realized when the composite signal from the camera has been linearized prior to the decoding and matrix functions. Gamma reinsertion is introduced into the individual red, green, and blue output signals prior to viewing with a standard color monitor.

[b] Colorimetry:

The test setup decoder matrix adjustments were made by observing a color-bar scene made of appropriate gelatin filters and causing the red, green, and blue signals to fall within the NTSC tolerances of ± 5° phase and ± 10% amplitude as observed on a vectorscope. Photographs in Figs. 23(a), (b) and (c) indicate typical waveforms for the luminance channel, the color difference signals, and the final red, green, and blue output signals. Fig. 24 is a reproduction of a typical slide using system II.

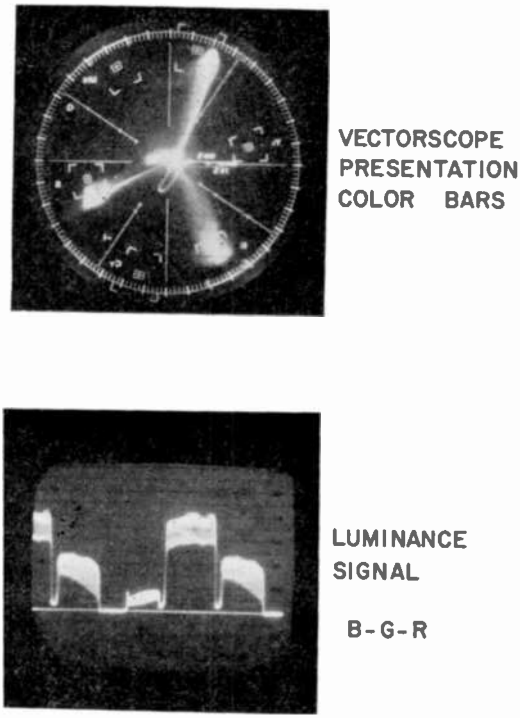

Fig. 23(a)—System II vectorscope presentation and luminance signals.

The flat-field color uniformity of system II is superior to previous systems due to the fail-to-gray characteristic that translates the partial or complete failure of the spot to uniformly resolve the color stripes to changes in color saturation instead of color hue.

The details of the desired stripe-color filter spectral characteristics are discussed elsewhere.[2] The specific spectral characteristics of the filters used in the test setup are shown in Figs. 3 and 4.

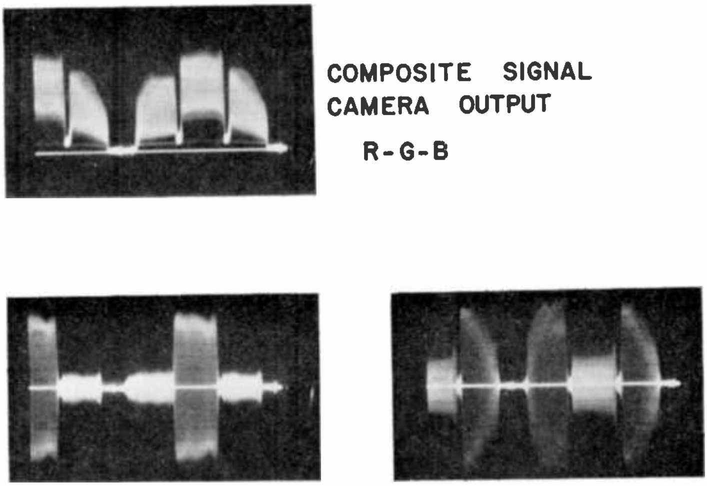

COMPOSITE SIGNAL
CAMERA OUTPUT
R-G-B

R AND B BAND-PASS
OUTPUT 3.6 MHz

G BAND-PASS OUTPUT
4.92 MHz

Fig. 23(b)—System II color difference signals.

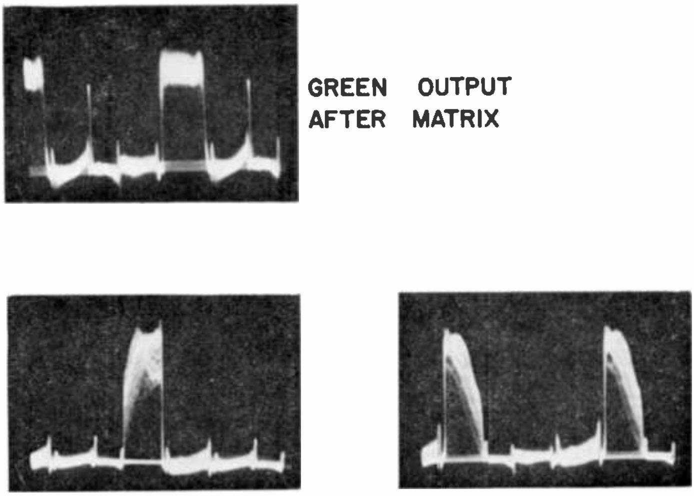

GREEN OUTPUT
AFTER MATRIX

BLUE OUTPUT AFTER
MATRIX

RED OUTPUT AFTER
MATRIX

Fig. 23(c)—System II color output signals.

Fig. 24—Reproduction of typical slide using system II.

[c] Beats and Spurious Signals:

In this system, an electrical signal beat of 1.32 MHz may occur between the red and blue interlaced subcarrier at 3.6 MHz and the green subcarrier at 4.92 MHz and will appear in large-area color-mixture portions of the scene. In addition, as in system I, an interline beat (7.85 kHz) can occur if the comb-filter circuits become sufficiently unbalanced or if the timing of one horizontal scan line with respect to the next varies excessively.

The level of the 1.32 HMz beat should be below the level of visibility if the decoder circuits are linear. However, beat-signal-amplitude values of the order of 5% may be effectively eliminated by use of a simple cancellation technique. Portions of the 4.92 MHz carrier and the 3.6 MHz carrier are selected by two tuned circuits and mixed in a nonlinear diode circuit to produce a 1.32-MHz beat signal. The beat signal is selected by a tuned circuit and fed back into an appropriate point in the luminance channel circuit in 180° phase opposition to exactly cancel the residual beat signal. Reduction of the beat signal components between 40 and 50 dB below picture signal white level has been achieved. Fig. 25 indicates a typical circuit for such a cancellation technique that has proven effective in the test setup.

8. Stripe-Color Amplitude-Modulation System III

8.1 System Description

Fig. 26(a) is a block diagram of system III, indicating the necessary circuit functions for the decoder. Fig. 26(b) indicates the frequency spectrum with the particular values of frequency relationships chosen for the experimental setup.

As in the previous systems, the red and blue color subcarriers are interlaced with each other on a line-by-line basis at a frequency of 4.2 MHz.

In order to regain the bandwidth utilization efficiency of system I while still retaining the fail-to-gray feature of system II, the green color information is carried by another subcarrier located at a lower frequency than that chosen for the red and blue subcarrier. This subcarrier at 3.2 MHz is so chosen as to cause the color sidebands to overlap and to be specifically interlaced with the high-frequency detail content of the baseband luminance signal. Thus, the green color information must be separated from the luminance signal by means of a 1-H delay-line comb-filter circuit similar to the unit used to separate the red and blue signals when compared on a line-by-line basis.

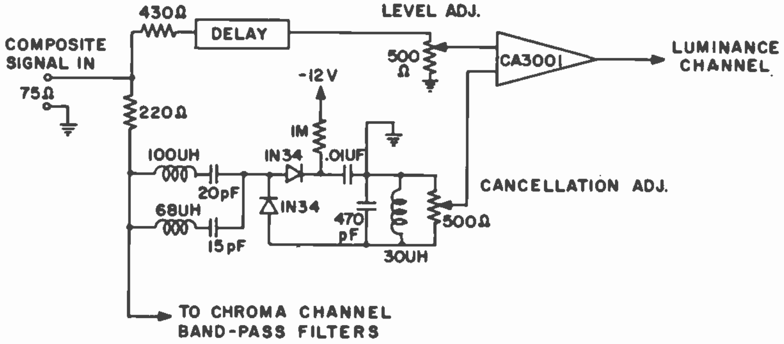

Fig. 25—Beat cancellation circuit diagram.

In the experimental setup the yellow–clear and cyan–clear stripes were oriented at ± 21° with respect to the vertical axis with a pitch suitable to produce an electrical frequency of 4.2 MHz. The magenta–clear stripes were oriented at an angle of 42° with respect to the vertical and had a pitch such that an electrical frequency of 3.2 MHz was generated. The experimental decoder employed two separate 1-H delay-line comb-filter circuits for convenience. However, a single broadband delay line could be used with appropriate band-pass selection filters for separating the red, blue, and green color signals.

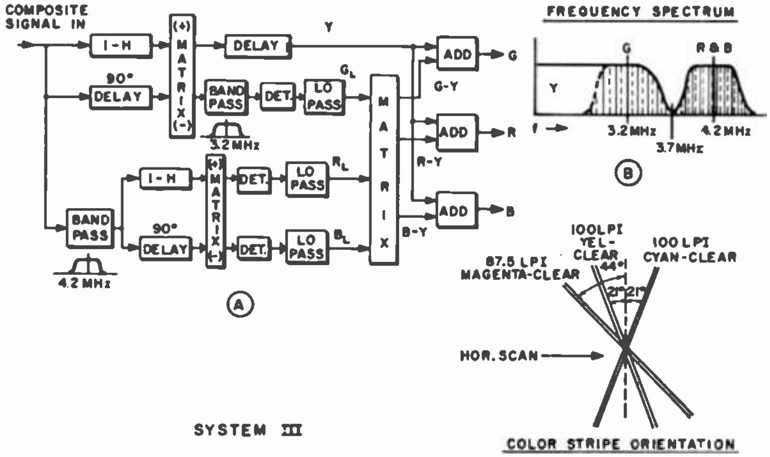

Fig. 26—System III: (a) decoder and (b) frequency spectrum.

8.2 System III Performance Characteristics

System III maintains the highly desirable fail-to-gray characteristic, while making efficient use of the available bandwidth from the pickup device without placing undue constraints upon the horizontal resolution as determined by the luminance channel bandwidth. Some loss of resolution occurs at approximately the 45 degree directions due to the comb-filter separation of the green color information from the high-frequency luminance components.

[a] Signal-to-Noise Ratio:

Some small degree of improvement in signal-to-noise performance over system II should be expected since the subcarrier frequencies are lower in system III. However, the difference is small and does not constitute a major factor in decisions regarding the possible preference of one system over the other in specific applications. The actual signal-to-noise ratio measurements made in the test setup are given in Table 3.

Table 3—S/N Measurements for System III

Color	System III
Red	45.1 dB
Green	51.1 dB
Blue	37.1 dB

[b] Colorimetry:

The large-area color-field uniformity system III is subject to variations due to electron-beam-spot astigmatic effects to a greater degree than systems I and II. This result is due to the large angle (42°) required by the magenta–clear stripes. Fig. 29 indicates the variation in color subcarrier amplitude versus rotational angle of the color stripes in the case of the test setup. This data indicates excessive variations occurring at angles greater than about ± 30°. The fail-to-gray characteristic subjectively helps this situation but the color uniformity is reminescent of the problem inherent in the original Kell/SRI system. Figs. 27(a) and (b) indicate typical signal waveforms for system III, while Fig. 28 is a reproduction of a slide using system III.

[c] Beats and Spurious Signals:

As in previous systems, an interline beat of 7.85 kHz can occur if the comb-filter circuits become sufficiently unbalanced and an electrical beat

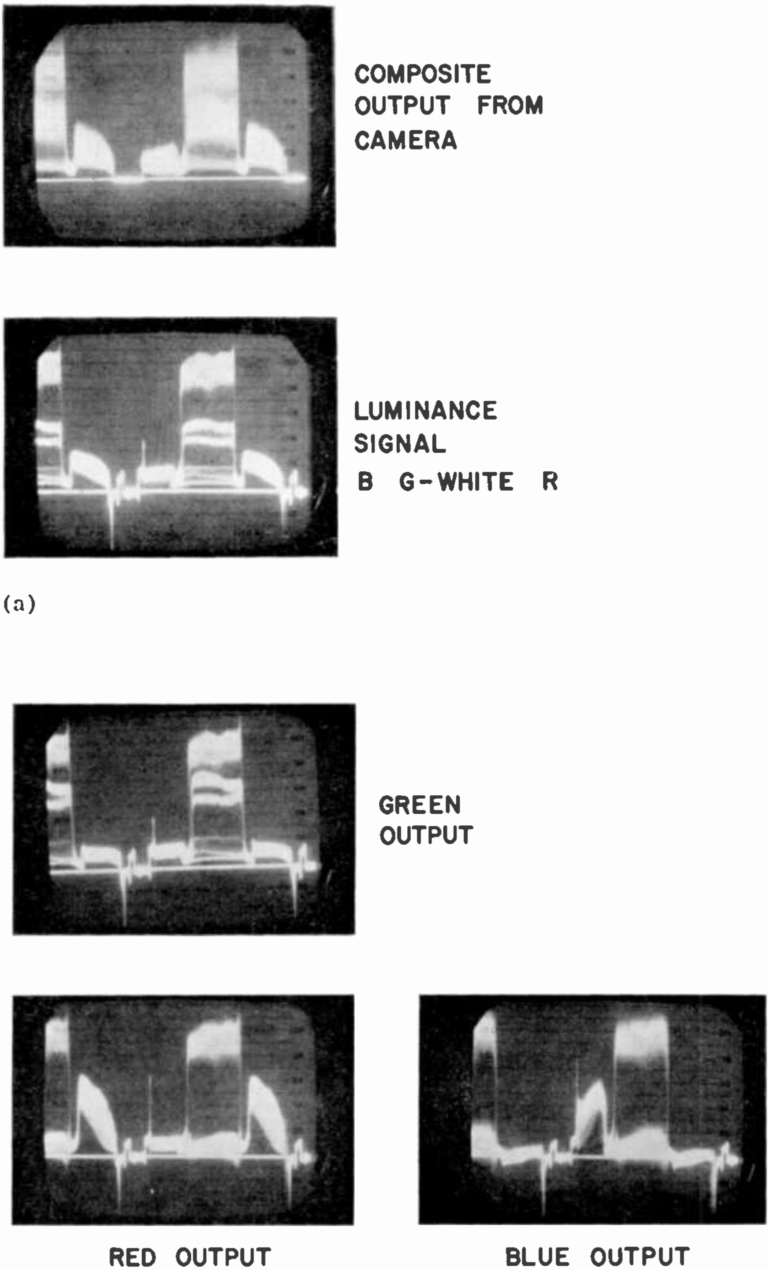

Fig. 27—System III, typical signal waveforms.

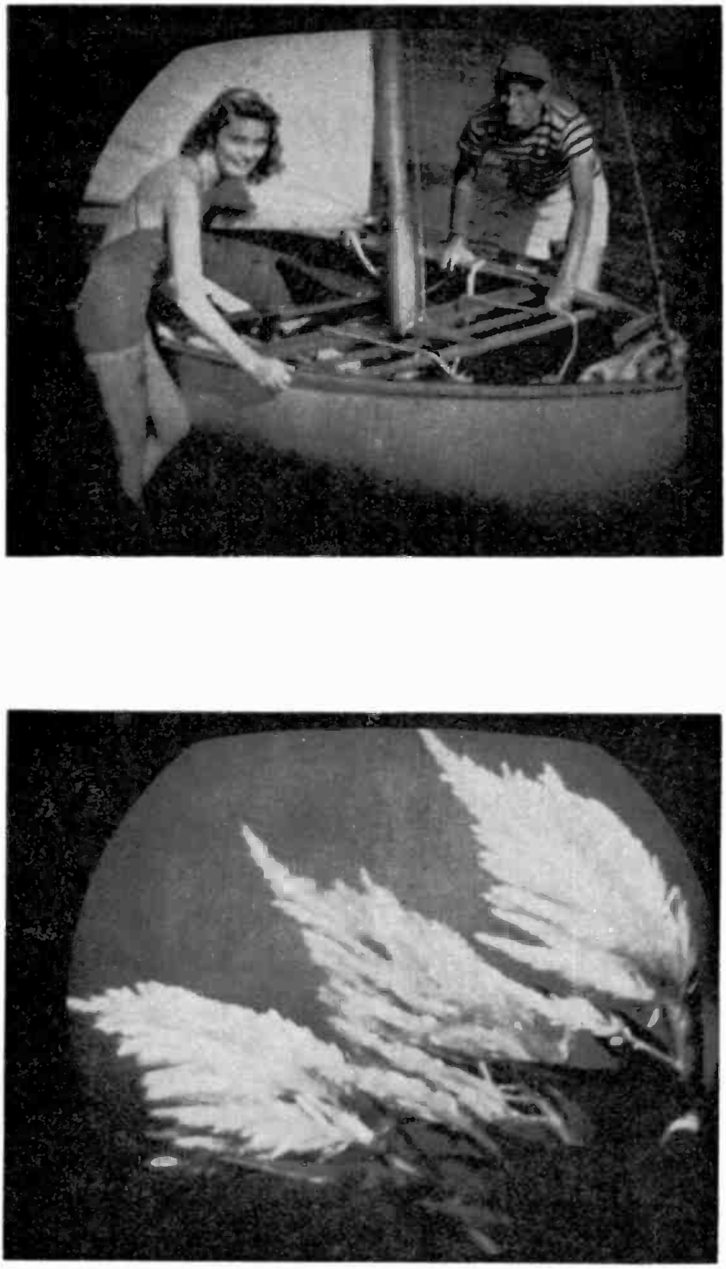

Fig. 28—Reproduction of a slide using system III.

of approximately 1 MHz may occur in large-area mixture colors. The anticipated subjective increase in edge color beats due to the green carrier being interlaced with the high-frequency end of the luminance band did not materialize.

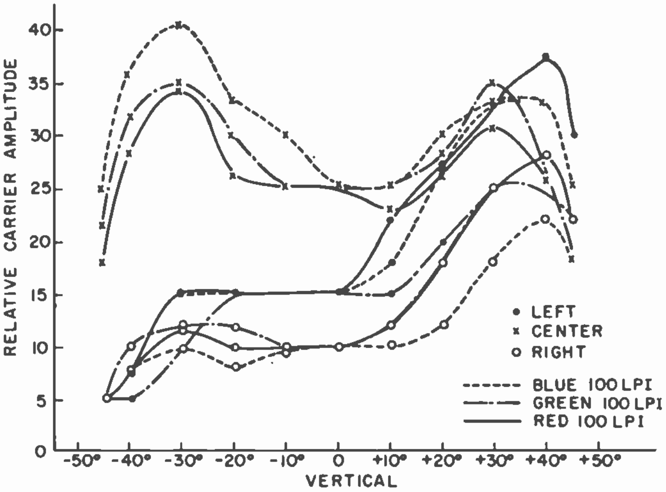

Fig. 29—Carrier response versus angle of rotation of stripes.

9. Stripe-Color Amplitude-Modulation System IV

9.1 System Description

An interesting approach to the multiple-carrier amplitude-modulated stripe-color system is to locate the subcarriers modulated with the red, blue, and green color information at the *same* frequency and employ a 2-H delay-line comb filter circuit to separate the three pieces of color information by comparing three successive scanning lines on a line-by-line basis. The relative angles and pitch of the yellow–clear, cyan-clear, and magenta–clear strip-color filters are arranged so that a delay differential equivalent to 120° of phase at the color subcarrier frequency exists between each of the color signals. In the test setup the yellow–clear and cyan–clear filters were at ± 29° with equal pitch of 100 lpi. The magenta–clear filter was oriented at 0° (vertical) and had a pitch of 87.5 lpi. Fig. 30a is a block diagram of system IV indicating the necessary circuit functions while Fig. 30(b) indicates the frequency spectrum used for the experimental evaluation.

9.2 System IV Performance Characteristics

System IV, by virtue of having the same subcarrier frequency for all three colors, results in the most uniform color characteristics of all four systems. The variations in electron-beam spot shape and size affect all three colors essentially the same. The system is as efficient as system I in its use of the available bandwidth while at the same time maintains the highly desirable fail-to-gray characteristic of systems II and III.

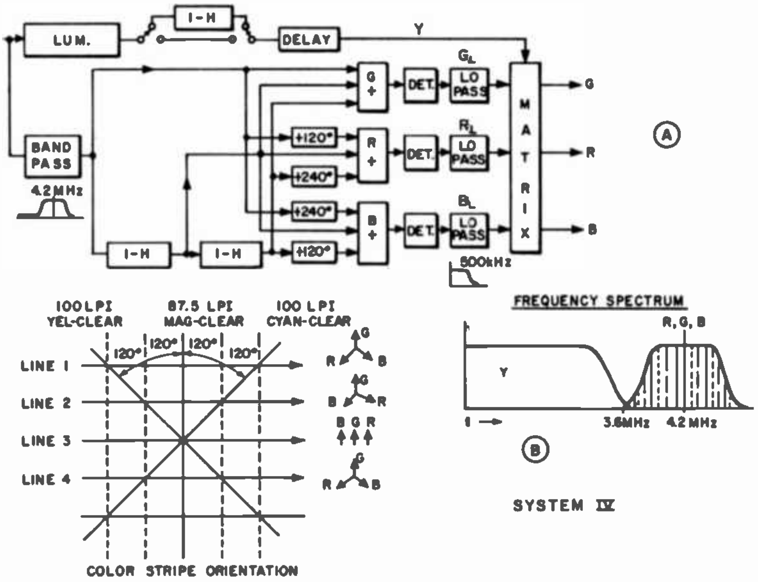

Fig. 30—System IV: (a) decoder and (b) composite signal.

On the negative side, system IV must compare the information on three consecutive scanning lines and requires the use of two 1-H delay lines in a more complex comb filter circuit in order to separate the three colors. The decoder is more complex and critical to initial design and adjustment than the other systems tested. If the comb-filter circuit becomes unbalanced, an interline beat of ⅓ of the line scanning rate is produced that is subjectively more visible than the ½-line-rate beat in previous systems.

In theory, an additional delay of 1-H should be employed in the luminance channel to provide symmetrical transitions of the vertical detail content, i.e., the luminance transitions should be centered in the three-line period required for a vertical color transition. Fig. 31 indicates the results with no additional delay in one case and with the appropriate 1-H delay in the other case. Subjective tests on typical scenes, however, did not show conclusively that the additional 1-H delay was actually required for best results.

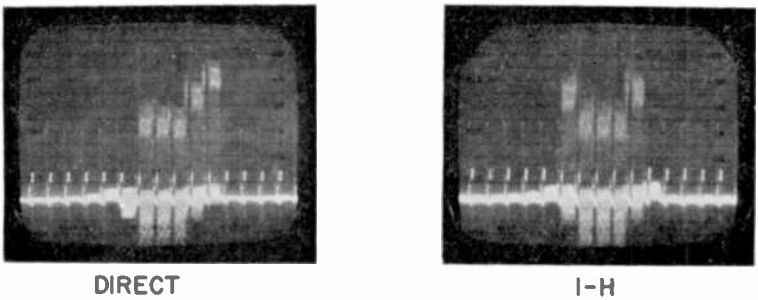

Fig. 31—Luminance channel 1-H delay for system IV.

[a] Signal-to-Noise Ratio

Signal-to-noise measurements were made on this system in the same manner and using the same basic test apparatus as employed in all other systems. The results are indicated in Table 4.

Table 4—S/N Measurements for System IV

Color	System IV
Red	47.0 dB
Green	53.0 dB
Blue	41.6 dB

[b] Colorimetry

In the test setup, the decoder matrix adjustments were made to cause the red, green, and blue signals to fall within the range of ± 5° phase and ± 10% amplitude as observed on a vectorscope. Photographs in Figs. 32(a), (b) and (c) indicate typical waveform for the luminance channel, color difference signals, and the output color signals, respectively. Fig. 33 is a reproduction of a typical slide employing system IV.

Since the same subcarrier frequency is generated by the electron beam scanning of the three sets of color stripes, the three color signals are essentially matched in characteristics such as large-area uniformity, effective gamma, and absolute carrier-signal amplitude.

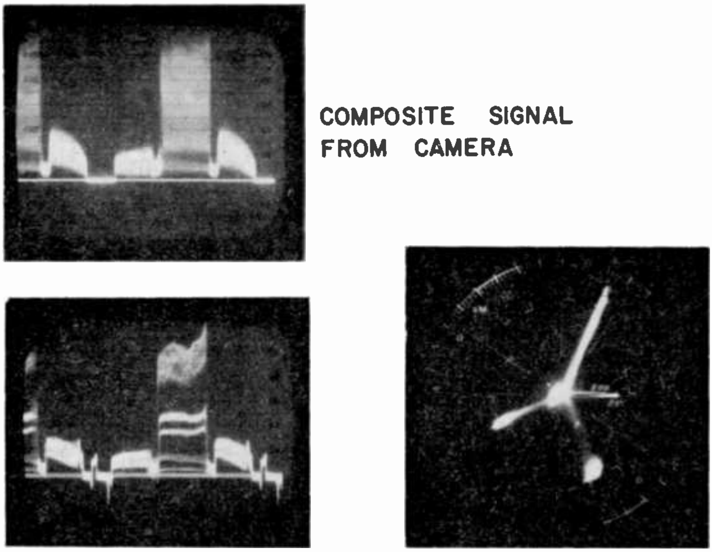

COMPOSITE SIGNAL FROM CAMERA

LUMINANCE CHANNEL

VECTORSCOPE PRESENTATION

Fig. 32(a)—System IV vector presentation and luminance signal.

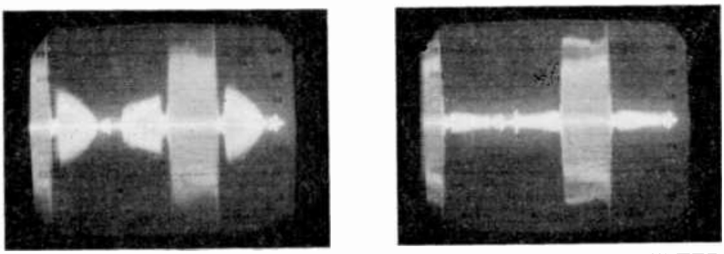

BAND-PASS FILTER OUTPUT

GREEN-COMB. FILTER OUTPUT

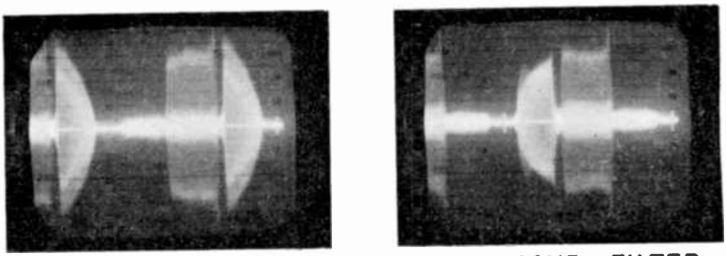

RED-COMB. FILTER OUTPUT

BLUE-COMB. FILTER OUTPUT

Fig. 32(b)—System IV color difference signals.

The fail-to-gray feature of the three-carrier systems is optimized in system IV since all three colors are treated essentially the same as the beam-spot size and/or shape is varied.

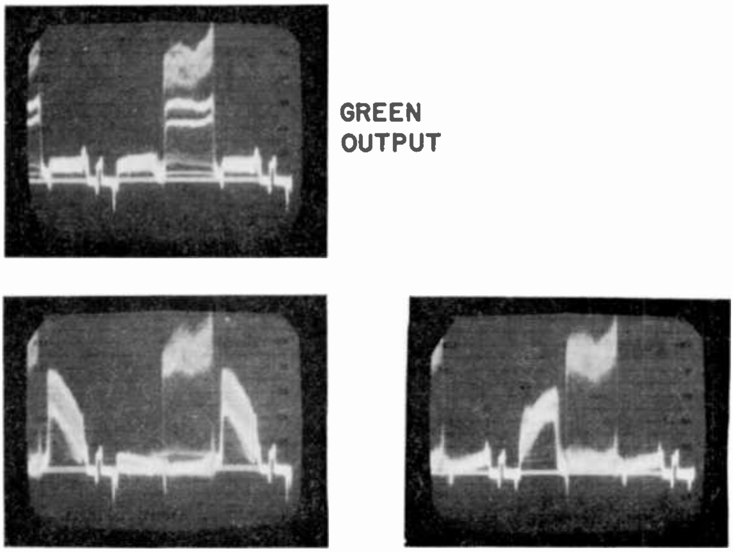

GREEN OUTPUT

RED OUTPUT

BLUE OUTPUT

Fig. 32(c)—System IV color output signals.

[c] Beats and Spurious Signals:

Since three consecutive scanning lines are compared in the comb-filter circuit of system IV, an interline beat of ⅓ of the horizontal line rate is generated. The visibility of this beat depends upon the degree of balance of the 2-H delay comb-filter circuit and must be maintained at least -40 dB to be acceptable. This requires careful compensation of the phase characteristic of the comb-filter circuits. The three signal paths (undelayed, delayed 1-H, and delayed 2-H) must have *matching* phase slopes over a frequency range at least equal to the expected variation in subcarrier frequency due to horizontal scan non-linearity. In the experimental setup, the phase characteristics were matched to within ± 5° over about a 400 kHz (± 200 kHz) range centered around the nominal value of the subcarrier frequency (4.2 MHz). Once this critical phase characteristic was realized in the intial design and adjustment of the comb-filter circuit, no difficulty was experienced in maintaining adequate rejection of the interline beat for scan non-linearities not exceeding 3%.

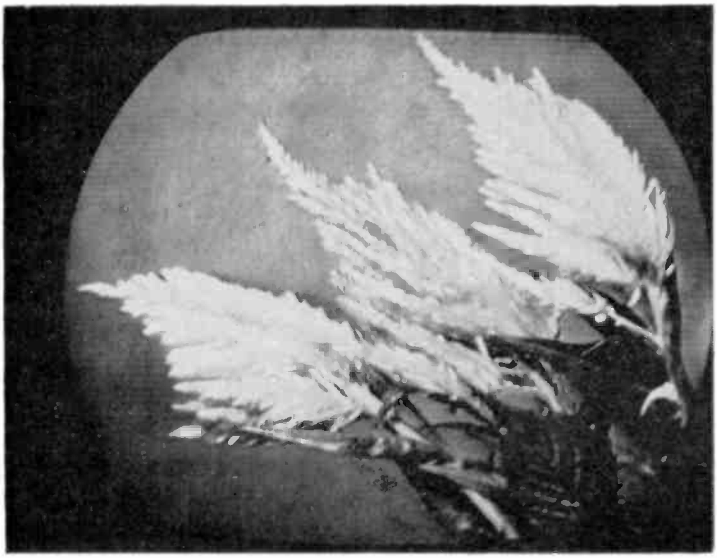

Fig. 33—Reproduction of slide using system IV.

10. Summary and Conclusions

Four representative stripe-color-encoded single-tube color TV camera systems were developed, constructed, and their relative performance characteristics were evaluated. The systems were in the amplitude-modulated color subcarrier category and included three versions of the fail-to-gray operational mode. Considerable care and attention was given to the physical test facilities to ensure the integrity of the comparative performance measurements.

The conclusion was reached that all four systems are capable of acceptable performance when properly implemented, with standard NTSC broadcast performance used as the measurement criteria. The fail-to-gray feature of systems II, III, and IV was found to be highly desirable when compared to the colorimetric failure-to-green characteristic of system I and the benchmark Kell/SRI system. Improved performance, relative to the reference Kell/SRI system, was shown in many areas such as signal-to-noise ratio, efficiency in use of available bandwidth, colorimetry, availability of inherent fail-to-gray feature, and versatility of possible applications.

Table 5 is a chart summarizing the various performance characteristics of all four systems.

Although the evaluation effort was limited to one-inch diameter vidicons employing antimony trisulfide as the photosensitive elements the knowledge gained is directly applicable to other pickup devices in larger sizes resulting in even better performance characteristics.

Each of the systems evaluated has individual potentials, as well as limitations that should be considered in the light of the specific application being considered. No one system appears to be the panacea for all possible applications.

Acknowledgment

The author gratefully acknowledges the contributions of many people at RCA Laboratories, the RCA Consumer Electronics Division at Indianapolis, Indiana, and at RCA Electronic Components, Lancaster, Pennsylvania, without whose efforts the work reported herein could not have been accomplished. Special mention should be made of the following contributors: J. J. Brandinger, for his interest and leadership as Laboratory Group Leader; A. C. Schroeder, for his technical insight and working contributions to the project; G. L. Fredendall, for his analytical work in the area of stripe-filter design; H. Hook and D. Hoffman, for their contributions to the technology of fabricating

Table 5—Summary of characteristics and performance of the various stripe-color camera systems.

SYSTEM	KELL/SRI	I	II	III	IV
1. Frequency Spectrum		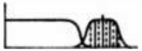		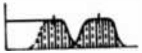	
2. Stripe-Color Filters	 Yellow Cyan	 Yellow Cyan Magenta	 Yellow Cyan Magenta	 Yellow Cyan Magenta	 Yellow Cyan Magenta
3. Stripe Orientation	0° @ 5 MHz 45° @ 3.5 MHz	± 21.5° @ 4.2 MHz	± 24° @ 3.6 MHz 0° @ 4.92 MHz	± 21.5° @ 4.2 MHz 44° @ 3.2 MHz	± 29° @ 3.85 MHz 0° @ 3.85 MHz
4. Spatial Frequency	5.0 MHz	4.45 MHz	3.95 MHz – 4.92 MHz	4.1 MHz – 4.2 MHz	4.4 MHz – 3.85 MHz
5. Optical Spatial Filter	3.5 MHz	4.2 MHz	3.6 MHz	4.2 MHz	3.85 MHz
6. Deflection System	Magnetic – GPL 1000	Magnetic – GPL 1000	Magnetic – GPL 1000	Magnetic – GPL 1000	Magnetic – GPL 1000
7. Gamma Compensation	Vidicon Composite Signal Linearizer	← Same	← Same	← Same	← Same
8. Optics	Relay	Relay	Relay	Relay	Relay
9. Vidicon	8507A	8507A	8507A	8507A	8507A
10. Comb Filter	None	1-H	1-H	2,1-H(Built), 1,1-H(Poss.)	2-H, Vert. Comp.'
11. S/N	R – 40.6 dB G – 45.2 dB B – 39.2 dB	R – 47.0 dB G – 53.0 dB B – 43.5 dB	R – 47.6 dB G – 51.1 dB B – 46.0 dB	R – 45.1 dB G – 51.1 dB B – 37.1 dB	R – 47.0 dB G – 53.0 dB B – 41.6 dB
12. Luminance Resolution	3.5 MHz	4.2 MHz	3.6 MHz	4.2 MHz	3.85 MHz
13. Chroma Resolution	500 kHz	500 kHz	500 kHz	500 kHz	500 kHz
14. Vert. Color Misregistry	None	1 Line	1 Line	1 Line	2 Lines (Comp.)
15. Large Area Color Uniformity	NTSC ± 20%, ± 10°	NTSC	NTSC	NTSC	NTSC
16. Color Failure Mode	To Green	To Green	To Gray	To Gray	To Gray
17. Comparative Color Uniformity	Poor	Fair	Excellent	Good	Excellent
18. Beats	1.5 MHz, - 36 dB	7.8 kHz, - 40 dB	7.8 kHz, - 40 dB 1.3 MHz, - 40 dB	7.8 kHz, - 40 dB 1.0 MHz, - 40 dB	5.25 kHz, - 36 dB
19. Lum./Color Crosstalk (2nd Order)	Magenta Beats	Magenta Beats	Fine Mixture & Interline	Fine Mixture & Interline	Fine Mixture
20. Light Utilization	2/3	2/3	1/2	1/2	1/2

dichroic stripe-filters; and to W. Sepp and R. Hassell, for their skill and tireless efforts in the construction and testing of the apparatus involved.

Appendix 1—1-H Delay Comb-Filter Fundamentals

A television signal is sampled at repetitive rates of 15.75 kHz, 60 Hz, and 30 Hz resulting from the horizontal and vertical scanning rates. A Fourier analysis of the signal indicates an energy spectrum concentrated at interval spacings of 15.75 kHz, with subsidebands grouped around each 15.75-kHz interval at multiples of 60 Hz and 30 Hz spacing. A second signal, such as the color subcarrier in a standard NTSC signal, may have its energy spectrum interleaved with the baseband spectrum by synchronizing the subcarrier with horizontal sync as an odd multiple of one-half line rate (3.579545 MHz in the case of NTSC).[11] In the same manner, two subcarriers may be interlaced with each other by causing them to have a 180° phase relationship with respect to each other when compared on a line-by-line basis.

Two independent pieces of information may be carried as amplitude modulation of the two carriers that are interlaced. At any one instant of time only one frequency exists, but the independent modulation sideband components may be separated when two scanning line periods are compared on a line-by-line basis by means of a comb filter comprised of a direct channel and a 1-H delayed channel.[4-7] Fig. 34 indicates the basic block diagram of a 1-H delay comb filter along with vector representations of the operation of the circuit in separating the information contained as amplitude modulation of carriers generated by scanning two-color stripe filters physically oriented so as to produce the required interlaced condition. Fig. 34(b) indicates the two directions of the stripe filters disposed symmetrically with respect to the vertical axis of the scanned raster. Both filters have the same pitch and are set at an angle such that a delay of 90° at the particular carrier frequency generated exists for the red filter, an advance of 90° occurs for the blue filter when compared on a line 1 to line 3 basis. Fig. 34(c) is a vector representation of this situation. In the comb-filter circuit, a 90° delay is introduced into the direct path, and the signals are added to the output of a 1-H delay line in one case and subtracted (180° inversion) from the 1-H delay signal in the second case. Thus, in one output the blue information in lines 1 and 3 add while the red information is canceled. At the same time the red information adds in the subtractor circuit while the blue is canceled, as is indicated by the vectors in Figs. 34(d) and (e). The equivalent amplitude-versus-frequency response is as shown in Fig. 35 for a 1-H delay comb filter using 1-H and 2-H delay elements.[4-7]

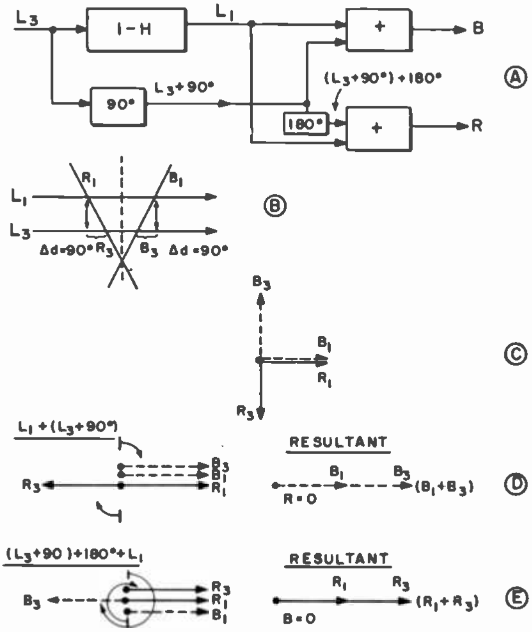

Fig. 34—Comb filter: (a) block diagram, (b) strip filters disposed symmetrically with respect to vertical axis of scanned raster, and (c), (d), and (e) resultant vectors.

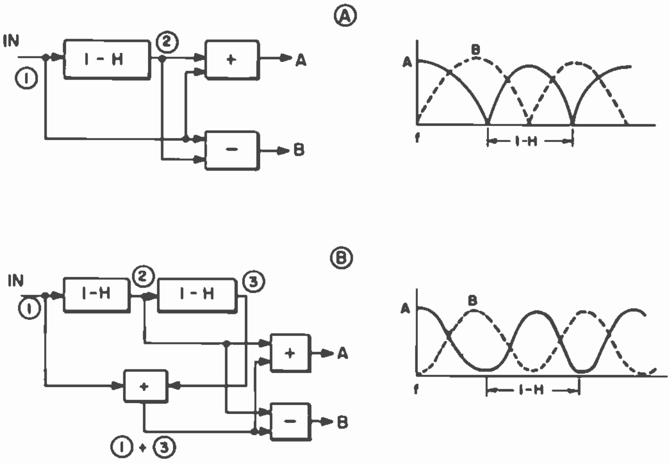

Fig. 35—Amplitude-versus-frequency response (a) for 1-H delay elements and (b) for 2-H elements.

The pitch of the stripe filters along with the standard line-scanning rate determines the absolute value of the subcarrier frequency generated by the scanning electron beam. If the stripe filters are oriented other than vertically, the component in the direction of horizontal scan determines the electrical frequency generated, while the actual pitch determines the spatial frequency. The relationship between the spatial frequency, the electrical frequency generated, and the angular displacement for the specific case of ± 90° delay (180° between two symmetrically displaced stripe filters) is shown in Fig. 36.

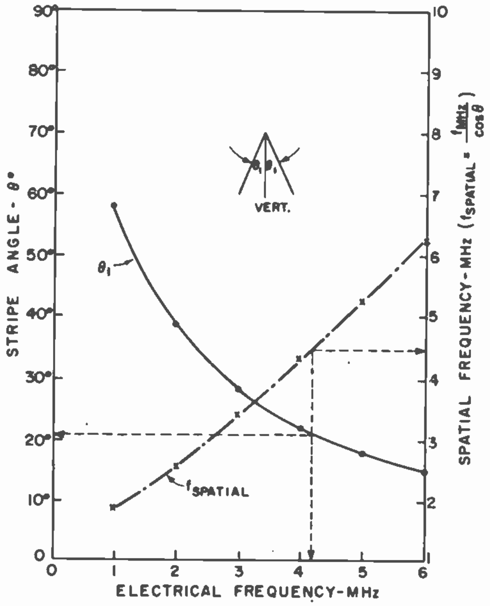

Fig. 36—Angular orientation of stripes versus electrical frequency and spatial frequency (180° relationship line-to-line).

The 1-H delay device employed is a quartz acoustic line with ceramic transducers obtained from an outside supplier and designated as DL45 (NTSC standards). The delay line is centered at 3.58 MHz with a bandwidth of about 2 MHz, an insertion loss of 8 dB, matching input and output inductors that result in an impedance of about 560 ohms, and a delay of 63.555 ± .005 μs.

In practical 1-H delay comb-filter circuits the desired-to-undesired signal ratio is in the range of at least 30 to 40 dB. Since the delay line has a fixed length, practical limits exist as to subcarrier frequency variations within one scan line, i.e., time jitter from one line to the next. Most commercial sync generators have a line-to-line horizontal stability in the order of 3-4 nanoseconds and are entirely satisfactory. Time jitter in excess of 8-10 nanoseconds causes 7.5-kHz horizontal striations (comb-filter imbalance) to be visible. This condition can exist in some industrial-quality sync generators. Fortunately, a simple and effective remedy is available. Driving the camera scanning circuitry from a fly-wheel horizontal circuit eliminates any line-to-line variations and requires only that the long-term time base be stable and controlled from a 3.58 MHz-crystal (in the case of NTSC standards).

Scan nonlinearity in the camera causes the frequency of the subcarrier generated by the stripe-color filters to vary along the horizontal scan line. The comb-filter circuit balance is reasonably insensitive to this type of error, since all frequency sideband components move together as the subcarrier changes value by small amounts (in the order of 1-5%) and if the slope of the phase characteristic in the direct path is made to match that of the delayed path over the range of the expected frequency variation plus sidebands. The equivalent amplitude-versus-frequency response of a single 1-H delay-line comfilter (correlates two scan lines) is in the form of a full-wave rectified sine wave as is shown in Fig. 35(a). The rejection ratio is more sensitive to frequency variation than that of a 2-H delay comb filter (correlates three scan lines) whose characteristic takes the form of a sine wave as shown in Fig. 35(b). A plot of rejection ratio versus percent frequency variation, shown in Fig. 37, indicates at least 10-to-1 difference in balance sensitivity in the practical range of 30 to 40 dB.

In camera systems that use a single 1-H delay-line comb filter to separate two pieces of color information, the signal contained in two adjacent scanning lines are correlated. Therefore, the vertical resolution of the *color signal* is reduced by a factor of 2 to 1 (4 MHz to 2 MHz). The luminance vertical resolution is unchanged however (4 MHz). A 2-H delay comb filter reduces the color vertical resolution by a factor of three, which is still well above the accepted horizontal color resolution of about 500 kHz.

The 1-H delay-line comb-filter technique provides a means for separating two interleaved pieces of color information and thereby effectively allows two color subcarriers and associated modulation sidebands to occupy the same band of frequencies. Therefore, considerable advantages result from the more efficient use of the available vidicon bandwidth. This approach has been used to good advantage in developing stripe-color camera amplitude-modulation systems.

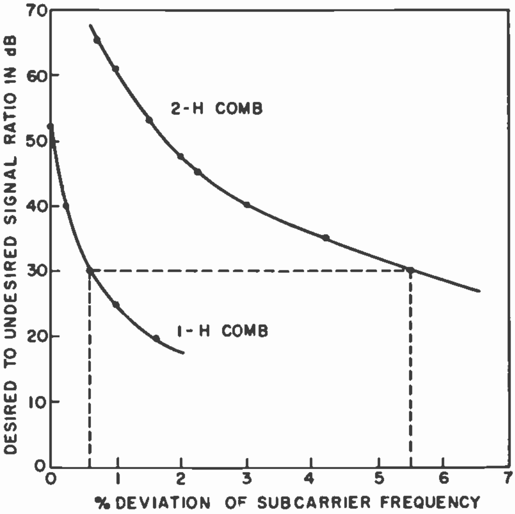

Fig. 37—Comb-filter rejection ratio versus percent subcarrier frequency stability.

Appendix 2—Special Color-Bar Test Slide

A special color test slide was developed to allow proper adjustment of the matrix circuitry of the decoder. The slide consists of a combination of Wratten filters, #24 red, #61 green and #98 blue, together with appropriate neutral density filters (see Fig. 38) to produce large-

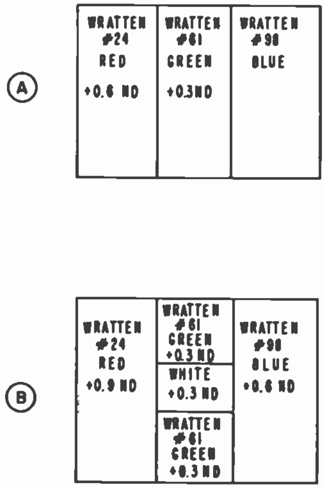

Fig. 38—Color-bar test slide.

arℯa red, green, blue, and reference white bars.

The luminance signal values are as follows:

a. Two stipe-color carrier systems:
   Luminance $= 0.50G + 0.25R + 0.25B$

b. Three stripe-color carrier systems:
   Luminance $= 0.60G + 0.30R + 0.20B$

The constants for the blue in the three-carrier system varied from about 0.1 to 0.2 depending upon the particular vidicon response involved when used with this test slide. The exact parameters to duplicate NTSC luminance values are:

$$Y(\text{Luminance}) = 0.59G + 0.30R + 0.11B.$$

References:

[1] C. D. Boltz and J. H. Wharton, private communication.

[2] G. L. Fredendall, "Filter Colorimetry for Single Tube Color Camera," **RCA Review,** Vol. 34, p. 267, March 1973 (this issue).

[3] Dr. W. Bruch, "PAL, a Variant of the NTSC Colour TV System," Selected papers from Telefunken Zeitung, NTZ Communications Journal, **Electronic Engineering.**

[4] G. L. Fredendall, private communication.

[5] M. A. R. Gunston and B. F. Nicholson, "Interdigital and Comb-Line Filters," **Marconi Review,** Vol. 29, No. 162, p. 133, 1966.

[6] Heinz E. Kallmann, "Transversal Filters," **Proceedings of the IRE,** pp. 302-310, July. 1940.

[7] B. D. Rukovich, "Linear-Phase Transmission Line Filters with Increased Selectivity," **IEEE Trans. Circuit Theory,** Vol. CT-17, No. 1, Feb. 1970.

[8] A. Macovski, **Encoded Color Systems,** Stanford Research Institute.

[9] T. Wagner, private communication.

[10] Albert Macovski, "Encoding and Decoding of Color Information," **Applied Optics,** Vol. 11, No. 2, Feb. 1972.

[11] Hazeltine Staff, **Principles of Color Television,** McIlwain and Dean Editors, John Wiley & Sons, Inc., 1956.

[12] FCC Compatible Color Order of December 1953, I. Section 3.682 **Transmission Standards,** paragraph (20)(VII).

[13] W. K. Hickok, "The Influence of Color Burst Variations on the Design and Performance of Color Receivers," Sylvania Electric Products, Inc., Batavia, New York.

[14] Jenkins and White, **Fundamentals of Optics,** McGraw-Hill Book Co., Inc., 1957.

[15] D. H. Pritchard, "Adjustable Bandwidth Optical Filter," Issued Patent #3,588,224(RCA).

Filter Colorimetry for Single-Tube Color Camera

G. L. Fredendall

RCA Laboratories, Princeton, N.J.

Abstract—An analytical determination of the spectral characteristics of the striped encoding filters in a single-tube color-camera system is derived by requiring that the system response to unit monochrome light trace out the camera sensitivity characteristics as the wavelength is varied. Calculations are made on the basis of NTSC sensitivities without negative lobes. Illuminant C is assumed.

Either two striped filters in sequence in the light path (cyan–clear alternating stripes and yellow–clear alternating stripes) or three striped filters (cyan–clear, yellow–clear, and magenta–clear) form a set of encoding filters by means of which color information is conveyed by amplitude-modulated carrier signals at the output of the camera tube. A baseband signal carries luminance information. In the case of two filters, the third color component, green, is regenerated by matrixing the envelopes of the two carrier signals and the luminance component. When three encoding filters are used, blue, green, and red information is transmitted as amplitude modulations of three carriers.

Although the magnitudes of the blue, green, and red components of the luminance signal may be specified arbitrarily, the NTSC specification $.11B + .59G + .30R$ is the appropriate choice.

In addition to the striped filters in each case, a uniform filter of prescribed spectral characteristic must also be placed in the light path.

Permissible variation in the transmission of an encoding filter as a function of wavelength is estimated by noting the extreme variations that give rise to NTSC color subcarriers that deviate no more than ten percent in amplitude and five degrees in phase from the true values for a representative range of subject colors. Such variations represent tolerances within which the spectral characteristic must be contained. In the case of a system encoded by a pair of striped filters, shifts of about ±10 nanometers along the wavelength axis appear to represent the tolerances to which the fabrication of the encoding filter should be held. In a triple-filter system, the tolerance is narrowed to about ±5 nanometers.

Introduction

A single color-camera tube operating with only one output terminal must possess a signal format from which the blue, green, and red signal components of the color picture may be isolated externally in the electrical circuits. The interposition of a set of appropriately designed and oriented striped color filters in the light path between subject and photosensitive target accomplishes this result.

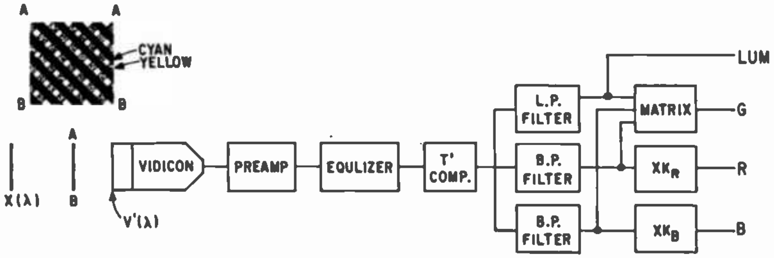

Fig. 1—Single-tube color-camera system employing two encoding striped filters.

One of the optical filters may be an alternate cyan and clear, transmitting, parallel-stripe pattern that causes the red component of a scene at the photosensitive surface of a camera tube to take the form of an amplitude-modulated square wave along the direction of scanning. When translated into an electrical signal by the scanning process, the red information is represented by the amplitude modulation of a carrier and a baseband signal. A camera system capable of full-color operation requires a second striped optical filter, in series with the first, with alternate yellow and clear transmitting stripes. If the second filter is considered to receive unattenuated blue light from the first filter, conditions are present for the generation of a baseband signal and a second electrical carrier signal that is amplitude modulated by the blue picture component. In the absence of a third striped filter, green portions of the scene are represented in the baseband (or luminance) signal. Appropriate matrixing of the luminance signal generated by the pair of striped filters and the amplitude detected signals yields the green signal. In addition to the striped filters, a uniform filter is also placed in the light path, a necessity explained below. Fig. 1 illustrates such a system. The angle of inclination and the pitch of the stripes determine the frequency of corresponding carrier signal.

In a second version of the single-camera-tube color system, three striped optical filters are positioned in a series arrangement for the

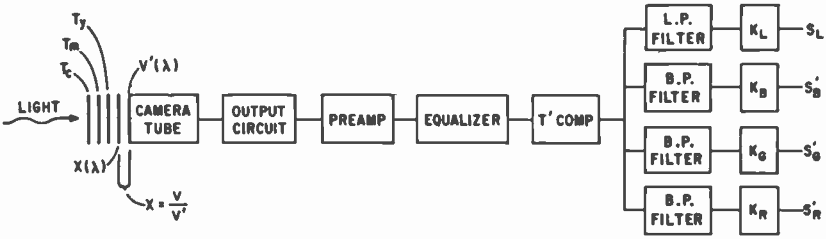

Fig. 2—Single-tube color-camera system employing three encoding striped filters.

generation of a baseband signal and three carriers amplitude modulated by blue, green, and red information, as illustrated in Fig. 2.

In the following discussion, a derivation of the spectral characteristics of the three striped filters and the required field filter is given.

Derivation of Optical Characteristics of Striped Filters

An analytical solution of the spectral characteristics of the optical encoding filters is accomplished by relating these characteristics to the camera-sensitivity characteristics corresponding to the receiver display chromaticities. The sensitivity characteristics imply that a monochrome color field of wavelength λ is faithfully reproduced on the monitor when the monitor input signals are proportional to the values corresponding to λ, as in Fig. 3* for the standard NTSC receiver chromaticities.

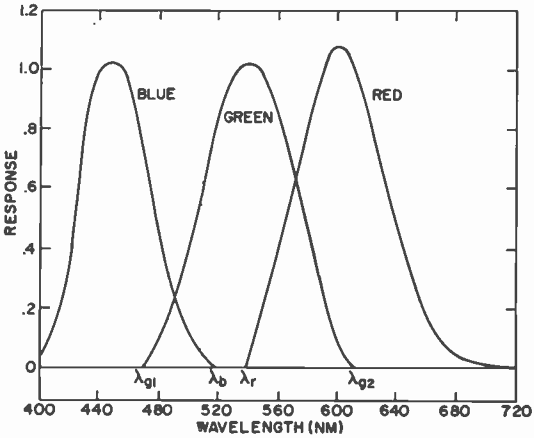

Fig. 3—Camera sensitivities in the standard NTSC system.

---

* Exact reproduction of a monochrome field requires accommodation of the negative lobes, which are not included in Fig. 1. See Ref. [1] and [2].

Hence, a condition of the solution of the encoding filters is that input of a unit monochrome field (λ) to the photosensitive target of the camera tube gives rise to the response values S_i for blue, green, and red given by the camera spectral sensitivities throughout the visible range.

We note that the variation in tranmission $\mathrm{TR}_i(\lambda)$ of the individual encoding filters in the x direction along a scanning line is a square wave

$$\mathrm{TR}_i(\lambda,x) = \frac{1+T_i(\lambda)}{2} + \frac{2}{\pi}\,(1-T_i(\lambda)) \sum_{n\ \mathrm{odd}} \frac{\sin n\pi/2}{n} \cos\,(2\pi xn/p_i), \qquad [$$

where p_i is the pitch of the stripes measured along the line and $\mathrm{i} = \mathrm{c}$ (cyan–clear), m (magenta–clear), and y (yellow–clear). $T_i(\lambda)$ are the normalized transmission factors of the color stripes of the encoding filters varying between 0 and unity. The overall transmission of three encoding filters in series, including the spectral characteristic $V(\lambda)$ of a uniform field filter representing the combination of the vidicon spectral response $V'(\lambda)$ and a trimming filter $X(\lambda)$, is

$$\mathrm{TR} = V(\lambda)\mathrm{TR}_c(\lambda)\mathrm{TR}_m(\lambda)\mathrm{TR}_y(\lambda). \qquad [2]$$

The charge pattern N created by the light quanta is proportional to the gamma power of the light amplitude along the scanning line i.e.,

$$N = kV^{\gamma}(\lambda)[\mathrm{TR}_c(\lambda)^{\gamma} \cdot \mathrm{TR}_m(\lambda)^{\gamma} \cdot \mathrm{TR}_y(\lambda)^{\gamma}], \qquad [3]$$

where

$$V(\lambda) = X(\lambda)V'(\lambda).$$

The degree of freedom represented by $V(\lambda)$ is necessary for achieving a solution for $T_i(\lambda)$.

Since $\mathrm{TR}_i(\lambda)$ possesses a square-wave form, we may write

$$\mathrm{TR}_i(\lambda,x) = \frac{1+T_i{}^{\gamma}}{2} + \frac{2}{\pi}\,(1-T_i{}^{\gamma}) \sum \frac{\sin\,(n\pi/2)}{n} \cos \frac{2\pi xn}{p_i}. \qquad [4]$$

As the charge pattern is scanned, a signal current S is generated that is proportional to the charge to a first order of approximation. Setting the line coordinate x_i equal to the product of the velocity of the scanning and the time t and further substituting $v = p_i f_i$ (where f_i is the frequency of the component of the signal corresponding to p_i), the expanded form of S from Eqs. [3] and [4] is

$$
\begin{aligned}
S = V'[&\frac{1}{8}(1+T'_c)(1+T'_m)(1+T'_y)\\
&+\frac{1}{2\pi}(1+T'_c)(1+T'_m)(1-T'_y)\cos(2\pi f_B t)\\
&+\frac{1}{2\pi}(1-T'_c)(1+T'_m)(1+T'_y)\cos(2\pi f_R t)\\
&+\frac{1}{2\pi}(1+T'_c)(1-T'_m)(1+T'_y)\cos(2\pi f_G t)\\
&+\frac{1}{\pi^2}(1-T'_c)(1-T'_y)(1+T'_m)\cos 2\pi(f_b-f_R)\,t\\
&+\frac{1}{\pi^2}(1+T'_c)(1-T'_y)(1-T'_m)\cos 2\pi(f_G-f_B)\,t\\
&+\frac{1}{\pi^2}(1+T'_c)(1+T'_y)(1-T'_m)\cos 2\pi(f_R-f_G)\,t\\
&+\frac{1}{9\pi^2}(1+T'_m)(1-T'_c)(1-T'_y)\cos 2\pi 3(f_B-f_R)\,t\\
&+\frac{1}{9\pi^2}(1-T'_m)(1+T'_c)(1-T'_y)\cos 2\pi 3(f_G-f_B)\,t\\
&+\frac{1}{9\pi^2}(1-T'_m)(1-T'_c)(1+T'_y)\cos 2\pi 3(f_G-f_R)\,t\\
&+\frac{2}{\pi^3}(1-T'_m)(1-T'_c)(1-T'_y)\cos 2\pi(f_G+f_R-f_B)\,t\\
&+\frac{2}{\pi^3}(1-T'_m)(1-T'_c)(1-T'_y)\cos 2\pi(f_G+f_B-f_R)\,t\\
&+\frac{2}{\pi^3}(1-T'_m)(1-T'_c)(1-T'_y)\cos 2\pi(f_G-f_R-f_B)\,t+
\end{aligned}
$$

+ (higher-order terms outside of the video pass band and of decreasingly small magnitude).

In the above expansion $T' = T^{\gamma}$. In the subsequent development, adequate gamma compensation is assumed such that $\gamma = 1$.

We refer now to the block diagram of the camera system shown in Fig. 2, where the color carrier signals represented by the fundamental components $\cos(2\omega f_i t)$ in Eq. [3] are isolated by electrical filters. Each component may be identified with a range of λ by noting that the coefficient $(1 - T_c)(1 + T_m)(1 + T_y)$ has maximum value in the blue range, $(1 + T_c)(1 + T_m)(1 - T_y)$ in the red range, and $(1 + T_c)(1 - T_m)(1 + T_y)$ in the green range. To identify the fundamental signal components more closely with the color range, we have replaced the subscripts c by R, m by G, and y by B in the trigometric arguments. The signal amplitudes at the system output terminals in Fig. 2 become

$$\frac{1}{2\pi} K_B V(1 + T_c)(1 + T_m)(1 - T_y) = S'_B$$

$$\frac{1}{2\pi} K_R V(1 - T_c)(1 + T_m)(1 + T_y) = S'_R$$

$$\frac{1}{2\pi} K_G V(1 + T_c)(1 - T_m)(1 + T_y) = S'_G \qquad [5]$$

$$\frac{1}{8} K_L V(1 + T_c)(1 + T_m)(1 + T_y) = S'_L$$

where K_i are appropriate gain factors. From Eq. [5], it follows that

$$\frac{S'_B}{S'_L} = \frac{4}{\pi}\frac{K_B}{K_L}\frac{(1 - T_y)}{(1 + T_y)};\ \frac{S'_G}{S'_L} = \frac{4}{\pi}\frac{K_G}{K_L}\frac{(1 - T_c)}{(1 + T_c)};\ \frac{S'_R}{S'_L} = \frac{4}{\pi}\frac{K_R}{K_L}\frac{(1 - T_m)}{(1 + T_m)}. \qquad [6$$

Solutions for T_c, T_y, and T_m are

$$T_y = \frac{1 - \frac{\pi}{4}\frac{S'_B}{S'_L}\frac{K_B}{K_L}}{1 + \frac{\pi}{4}\frac{S'_B}{S'_L}\frac{K_B}{K_L}},\quad T_c = \frac{1 - \frac{\pi}{4}\frac{S'_G}{S'_L}\frac{K_G}{K_L}}{1 + \frac{\pi}{4}\frac{S'_G}{S'_L}\frac{K_G}{K_L}},\quad T_m = \frac{1 - \frac{\pi}{4}\frac{S'_R}{S'_L}\frac{K_R}{K_L}}{1 + \frac{\pi}{4}\frac{S'_R}{S'_L}\frac{K_R}{K_L}}. \qquad [7$$

T_c, T_m, and T_y may be specified over certain ranges of the wavelength λ by inspection of the camera sensitivity characteristics S_i (Fig. 3) and tabulated as shown in Table 1.

Table 1—T_c, T_m, and T_y for Various Ranges of Wavelength λ

λ	T_c	T_m	T_y	Reason
$\lambda \leqslant \lambda_{g1}$	1	1		$S'_R(\lambda), S'_G(\lambda) = 0$
$\lambda \leqslant \lambda_{g1}$			0	Blue signal proportional to S'_B
$\lambda_{g1} \leqslant \lambda \leqslant \lambda_b$	1			$S'_R(\lambda) = 0$
$\lambda_b \leqslant \lambda \leqslant \lambda_r$	1		1	$S'_B(\lambda), S'_R(\lambda) = 0$
$\lambda_b \leqslant \lambda \leqslant \lambda_r$		0		Green signal proportional to to S'_G
$\lambda_r \leqslant \lambda \leqslant \lambda_{g2}$			1	$S'_B(\lambda) = 0$
$\lambda \geqslant \lambda_{g2}$	0			Red signal proportional to S'_R
$\lambda \geqslant \lambda_{g2}$		1	1	$S'_B(\lambda), S'_G(\lambda) = 0$

The required variation in $V(\lambda)$ over the complete range of the monitor spectral characteristics and of T_i over the ranges $\lambda_{g1} \leqslant \lambda \leqslant \lambda_b$ and $\lambda_r \leqslant \lambda \leqslant \lambda_{g2}$ is found by substitution in Eq. [7] from Table 1. As a condition that the gain factors K_i be independent of λ, the luminance signal must consist of a linear addition of S_i, namely,

$$S_L = C_B S'_B + C_G S'_G + C_R S'_R$$

in which C_i are arbitrary.

The tabulated values of T_i and V are listed in Table 2.

Since the spectral characteristic $V(\lambda)$ of the hypothetical camera tube is completely specified in Table 2, a trimming filter $X(\lambda)$ is called for in the real camera system in which the vidicon spectral characteristic may be $V'(\lambda)$ where

$$X(\lambda) = V(\lambda)/V'(\lambda).$$

The greatest light economy is achieved when a scale factor is applied to $X(\lambda)$ causing unity transmission at the wavelength of maximum transmission.

The spectral characteristics of the encoding filters T_c, T_m, and T_y and the theoretical camera filter $V(\lambda)$ shown in Figs. 4 and 5 were computed by means of formulas given in Table 2 for the NTSC specification of the luminance signal ($.11\,S'_B + .30\,S'_R + .59\,S'_G$) and the frequently mentioned combination ($.25\,S'_B + .25\,S'_R + .50\,S'_G$). The trimming filter $X(\lambda)$ appropriate for the compensation of the published spectral characteristics of the RCA vidicon type 8507 is shown in Fig. 6.

Table 2—Values of T_i and V for System Employing Three Encoding Filters

λ	$T_c(\lambda)$	$T_m(\lambda)$	$T_y(\lambda)$	$V(\lambda)$
$\lambda \leqslant \lambda_{g1}$	1	1	0	$2C_BS'_B$
$\lambda_{g1} \leqslant \lambda \leqslant \lambda_b$	1	$C_BS'_B/(2C_GS'_G+C_BS'_B)$	$C_GS'_G/(2C_BS'_B+C_GS'_G)$	$\dfrac{(2C_GS'_G+C_BS'_B)(2S'_BC_B+C_GS'_G)}{C_GS'_G+C_BS'_B}$
$\lambda_b \leqslant \lambda \leqslant \lambda_r$	1	0	1	$2C_GS'_G$
$\lambda_r \leqslant \lambda \leqslant \lambda_{g2}$	$C_GS'_G/(2C_RS'_R+C_GS'_G)$	$C_RS'_R/(2S'_GC_G+C_RS'_R)$		$\dfrac{(2C_GS'_G+C_RS'_R)(2C_RS'_R+C_GS'_G)}{C_GS'_G+C_RS'_R}$
$\lambda \geqslant \lambda_{g2}$	0	1	1	$2C_RS'R$

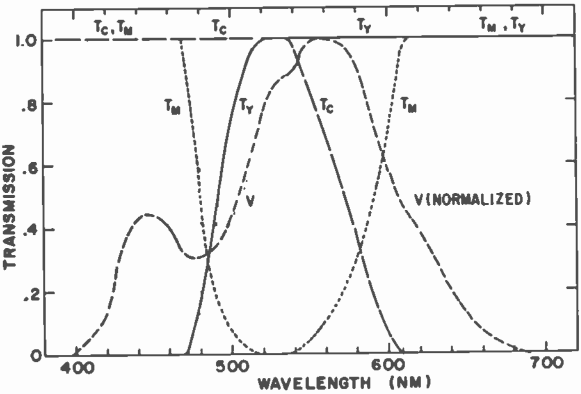

Fig. 4—Spectral characteristics of the encoding filters in the three-striped-filter systems (luminance signal $= .25E_R + .50E_G + .25E_B$).

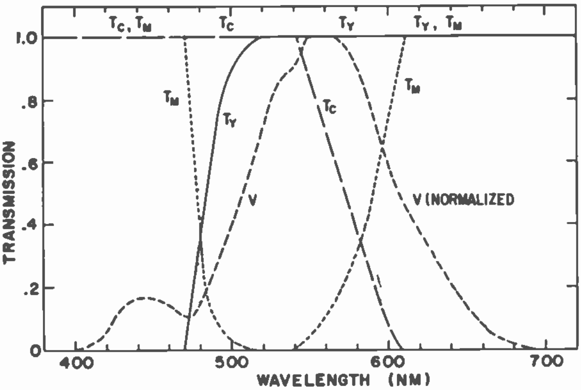

Fig. 5—Spectral characteristics of the encoding filters in the three-striped-filter systems (luminance signal $= .30E_R + .59E_G + .11E_B$).

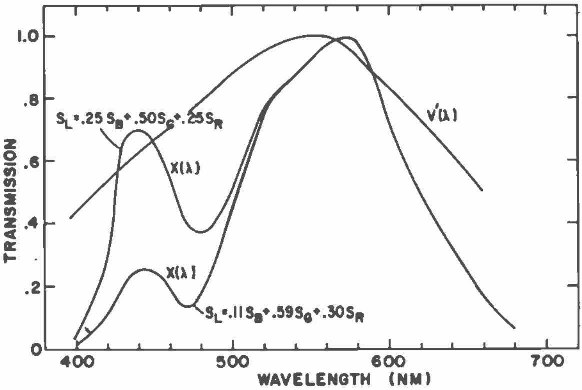

Fig. 6—Trimming filter $X(\lambda)$.

Table 3—Values of T_i and V for System Employing Two Encoding Filters

λ	$T_c(\lambda)$	$T_y(\lambda)$	$V(\lambda)$
$\lambda \leqslant \lambda_{g1}$	1	0	$2C_BS'$
$\lambda_{g1} \leqslant \lambda \leqslant \lambda_b$	1	$C_GS'_G/(2C_BS'_B+C_GS'_G)$	$2C_BS'_B+C_GS'_G$
$\lambda_B \geqslant \lambda \geqq \lambda_R$	1	1	$C_GS'_G$
$\lambda_R \geqslant \lambda \geqq \lambda_{g2}$	$C_GS'_G/(2C_RS'_R+C_GS'_G)$	1	$2C_RS'_R+C_GS'_G$
$\lambda \geqslant \lambda_{g2}$	0	1	$2C_RS'_R$

A single-camera-tube system employing only two encoding filters, T_c and T_y, derives the green signal by a matrix operation on the luminance signal and the blue and red signals as referred to previously in Fig. 1. Solutions for T_c, T_y, and V are obtained from Eqs. [7] and Table 1, as before, except that T_m is set equal to unity for all λ. The results are listed in Table 3. It is noted that formulas for T_c and T_y are unchanged. The camera spectral response $V(\lambda)$ shown in Fig. 7 differs in the intervals $\lambda_{g1} \leqslant \lambda \leqslant \lambda_b$ and $\lambda_r \leqslant \lambda \leqslant \lambda_{g2}$.

Tolerances in Spectral Characteristics of Encoding Filters

The wavelength sensitivities of the spectral characteristics of the cyan–clear, magenta–clear, and yellow–clear encoding filters to shifts along the wavelength axis were investigated by calculating the change in amplitude and phase of the NTSC subcarrier corresponding to various

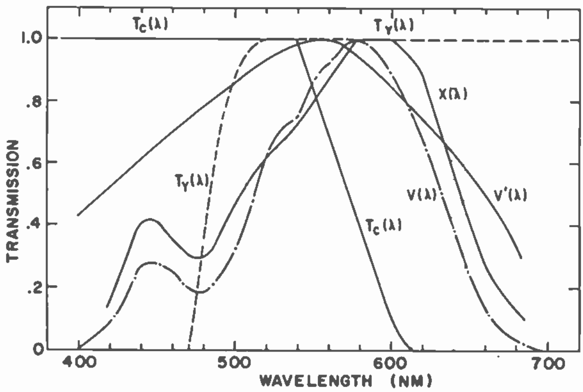

Fig. 7—Spectral characteristics of encoding filters and field filter.

uniform color test fields as indicated in Fig. 5. This calculation calls for the determination of system outputs for monochrome inputs as given by the first four terms of Eq. [3] and integration over the spectrum of each test field. The gain in each color output channel of the system was standardized to yield unit voltage output when the uniform field was illuminant C. The standard formulas for computation of amplitude and phase angle of the NTSC color subcarrier were used.* Locations of 15 test colors are shown in the color triangle of Fig. 8. Three artificial test colors not identified in the triangle are given the same spectral characteristics as the camera sensitivities where the maximum response is taken as 100% reflectance.

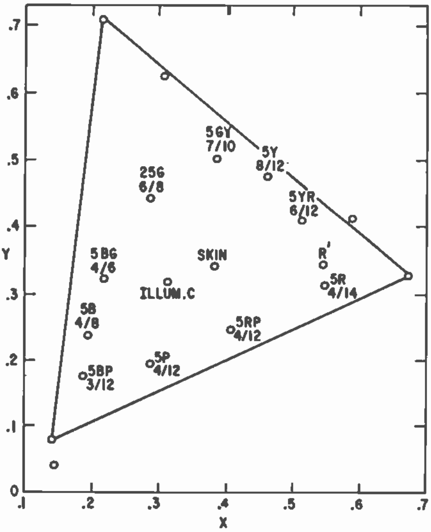

Fig. 8—Positions of the Munsell colors in the color triangle formed by the NTSC primaries.

The Federal Communications Commission tolerances for broadcasting the NTSC subcarrier are ± 20% in amplitude and ± 10° in phase angle. These tolerances provide accepted color in pictures; wider tolerance limits would produce unacceptable shift changes in picture colorimetry. For an added margin of performance, tolerance limit of ± 10% in amplitude and ± 5° in phase were considered in this study.

These results are summarized in Table 4 and are commented upon as follows:

---

* See Ref. [2], p. 553.

Case 1

The reference values for amplitude and phase of the NTSC subcarrier corresponding to the test colors are established in Case 1 for the ideal encoding filters and field filter characteristic $V(\lambda)$. Variations from the ideal spectral description of these filters result in deviations in the subcarrier from the reference carrier. These deviations are recorded in Table 4 for a variety of assumed tolerances.

Table 4—Extreme Variation of NTSC Subcarrier from Subcarrier Corresponding to the Ideal Stripe Specifications (All Test Colors Included)

Case	Field Filter	Stripe Filter Condition $TC_{A,B,C}$	$TY_{A,B,C}$	$TM_{A,B,C}$	Extreme Variation of NTSC Subcarrier Angle (Deg.)	Amplitude (%)
1	$V(\lambda)$	0,0,0	0,0,0	0,0,0	Reference	Reference
2	$V'(\lambda)$	0,0,0	0,0,0	0,0,0	10 to −11	12 to −47
3	$V(\lambda)$	85,5,0	85,5,0	80,5,0	2 to −3	0 to 10
4	$V'(\lambda)$	85,5,0	85,5,0	80,5,0	11 to −11	28 to −33
5	$V(\lambda)$	85,5,+10	85,5,−10	80,5,+10	1 to −10	11 to −13
6	$V(\lambda)$	85,5,+10	85,5,−10	80,5,−10	8 to −10	14 to −9
7	$V(\lambda)$	85,5,+5	85,5,−5	80,5,+5	5 to −6	8 to −9
8	$V(\lambda)$	85,5,+5	85,5,−5	80,5,−5	6 to −6	−7 to −13

Key:	$V(\lambda)$	denotes the theoretical spectral response of the camera tube.
	$V'(\lambda)$	denotes the vidicon spectral characteristic used as field filter for test.
	$TC_{A,B,C}$	denotes that the cyan-clear striped filter had A percent transmission, B percent rejection, and +C millimicrons transition of ideal spectral characteristic to the longer wavelengths or −C translation to the shorter wavelengths.
	$TY_{A,B,C}$	denotes yellow–clear stripe filter.
	$TM_{A,B,C}$	denotes magenta–clear stripe filter.

Case 2

Conditions of Case 1 were maintained with the exception of substitution of the vidicon spectral characteristic for $V(\lambda)$. Variations of the NTSC subcarrier from reference amplitude and phase were +12 and −47% and +10° and −11°.

Case 3

Modification of the theoretical encoding filters for 85% transmission for cyan and yellow stripes, 80% for magenta stripes, and 5% rejection for each encoding filter calls for matrixing of blue and luminance and red and luminance in order that the dilution caused by incomplete transmission and rejection may be eliminated. With the theoretical field filter characteristic, the deviation in the NTSC subcarrier amounted to 0 to 10% and +2° to −3°.

Case 4

Substitution of the vidicon spectral characteristics for the field filter characteristic in Case 3 introduced variations of about +11° in the phase of the NTSC color subcarrier and −28 to +33% in the amplitude for the range of test colors.

Cases 5 and 6

Tolerances represented by shifts of −10 nm in the cyan spectral characteristic, +10 nm in the yellow, and ±10 in the magenta result in deviations in amplitude and phase of the subcarrier that exceed the marginal limits of ±5° and ±10%.

Cases 7 and 8

These cases tend to indicate that the tolerable limits on shifts in the spectral characteristics of the encoding filters in a three filter system are ±5 nm if the limits of ±5° and ±10% are placed on the variation of the NTSC color subcarrier.

Conclusions

The tolerances on the spectral characteristics of the encoding filters appear to be ±5 nm provided a trimming filter is used. Although further exploration within the tolerance limits is indicated, the assumption appears to be reasonable. This limit is contrasted with a tolerance of ±10 nm found to exist for a two-encoding-filter system under test conditions similar to those in Table 3, but not reported here. The reduction of tolerance in the case of three encoding striped filters is understandable, since three encoding filters are involved in a multiplicative type of action, whereas in the other case only two filters are involved.

References:

[1] **Principles of Color Television**, Hazeltine Staff, p. 73, John Wiley and Sons, N.Y., N.Y. (1956).

[2] D. H. McRae, "High-Quality Color Rendition in Color Telecine," **J. SMPTE**, Vol. 78, p. 140, March 1969.

Low-Frequency 1/f Noise in MOSFET's*†

R. S. Ronen
RCA Laboratories, Princeton, N.J.

Abstract—Measurements of low-frequency 1/f noise on bulk and SOS MOSFET's are described. The devices were operated in the current-saturation region; the noise results were examined relative to existing theories. The dependence of input-referred noise voltage, $\tilde{e}_n$, on geometry, bias, temperature, and source resistance is examined, and is shown to fit theoretical expectations. Dependence of $\tilde{e}_n$ on oxide thickness and surface-state density is inconclusive, particularly in SOS MOSFET's, which exhibit larger 1/f noise than identical bulk devices. A comparison of MOSFET's and commercial low-noise JFET's is also made.

We show that when clean thin oxides are used, conventional low-threshold p-MOSFET's (COS/MOS series) demonstrate low-noise (< 20 nV/$\sqrt{\text{Hz}}$ at 1 kHz) operation, low cross-over frequency ($< 10^4$ Hz), and high uniformity of results. Their noise-voltage dependence on drain current, source resistance, and temperature is small, making them attractive as small-signal amplifiers fed by high-impedance sources and capable of operating over a wide temperature range. Moreover, ways to obtain low-noise SOS MOSFET's are also examined. Possible applications are discussed briefly.

---

* This work was supported in part by the Air Force Avionics Laboratory, Wright-Patterson Air Force Base under Contract No. F33615-71-C-1748 and by RCA Laboratories.

† Sections of this paper appear as part of a dissertation that has been submitted to Brooklyn Polytechnic Institute in partial fulfillment for the degree of Ph.D. 1973.

1. Introduction

Low-frequency $1/f$ noise is a universal phenomenon prevalent in all electronic devices where different materials are in contact; the different "material" may be a vacuum, a different alloy, or a differently doped semiconductor. The number of carriers flowing through, or parallel to, such an interface usually fluctuates due to various mechanisms such as generation–recombination or trapping. When the range of time constants for such fluctuations is large, the resulting noise may span many orders of magnitude over a very wide frequency range. Since MOS transistors are surface devices with a complex potential distribution at the SiO_2-Si interface, particularly when they are operated in saturation, low-frequency $1/f$ noise is expected to be a major source of noise below some frequency f_o. MOSFET's are majority-carrier high-impedance devices with essentially capacitive input; they can easily be integrated, even on dielectric substrates, such as silicon on sapphire (SOS), and perform well at cryogenic temperatures, where bipolars are not useful. Hence, they are very attractive as amplifiers for high-impedance signal sources, such as various radiation detectors, many of which operate at liquid-nitrogen temperatures. Unfortunately, operation at low frequencies normally extends below f_o for MOSFET's, thus including a very noisy part of the spectrum.

The object of the work described here was to determine the feasibility of using MOSFET's as small-signal amplifiers in cryogenic systems, where high input impedance, high signal-to-noise ratio, and ease of integration are important considerations. We have examined $1/f$ noise in various MOSFET's and compared it to that in low-noise commercial JFETs. RCA's silicon-gate p-MOSFET's with a channel width of 63 mils, exhibit an input-referred noise voltage $e_n < 15$ nV/$\sqrt{\text{Hz}}$ at $f = 1$ kHz, drain current $I_D = 1$ mA, and drain–source voltage $V_{DS} = 10$ V, and have $f_o < 5$ kHz. Identical devices in SOS exhibited one to two orders of magnitude higher noise, with the best results obtained on thick-film thin-oxide devices. Very large low-noise JFET's exhibited lower $\tilde{e}_n$, but had much higher input capacitance and conductance. Uniformity of the results on the bulk MOSFET's was excellent; somewhat poorer uniformity was obtained in SOS MOSFET's, and very large standard deviation was noticed on the several JFET's under investigation.

Variations of noise voltage resulting from changes in drain current, drain voltage, and temperature were very small, as had been expected. The effect of gate area A on noise was also confirmed for both bulk and SOS devices ($\tilde{e}_n^2 \sim A^{-1}$), but the effect of using thinner oxides was more pronounced than expected in reducing the noise. This is especially true for SOS devices, and is attributed to the dependence of N_{ss}, the fast-surface-state density, on oxide thickness t_{ox}. It is concluded that the product $P_{ss} = N_{ss}t_{ox}$ has to be minimized to reduce $\tilde{e}_n$. Possible applications of MOSFET's as amplifiers are also examined briefly.

2. Theory

The general theory of noise in semiconductor devices has been treated by various authors over the last two decades.[1] Specifically, $1/f$ or flicker noise, which is universally found in active and passive devices has been discussed in some detail.[2-6] More recent approaches have treated $1/f$ noise spectrum in MOSFET's in terms of specific modes of operation, e.g., the ohmic region[5,7] or the saturation region,[8] with efforts to explain the very wide frequency spectrum of the $1/f$ noise[7,9,10] known to extend several decades below 1 Hz.[11]

Derivation of $1/f$ noise behavior in FETs is based on McWhorter's theory[3] modified to say that free carriers are randomly trapped at the SiO_2-Si interface by means of a tunneling process into the oxide.[4,5,7] An expression for the spectral intensity of the trapping mechanism is given by van der Ziel[12] for an assumed distribution of (N_t, τ):

$$S_N(\omega) = \frac{N_t A d_t}{\omega \ln(\tau_1/\tau_0)} [\tan^{-1}(\omega\tau_1) - \tan^{-1}(\omega\tau_0)], \qquad [1]$$

where $\omega = 2\pi f =$ angular frequency

$N_t =$ trap density in the oxide at dy from the interface

$A =$ surface area of the inverted channel

$d_t =$ distance into oxide where traps are effective

$\tau_1, \tau_0 =$ maximum and minimum values of the characteristic time constant of trapping mechanisms.

The quantities τ_0, τ_1, and d_t are known from calculations based on several experiments, e.g., under uniform inversion, $0 < x \leqslant d_t = 20$ Å.[13] Eq. [1] has a $1/f$ behavior for $1/\tau_1 \ll \omega \ll 1/\tau_0$ (which is a very wide range), because[5]

$$\tau_1 = \tau_0 \exp(\alpha x) > 10^{17},$$

where $\alpha \equiv (4\pi/\hbar)(2m^*E_B)^{1/2} \simeq 2 \times 10^{-8}\,\text{cm}^{-1}$. Here $\hbar$ is Plank's constant, m^* is the effective mass of the carriers, and E_B is the energy barrier to be tunneled by the carriers. Using the same theory, the general form of the current spectral density in MOSFET's is[5]

$$i_n^2 = 4\left(\frac{qI_D}{L}\right)^2 W \int_{E=-\infty}^{\infty}\int_{x=0}^{L}\int_{y=0}^{t_{ox}} N_t \frac{f_t(1-f_t)}{g([V(x)]^2}\frac{\tau}{(1+\omega^2\tau^2)}\,dy\,dx\,dE, \qquad [2]$$

where L,W = channel length, width

q = electronic charge

E = energy

f_t = fractional occupation of trapping centers

$V(x)$ = potential along the channel.

Since $N_t = N_t(y,E)$

$f_t = f_t(y,E)$

$\tau = \tau(x,y,E)$,

evaluation of the integrals requires knowledge of the energy and geometry dependencies for every set of bias conditions (see Fig. 1), i.e., heavy uniform inversion ($0 \cong V_{DS} \ll V_{GT}$), onset of current saturation ($V_{DS} \cong V_{GT}$), and deep saturation ($0 < V_{GT} \ll V_{DS}$). Most authors consider only the first region, where the device behavior is well understood. Assuming uniform inversion and N_t = constant for $0 < y < d_t$, one can obtain[5,7] with τ exponentially dependent only on y and E,

$$\bar{i}_n^2 = \left(\frac{4q^2g_m^2}{C_{ox}^2\,WL}\right)\left(\frac{1}{4\alpha f}\right)F(V_{DS})N_t \cong \left(\frac{qg_m}{C_g}\right)^2\frac{kTA}{\alpha f}N_t(E_f) \qquad [3]$$

when $\frac{1}{\tau}\exp(-\alpha d_t) << \omega << \frac{1}{\tau}$

where g,g_m = conductance, transconductance

$C_{ox} = \epsilon_{ox}/t_{ox} \equiv Cg/A$

ϵ_{ox} = permittivity of the oxide

k = Boltzmann's constant

T = absolute temperature

$N_t(E_f)$ = actual trap density near the Fermi level

The second part of Eq. [3] also recognizes $\Delta E = E_f \pm 2kT$ to be the only range of energy in which the traps contribute appreciably to the noise and allows $N_t(E_f) = 4V_{th}N_{ss}/dt$ ($V_{th} = kT/q$ is the thermal voltage) to be the average trap distribution within that range.

The input-referred noise-voltage spectral density, e_n^2, has the form

$$\tilde{e}_n^2 \equiv \frac{\tilde{i}_n^2}{g_m^2} \sim \left(\frac{q}{C_g}\right)^2 \frac{A}{\alpha f} N_t. \qquad [4]$$

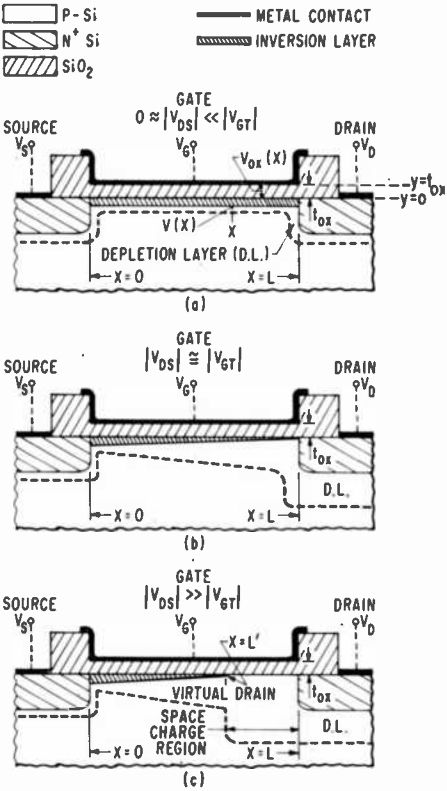

Fig. 1—Modes of operation in MOSFET's—physical structural changes: (a) linear (ohmic) region, uniform inversion; (b) threshold of current saturation; and (c) full current saturation.

One must remember that in small-signal applications, MOSFET's are normally operated in the saturation region, i.e., $0 < V_{GT} \ll V_{DS}$. The inversion layer and surface potential are nonuniform, and field and trap distribution around and beyond the virtual drain point, Fig. 1(c), are not uniquely known. However, since $1/f$ noise was found to saturate with drain current, investigators took the view that it is generated in the inverted part of the channel, and that the theories described by the foregoing equations can be extended to include the saturation region. However, since $N_t(E)$ is not known exactly (in saturation), different and possibly more accurate theories are possible. Acknowledging the complexity involved, several authors took a somewhat different approach. Considering the trap density in the oxide N_t to be proportional to the density of free carriers N_{free}, with γ being the proportionality coefficient ($N_t = \gamma N_{\text{free}}$) and $\bar{\gamma}$ the average value of γ in the channel, Klaassen[8] gives

$$e_n^2 \sim \bar{\gamma}\frac{qV_{GS}}{C_g f}, \qquad 0 < V_{GT} \ll V_{DS}. \qquad [5]$$

The difference between Eqs. [4] and [5] results from the different conditions used in the derivations and will be examined subsequently.

Several more recent approaches should also be mentioned in concluding this brief theoretical discussion. Fu and Sah[9] and Hawkins[10] explained the large frequency range of $1/f$ noise by modifying previous theories (e.g. two-stage tunneling[9] or two distinct trap energy bands[10]). A. Rose[14] derived an expression for $\tilde{e}_n^2$ based on his previous concept of photon counting;[15] groups of trapped electrons characterized by lifetimes τ_0, $2\tau_0$, $4\tau_0$, etc., are in communication with free electrons, the total number per time slot being N. Rose's approach gives rise to $1/f$ type noise, and an expression similar to that of Klaassen.* North's approach,[16] on the other hand, pre-supposes the existence of $1/f$ noise in MOSFET's as a universal phenomenon between any two dissimilar materials. He proceeds to derive the input-referred noise voltage as a small perturbation in the surface potential that leads to a corresponding perturbation in drain current. His result* states that

$$\tilde{e}_n^2 = \frac{q}{C_g} V_T \ln\left(V_{GT}/V_{th}\right) \Psi(f), \qquad 0 < V_{GT} \ll V_{DS}, \qquad [6]$$

---

* The derivation of Rose's expression and of North's expression (Eq. [6]) are given in the appendixes of Refs. [20] and [34].

where V_T is the threshold voltage and $\Psi(f) \equiv K/f =$ the frequency dependent noise term. Clearly this result differs from all previous results, and has an unknown quantity, K.

3. Summary and Examination of Theories

Before presenting our experimental observations and conclusions, a short review of the salient points of the above theories is in order. It appears that a general expression for input-referred noise spectral density can have the following form:

$$\tilde{e}_n^2 = C_N F_1(W,L,t_{ox}) F_2(V_{GS}, V_{DS}, N_t, f) \qquad [7]$$

where: $C_N =$ constant

$F_1 =$ a geometry factor

$F_2 =$ function of bias, processing, and frequency

We may now sum up the salient features of the foregoing theories.

[a] $\tilde{e}_n^2$ is inversely proportional to the channel area, i.e., $\tilde{e}_n^2 \sim 1/A = 1/WL$.

[b] $\tilde{e}_n^2$ is proportional to t_{ox}^2 (e.g. Christenson[5] and Hsu[7]) or to t_{ox} (e.g. Klaassen,[8] Rose,[14] North[16]), subject to the distribution and bias dependency of N_t.

[c] From a and b above, we may state that $F_1 \sim A/C_g^2$, or $F_1 \sim 1/C_g$, depending on N_t.

[d] $\tilde{e}_n^2$ measured in saturation is almost independent of the drain voltage V_{DS}, i.e., it essentially saturates with drain current I_D. It is dependent, however, upon the effective gate voltage V_{GT}, either linearly (Klaassen[8]) or logarithmically (North[16]). All theories, then, show a very weak dependence of the noise voltage $\tilde{e}_n$ on drain voltage and current for saturated devices. Note that the thermal noise of MOSFET's, which is associated with channel conductance, decreases with drain current.

[e] The noise spectral density is proportional to N_t and therefore to N_{ss}, the fast surface state density. Both are not uniquely known, are dependent largely on processing, and are not simple or always possible to measure.

[f] The $1/f$ noise is generated in the channel, appearing as a current source at the output. A physical voltage source at the input, if

any, has a very small overall effect. Moreover, signal-source resistance has no effect on the *inherent* $1/f$ noise generation of the device up to certain high values where feedback becomes important. *This contrasts with noise generation in bipolar transistors.*

[g] $1/f$ noise in MOSFET's is dominant from well below 1 Hz to well above 10^3 Hz in present commercial devices.[11] The lower frequency limit of $1/f$ noise has not been determined.

[h] Temperature dependence of $1/f$ noise is theoretically rather complicated.[5,17] Because FET's are good amplifiers at low temperatures, interest in their noise behavior in the wide range $77°K < T < 300°K$ always existed. Assuming a negligable change in geometry or dielectric constant at cryogenic temperatures, the two factors that contribute to changes in the noise are change in the amplitude and occupation index of N_t and change in effective mobility, μ. The theoretical dependence of mobility on temperature is $\mu \cong T^{-3/2}$, and it can be measured by evaluating small-signal conductance ($g_{do} = g_d$ as $V_{DS} \rightarrow 0$) at different temperatures. Again, with the devices operated as amplifiers, both V_{DS} and V_{GT} are not trivial; they are many kT/q (i.e., the thermal voltage); and since the surface is not uniformly inverted, μ_{eff} obtained this way must be interpreted carefully and may be of limited use. However, since $\tilde{e}_n{}^2$ is independent of μ_{eff}, its only principal dependence is on N_t (or alternatively N_{ss}). Various measurements have been reported in the literature[17-19] and attempts have been made to explain the different changes in $\tilde{e}_n$ with temperature in p- and n-MOSFET's. Independent measurements of N_{ss} at low temperatures by the use of threshold versus temperature method are not sensitive enough below $N_{ss} = 10^{11}$ $eV^{-1}cm^{-2}$. Moreover, with low density and uniform distribution of traps, one would assume a small dependence of $\tilde{e}_n$ on temperature, as indeed several recent papers have reported.[8,18,20] Since we expected the devices discussed here to fall into this category, we shall not further pursue this subject.

[i] To minimize $\tilde{e}_n$, both N_{SS} and t_{ox} must be minimized, and the area A maximized. Increasing A by increasing either L or W or both has its limitation, i.e., gain–bandwidth considerations, load and source impedance, and "real-estate" constraints must be considered. Thus, t_{ox} and N_{SS} are the only intrinsic qualities that can be minimized. Das,[27] in fact, uses the product $P_{SS} = N_{SS}t_{ox}$

as an inherent figure of merit; with the apparent dependence of N_{SS} on t_{ox} for thin-oxides, such a product is even more meaningful.

Having summarized some of the important features of the various theories, we can address ourselves to the experimental results and examine them in light of these theories. Most measurements were carried out with the MOSFET's operated well into current saturation.

4. Experimental Setup and Procedure

A block diagram of the experimental setup is shown in Fig. 2. Provision was made to measure noise on encapsulated devices and on wafers below 1 MHz; noise values recorded on identical MOSFET's in either form differed by less than 10%. Low-temperature noise measurements were carried out on encapsulated devices in a well-shielded isothermic bottle. The measuring system consists of two branches. One branch is a commercial low-noise amplifier and filter that yields spot values of $\tilde{e}_n$ (10 to 10^5 Hz) directly by measuring the noise current and the overall small-signal gain at a specific frequency within the band. These spot noise measurements are very valuable in the $1/f$ region where $\tilde{e}_n$ changes rapidly. The second branch of the system consists of an amplifier and a tuned filter with $f = 10$kHz to 30MHz and a choice of $\Delta f = 0.5$ or 5 kHz; the substitution method was used, wherein a known noise source at the input or output is compared to the device noise. This method was particularly useful in the white-noise region, i.e., above 10 kHz.

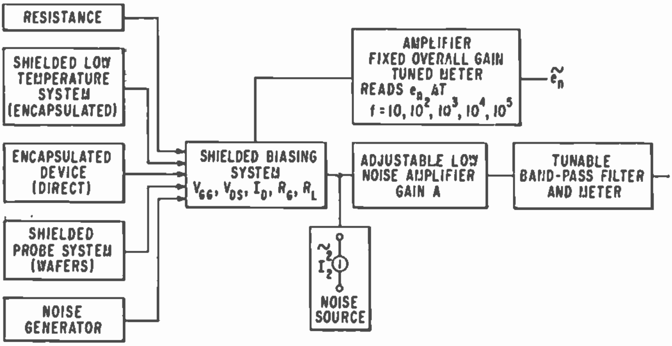

Fig. 2—Low-frequency noise test setup.

5. Experimental Results

The object of the investigation was outlined in the introduction. The main test vehicles were various versions of RCA COS/MOS devices, specifically the CD4000 series.* The versions tested included high-, medium-, and low-threshold devices (> 2.0 V, 1.0 V, and < 0.5 V, respectively), metal-gate and silicon-gate devices, bulk silicon and SOS devices, MOSFET's with SiO_2 and with Al_2O_3 gate dielectrics, and devices with different dielectric thickness. For comparative purposes, other MOSFET's and JFET's were evaluated, with ultra-low-noise JFET's measured alongside the test MOSFET's. We shall summarize here the important observations and draw some conclusions.

5.1 Uniformity of Results

Excellent uniformity was observed on the COS/MOS devices, with variations of V_T and $\tilde{e}_n$ limited to less than 15% in low-threshold bulk devices available commercially. Our laboratory-fabricated devices achieved good uniformity, particularly when we utilized clean, low-temperature processing.[20] Variations in measurements on early SOS devices exceeded 50%, improving to 25% in more recent devices. In contrast to the high uniformity in MOSFET's, high variations of basic parameters and $1/f$ noise were observed in low- and ultra-low-noise JFET's. Standard deviation σ in I_{DSS} and $\tilde{e}_n$ exceeded 50% for the few samples tested, which may have come from different batches. One should remember that these ultra-low-noise JFET's are planar, with buried junctions and very large width ($W > 500$ mils). Hence, non-uniformities in channel length, width, and depth and in the quality of the epitaxial material are likely to occur, and would account for non-uniformity in noise performance. This consideration is important in deciding which devices to use in LSI.

5.2 Bias Dependence

For MOSFET devices operated in saturation, the $1/f$ noise voltage was essentially independent of drain voltage, V_{DS}. It also was a weak function of drain current I_D and, unlike white noise, increased with current.† This is shown in Fig. 3a, and contrasts with results for JFET's

---

* In particular RCA's CD4007 IC was extensively used for testing. For details see *COS/MOS Integrated Circuit Manual* CMS-270 published by RCA's Solid State Division, Somerville, N. J.

† $\tilde{e}_n \sim I_D^{1/4}$ according to Klaassen (Eq. [5]), and $e_n \sim (\ln I_D)^{1/2}$ according to North (Eq. [6]), for ideal square-law devices.

(Fig. 3b). Measurements of the variation of spectral density $\tilde{e}_n^2$ with effective gate voltage V_{GT} showed a linear relation (Fig. 4). In low-noise MOSFET's and SIGFET's, $\tilde{e}_n^2$ was almost invarient with V_{GT}. The variation of $\tilde{e}_n$ with I_D was consistently small, less than the one predicted by Klaassen[8] but more than predicted by North;[16] a comparison of MOSFET's including SOS devices, is given in Fig. 5.

The very weak dependence of $\tilde{e}_n$ on I_D for saturated devices is an asset in the design of amplifiers. The geometry chosen has much more

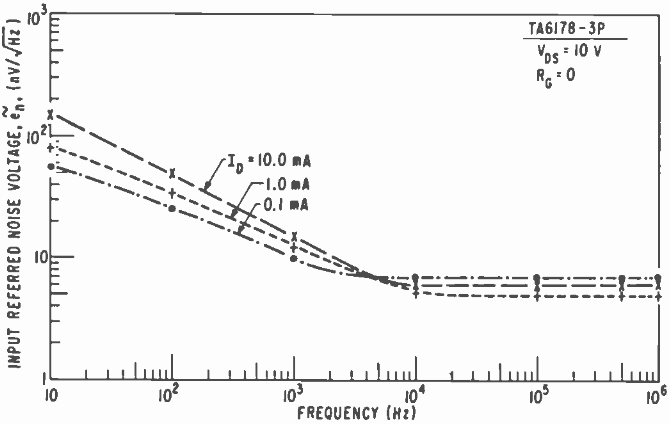

(a)

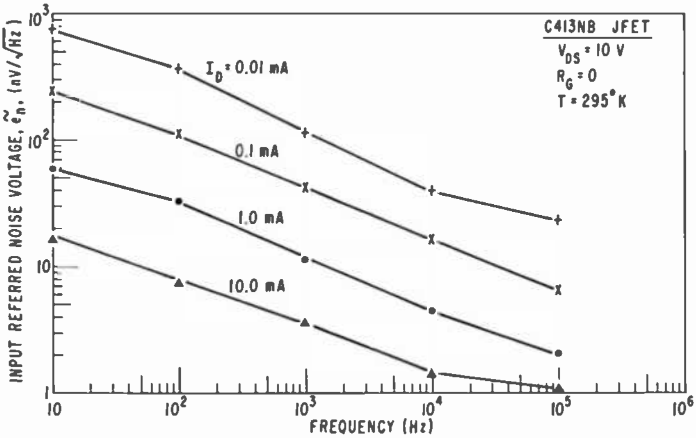

(b)

Fig. 3—(a) Dependence of low-frequency noise voltage on bias (TA6178 in saturation) and (b) $1/f$ noise voltage in JFET versus bias (room temperature, current saturation).

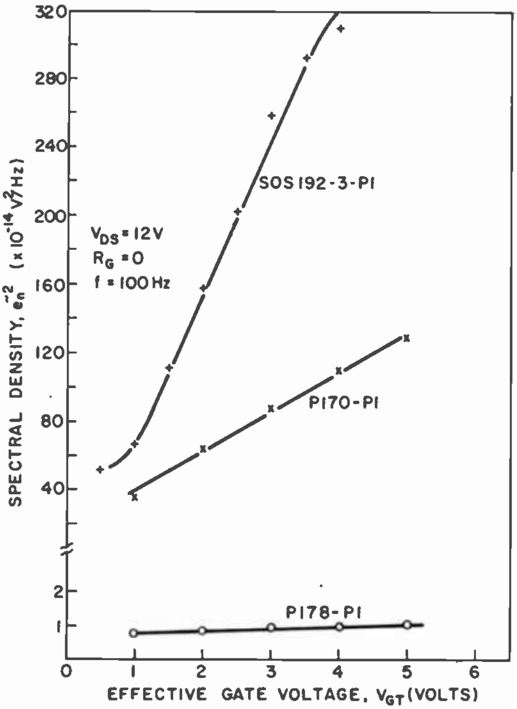

Fig. 4—Variations of noise spectral density with effective gate voltage.

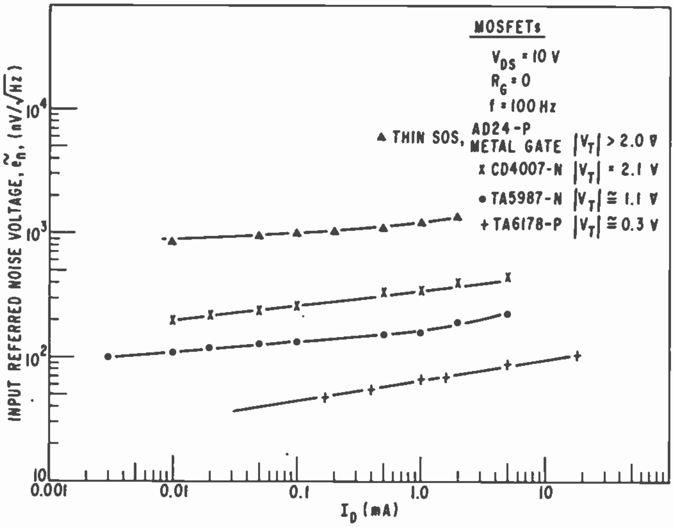

Fig. 5—Variation of 1/*f* noise voltage with current in MOSFET's in saturation.

effect on the noise than any bias variations, particularly in low-noise devices.

It is important to note that saturation of $\tilde{e}_n$ is observed in SOS devices despite the existence of the kink, i.e., an abrupt change in drain current to a higher value at low drain voltage, followed by a second saturation at high gate voltages. The kink phenomenon is discussed elsewhere;[20,25,39] it does not result in a large increase in noise. However, a considerable increase in $1/f$ noise, corresponding to an increase in drain current, is observed several volts below the drain junction breakdown voltage. Such increases may be the result of impact ionization effects appearing as early avalanche.

5.3 Dependence on Silicon Resistivity

We did not test dependence on silicon resistivity over the entire nondegenerate attainable resistivity range. Several authors (e.g., Ref. [22] and [23]) have discussed some dependence of noise on substrate doping, particularly with high-conductivity wafers. More recent papers[7,24] show that such effects are negligible within the entire range of bulk resistivities used in MOS fabrication. Indeed, with high-quality [100] oriented silicon, high-quality clean oxides and interfaces, and low-temperature processing, a comparable and uniformly low noise has been obtained in devices and in wafers ranging in resistivity from 0.4 to 10 ohm-cm. Similar results were observed in SOS p-MOSFET's fabricated in 1-μm films, ranging in resistivity from 0.5 to 6 ohm-cm.

5.4 Area Dependence

Our experimental results bear out the theory, i.e., $\tilde{e}_n \sim (WL)^{-1/2}$. Once a decision is made as to the desired gain–bandwidth product, and L is chosen, the value of W determines e_n. Of course, arbitrarily large W will result in very small input-referred noise voltage, but this is of little use as a practical integrable low-capacitance device. No *excess* of $1/f$ noise was observed in SOS devices when changing from large to small W, indicating that mesa edges did not act as an extra $1/f$ noise source.

5.5 Oxide Thickness Dependence

The dependence of $\tilde{e}_n^2$ on oxide thickness appears to be functionally different in Eqs. [4] and [5]; in one case $\tilde{e}_n^2$ is proportional to t_{ox}^2 and in the other to t_{ox}. However, by considering the different assumptions for N_t in Eqs. [4] and [5], one can show the similarity between the expressions.* Our measurements were carried out on bulk and SOS devices in the current-saturation regime. Bulk devices processed identically and with thick oxides ($t_{ox} > 1200$ Å) exhibited $\tilde{e}_n^2 \sim t_{ox}^n$, where $1 < n < 2$, which is not completely in agreement with Klaassen's results;[26] these results, however, are inconclusive. Recent measurements on bulk devices with $600 < t_{ox} < 1200$ Å, bear out the square relation theory (Eq. [4]) when the devices are operated in saturation at identical effective gate voltages V_{GT}. In some MOSFET's, particularly SOS devices, reducing t_{ox} much below 1000 Å results in a large drop in noise voltage $\tilde{e}_n$—much greater than the expected relationships, $\tilde{e}_n \sim t_{ox}$ or $\tilde{e}_n \sim t_{ox}^{1/2}$, previously discussed. Oxide thickness alone does not account for such large noise reduction. These variations are attributed to changes in surface state and trap densities that result from the changes in oxide thickness, and are discussed subsequently.

5.6 N_{ss} Processing Dependence

Since processing and the corresponding surface properties are not unique, the dependence of e_n on the surface properties is not always known. It constitutes a complex subject that has been discussed by most authors for MOSFET's operated in heavy and uniform inversion, i.e., in the ohmic region. This dependence takes a more complex and yet unknown form for devices operated in saturation. The location of traps in the oxide, their energy distribution, and their relation to the fast surface states are not precisely known, nor is their dependence on energy, i.e., gate voltage and temperature. Also N_{ss} may not always be independent of t_{ox} for thin oxides, particularly in SOS MOSFET's.

To shed some light on the effect of processing on N_{ss} and e_n in saturated MOSFET's, we measured these quantities independently. Methods such as variation of C-V and V_T with temperature, or even charge pumping,[28] are not sensitive or accurate enough to yield N_{ss} when it is much below 10^{11} eV^{-1}cm^{-2}, as is the case with our low-noise devices. The conductance voltage method (G-V), on the other hand, is sensitive enough, and it was utilized[29] on bulk MOS capacitors that were fabricated with the same processing steps as the active devices.

---

* With $N_t = \bar{\gamma} N$ and $C_g \sim Q/V_{GS}$, we can rewrite Eq. [5]

$$e_n^2 \sim \frac{N_t}{qN}\frac{q^2 V_{GS}}{C_g f} = \frac{q}{C_g f} N_t \frac{1}{Q/V_{GS}} \sim \left(\frac{q}{C_g}\right)^2 \frac{N_t}{f}.$$

In Eq. [6], $V_T \sim t_{ox}$

The surface trapping efficiency $\bar{\gamma}$ was evaluated (See Eq. [5] and Fig. 4), and a correspondence between $\tilde{e}_n$, N_{ss}, and $\bar{\gamma}$ was established. Table 1 shows the general trends and a range of variation for such correspondence. The differences in processing consisted of changing t_{ox} in the range 760-1160 Å and changing the annealing methods following clean steam oxidation. From the linear relationship of $\tilde{e}_n^2$ versus V_{GT}, a uniform trap distribution is assumed, making comparison of N_{ss}, $\bar{\gamma}$, and $\tilde{e}_n^2$ valid. The values for $\tilde{e}_n$ were normalized for $t_{ox} = 1000$ Å.

Table 1—Variations of $\tilde{e}_n$ with N_{ss} and $\bar{\gamma}$

N_{ss} ($\mathrm{eV}^{-1}\,\mathrm{cm}^{-2}$)	$\bar{\gamma}$	$\tilde{e}_n^2$ (V^2/Hz)
2.0 — 2.3 ($\times 10^{10}$)	0.17 ($\times 10^{-8}$)	1.0 — 1.2 ($\times 10^{-15}$)
9.5 — 11.0 ($\times 10^{10}$)	0.90 ($\times 10^{-8}$)	5.3 — 5.75 ($\times 10^{-15}$)
46 — 56 ($\times 10^{10}$)	4.40 ($\times 10^{-8}$)	27.8 — 29.0 ($\times 10^{-15}$)

Series resistance poses a severe problem for *C-V*, *G-V*, and charge pumping measurements on SOS films. However, early *G-V* tests* carried out on a 2.2 μm 1 ohm-cm SOS film at low frequency indicated a somewhat higher N_{ss} value than that of identically processed bulk units, ranging from 3×10^{10} to 5×10^{12} $\mathrm{eV}^{-1}\mathrm{cm}^{-2}$.

High uniformity and low-noise performance was obtained in wafers that underwent clean steam oxidation and He anneal *in situ* ($T < 1000°\mathrm{C}$), and an additional H_2 low-temperature annealing. The devices utilized clean aluminum metallization alloyed at the contacts. Similar results were obtained in SIGFET's.

5.7 Dielectric Constant Dependence

Bulk and SOS MOSFET's with Al_2O_3 gate dielectric were fabricated as part of the COS/MOS series. Despite the higher dielectric constant of Al_2O_3 (~9.0) compared with that of SiO_2 (3.8), noise performance of similar devices was comparable. The lack of improvement in noise performance may be due to the higher surface-state density N_{ss} that has been observed in Al_2O_3 capacitors, particularly near mid-gap.[21] To utilize the advantages of a high-dielectric-constant gate insulator, one must maintain the good interface and oxide qualities obtained with SiO_2.

---

* Experiment with J. Carnes of RCA Laboratories (1970—71).

5.8 Dependence on Signal Source Impedance

As expected, dependence on signal source impedance was negligible for the MOSFET's tested (frequency range 10 to 10^5 Hz and source resistance range of 0 to 10^6 ohms). Naturally, the thermal noise of the resistance showed up as an additional noise component in $\tilde{e}$ (RMS addition), but it did not affect the inherent noise generation in the channel. It appears that the effect of source resistance becomes significant when the time constant $[RC]^{-1}$ reaches the value of the operating frequency f. The capacitance C is the total input capacitance of the device. A detailed analysis for source-resistance effects on total noise performance for devices with different gain–bandwidth products is given by Das.[27]

5.9 Dependence on Temperature

The MOSFET's and various other FET's were examined at room temperature (295°K) and at 195°K and 77°K. The devices performed well throughout this temperature range and, in fact, showed some increase in transconductance with decreasing temperatures for identical current level. The *I-V* characteristics for a MOSFET and a JFET at these temperatures are shown in Fig. 6. The measured effective hole mobility of the low-noise bulk SIGFET was 268, 508, and 1480 cm^2/Vsec at $T = 295°$, 195°, and 77°K, respectively. Despite such large variations, the change in e_n was negligible, as expected from theory, with changes in the low-noise JFET being slightly higher, but still small. These noise results are shown in Fig. 7. Clearly, changes in $\tilde{e}_n$ were small for both n and p low-noise MOSFETs and did not follow a specific pattern for either type (in some disagreement with earlier literature.[17-19]). The largest fractional variations in $\tilde{e}_n$ occurred in older bulk and SOS devices, and the smallest variations were observed in recently manufactured low-threshold p-SIGFET's, which also exhibited the highest uniformity and consistency of results. Consequently, we did not further investigate a wide range of devices for details of variations in N_{ss} with temperature, except to verify identical behavior of $\tilde{e}_n^2$ versus V_{GT}, as shown in Fig. 4, thus indicating no changes in effective N_t and uniform distribution of traps even at low temperatures. The same conclusion is drawn from the fact that $\tilde{e}_n^2 \sim 1/f^\alpha$ with $\alpha \cong 1$ at all temperatures.

The experimental data presented here verify the usefulness of MOSFET's as small-signal, high-impedance, low-noise integrable amplifiers and as building blocks in systems where such properties are essential.

6. Specific Observations in SOS MOSFET's

Since sapphire is an excellent insulator that has good mechanical and thermal properties, and since SOS MOSFET's enjoy high inter-device isolation, low inherent and parasitic capacitance, and high packing density, complete integration of systems appears attractive.[30-33] Specifically, detector arrays and sensors or various high-impedance sources can be placed on the same substrate in close proximity to their amplifiers and operated over a wide range of temperatures.

We shall address ourselves only to the aspects of $1/f$ noise that differ in SOS MOSFET's and bulk MOSFET's:

[a] Low-frequency noise of $1/f$ type is observed in SOS MOSFET's, normally below $f = 1$ MHz. Fig. 8 shows noise data on two

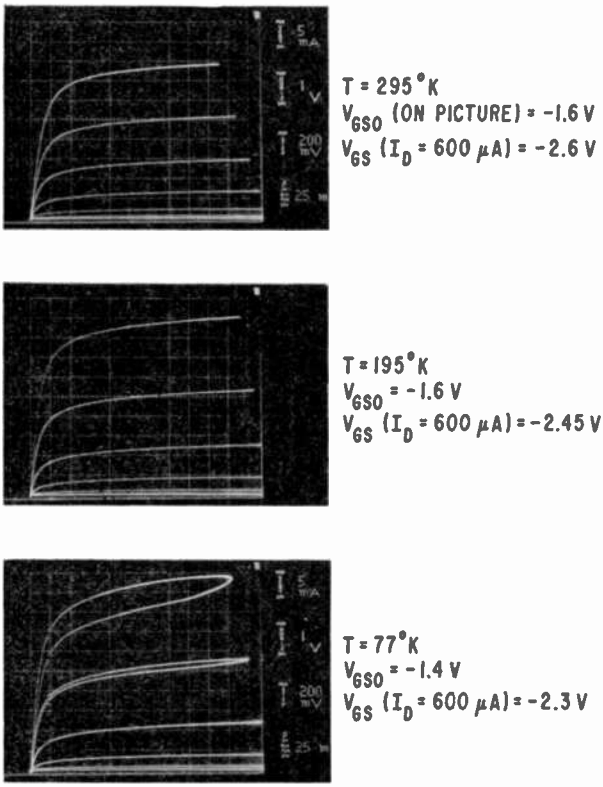

Fig. 6(a)—*I*-*V* characterstics of TA6178-3 MOSFET.

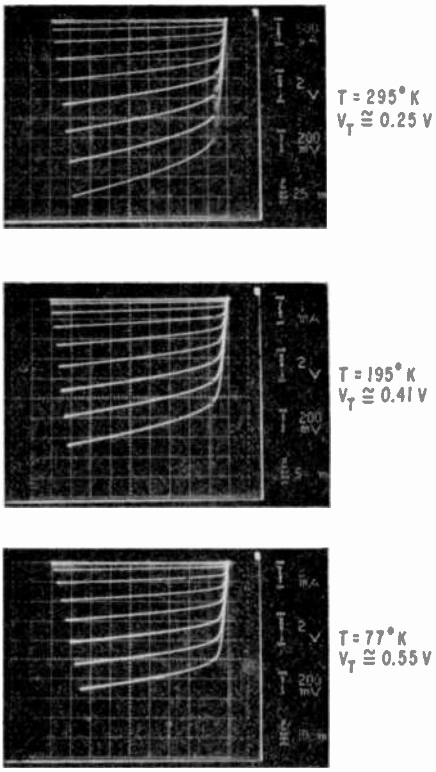

Fig. 6(b)—*I-V* characteristics of C413N JFET.

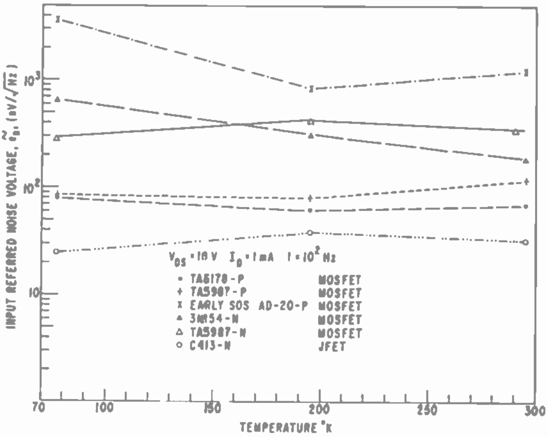

Fig. 7—Variations of 1/*f* noise voltage $\tilde{e}_n$ with temperature for various n- and p-type FET's.

groups of devices at two different drain currents. Slight nonuniformities in the curve are observed below $f = 1$ kHz, especially at low currents, and are discussed subsequently.

[b] $1/f$ noise in SOS MOSFET's is, in general, higher than that observed in bulk devices of identical geometry. This was particularly true in early devices that had been fabricated in thin films, $t_{Si} < 1$ μm.

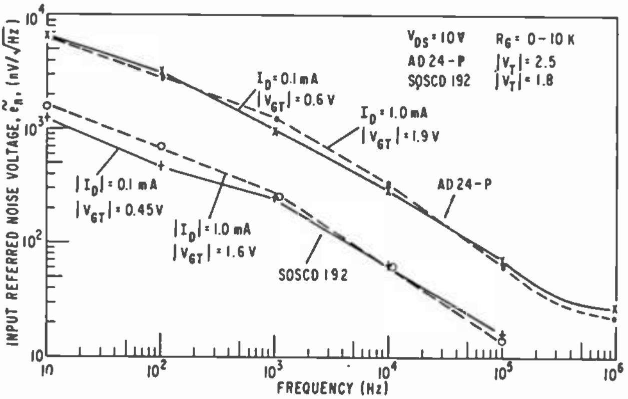

Fig. 8—Low-frequency noise voltage in SOS MOSFET's.

[c] Higher fast-surface-state density N_{ss} cannot by itself account for the higher $1/f$ noise, particularly in thin films. In the past, several G-V measurements on SOS capacitors ($1.2 < t_{Si} < 3.0$ μm) gave values of $5 \times 10^{10} < N_{ss} < 5 \times 10^{11}$/eVcm^2 for $t_{ox} < 1200$ Å as compared to $2 \times 10^{10} < N_{ss} < 10^{11}$/eVcm^2 for identically processed 1 ohm-cm p-type capacitors. Contributions to the low-frequency noise arise from defects in the films (G-R noise associated with deep traps[35-37]) and a somewhat poorer oxide and Si-SiO$_2$ interface. The bottom (silicon-sapphire) interface may also contribute to the noise.

[d] As expected, gate-area dependence of $1/f$ noise in SOS MOSFET's is identical to that of bulk devices.

[e] Bias dependence in SOS MOSFET's showed differences with respect to identical bulk devices. Although the $1/f$ noise generally saturated with current, peaks and bumps were observed in $\tilde{e}_n$ versus V_{DS} for a constant gate voltage V_{GT}. This can be seen in Fig. 9, and is also observed in Fig. 4 at different gate voltages

V_{GT}. Apparently, the distribution and occupancy of traps in the oxide are not uniform, and are excited by specific energies applied to the channel. A slight kink is observed in the *I-V* characteristics of SOS MOSFET's[38,39] particularly in thin n-type devices; this phenomenon is attributed to a parasitic FET effect at the Si–sapphire interface.[34,25] However no abrupt increase in low-frequency noise accompanies this kink, ruling out local or total premature avalanche (Fig. 9). The nonuniformities that are observed in the noise behavior with energy may arise from

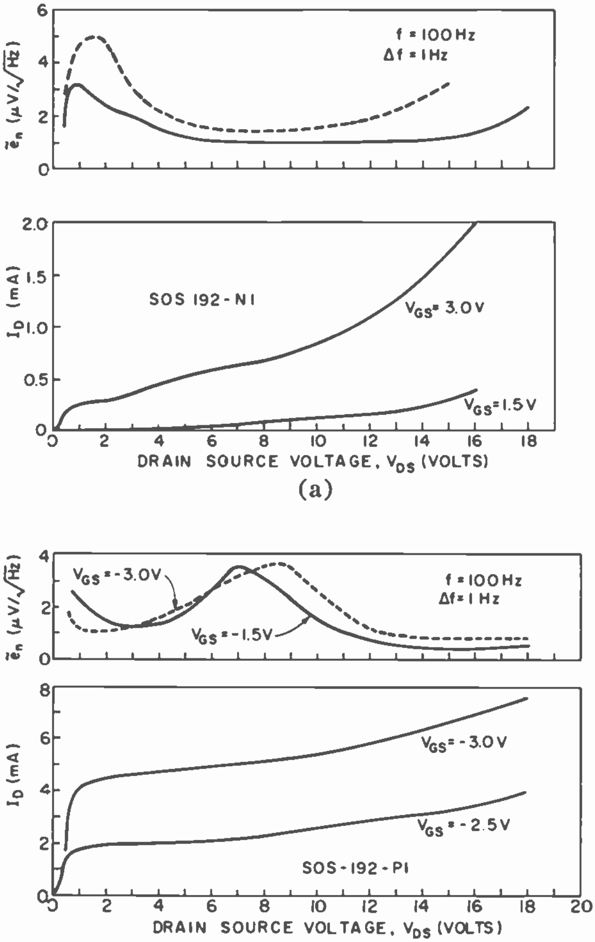

(a)

(b)

Fig. 9—Comparison of noise voltage and drain current as functions of drain voltage: (a) n-MOSFET; (b) p-MOSFET.

several effects—trapping in the oxide, defects in the films (*G-R* noise), and interaction of carriers with the bottom interface. The nonuniform bias dependence is very pronounced in thin films ($t_{Si} < 1.0\ \mu m$) and slight in thick films ($t_{Si} > 2.0\ \mu m$) with shallow drain–source regions, suggesting that film defects and interaction with the lower interface may indeed contribute heavily to the noise.

[f] The oxide thickness dependence in SOS MOSFET's is greater than expected from either Eqs. [4] or [5] for oxides less than 1200 Å in thickness. With identical He and H_2 annealing procedures and clean steam oxidation,[20,41] the large drop in $\tilde{e}_n$ with a decrease in t_{ox} suggests that t_{ox} and N_{ss} may not be independent variables, and that the product $P_{ss} = N_{ss}t_{ox}$ decreases rapidly as t_{ox} is decreased. Although different annealing techniques may prove to reduce the dependence of $\tilde{e}_n$ on t_{ox}, it is believed that overall dependence of N_t or the noise mechanism on t_{ox} exists, especially in thin-film devices.

[g] The dependence of $\tilde{e}_n$ on the film thickness t_{Si} was very pronounced below $t_{Si} = 1\ \mu m$. Since it is known that the quality of the film and associated electrical properties fall sharply with film thickness,[34,36,39,40] oxide and interface properties are also expected to deteriorate. Fig. 10 shows the total effect on $1/f$ noise of changes in t_{Si} and t_{ox}, suggesting that $t_{Si} > 1.2\ \mu m$ should be maintained. Our best results, approaching those of commercially available COS/MOS bulk devices ($|V_T| = 2.0$ V), were obtained on 2.4-μm n-type films with $t_{SiO_2} < 1000$ Å, and our clean oxide growth and annealing techniques.

[h] Low-temperature noise performance of SOS devices is similar to that of bulk devices in its trends. P-MOSFET's, however, become somewhat quieter at low temperatures, a trend that continues below $T = 195°K$; low-temperature investigation of $1/f$ noise, particularly below 77°K, may shed more light on the distribution function and occupation index of states in SOS MOSFET's operated in saturation. As with other measurements, the best uniformity was obtained on thick p-MOSFET's, and the greatest nonuniformity of results (with temperature) on thin n-MOSFET's.

[i] The nonuniformity of the various results was a function of many variables. It was in general much greater than that obtained on identical bulk devices, particularly our early devices. The largest standard deviation in results was observed on very thin films

($t_{Si} \leqslant 0.6\mu m$), across large wafers ($D > 1.25$ inches), on devices with thick oxides ($t_{ox} > 1200$ Å), and on devices that did not undergo He and H_2 anneal. Conversely, the best uniformity was obtained on thick-film, thin-oxide, properly annealed MOSFET's. One may conclude, therefore, that the quality of the film affects noise performance as well as the uniformity, and that the distance of the channel from the bottom interface may also play a role.

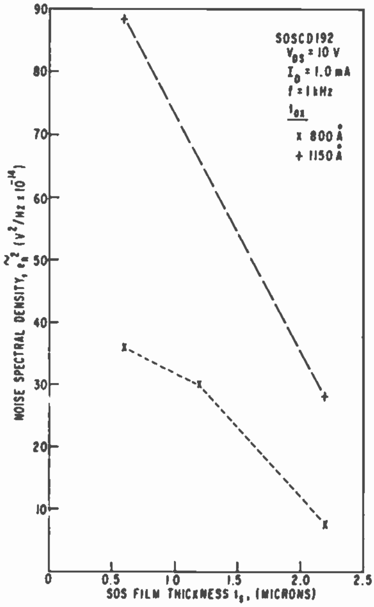

Fig. 10—Variations of noise spectral density in SOS MOSFET's with thickness of silicon film and thickness of oxide.

We can summarize the results for SOS MOSFET's by suggesting the use of thicker films, thinner oxides, and shallower source–drain regions, subject to gain and yield requirements. Use of p-MOSFET's offers slightly better uniformity, lower noise, and better low-temperature performance. Low-stress processing combined with proper annealing can result in SOS MOSFET's achieving noise performance and uniformity approaching that of good quality bulk devices.

7. Conclusion—Applications of MOSFET's in Low-Noise Systems

Measurements made included the comparison of noise performance in a variety of MOSFET's and JFET's at room temperature. Results are shown in Fig. 11. The lowest noise was observed in one of the JFET samples. Of all the transistors tested, it had the largest chip area, largest periphery ($W > 17000$ μm), highest input capacitance (> 50 pF), and a finite nontrivial input conductance. The uniformity of the performance among the several JFET samples under test was poor. We also note that large-gate-area MOSFET's ($W \cong 12000$ μm) exhibit low $1/f$ noise and, in fact, very low noise above 5 kHz. Our recent p and n MOSFET's ($W \cong 1600$ and 200 μm, respectively, and $L \cong 6.5$ μm) consistently exhibited good noise performance and good uniformity, even from wafer to wafer. Their small size, very high input resistance, low input capacitance, and ease of integration make them very attractive for specific applications.

As an example of the application of these considerations, we will consider the following case. A signal-source I_s with a noise component $\bar{i}_{ns}$ has a low output capacitance ($C_s = 2.0$ pF) and a high output resistance ($R_s > 10^{12}$ ohms). The thermal noise of the output resistance is $\bar{i}_{n2} = (4kT/R_s)^{1/2}$. To this source an amplifier is connected, with overall input resistance R_i (including biasing network) that develops a thermal noise $\bar{i}_i$. The amplifier also has input capacitance C_i and an input-referred noise voltage $\tilde{e}_n$ (See Fig. 12 (a)). We want to determine the amplifier that gives the desired gain, and the least amount of noise. We assume a high-quality low-level signal source with the following parameters:

$$C_s = 2.0 \text{ pF} \qquad I_s \cong 10^{-9} \text{ A}$$

$$R_s > 10^{12} \text{ ohms} \qquad \bar{i}_{ns} = 5 \times 10^{-14} \text{ A}/\sqrt{\text{Hz}}$$

$$\Delta f \equiv f_u - f_l \cong f_u = 2 \text{ kHz}.$$

where f_u and f_l are the upper and lower frequency limits, respectively. Using the above numbers, we obtain

$$I_{ns} = \left[\int_0^{f_u} \bar{i}_{ns}\, df\right]^{1/2} = [\bar{i}_{ns}{}^2 f_u]^{1/2} = 2.2 \times 10^{-12} \text{ A}. \tag{8}$$

At the source, the signal-to-noise ratio is

$$\text{SNR} = 20 \log (I_s/I_{ns}) = 20 \log [10^{-9}/(2.2 \times 10^{-12})] \cong 50 \text{ dB}. \tag{9}$$

Our goal is to maintain this respectable SNR at the amplifier output. With $R_s > 10^{12}$ ohms, $\bar{i}_{n2} < (4kT/R_s)^{1/2} = 10^{-16}$ A/$\sqrt{\text{Hz}} \ll \bar{i}_{ns}$; we can

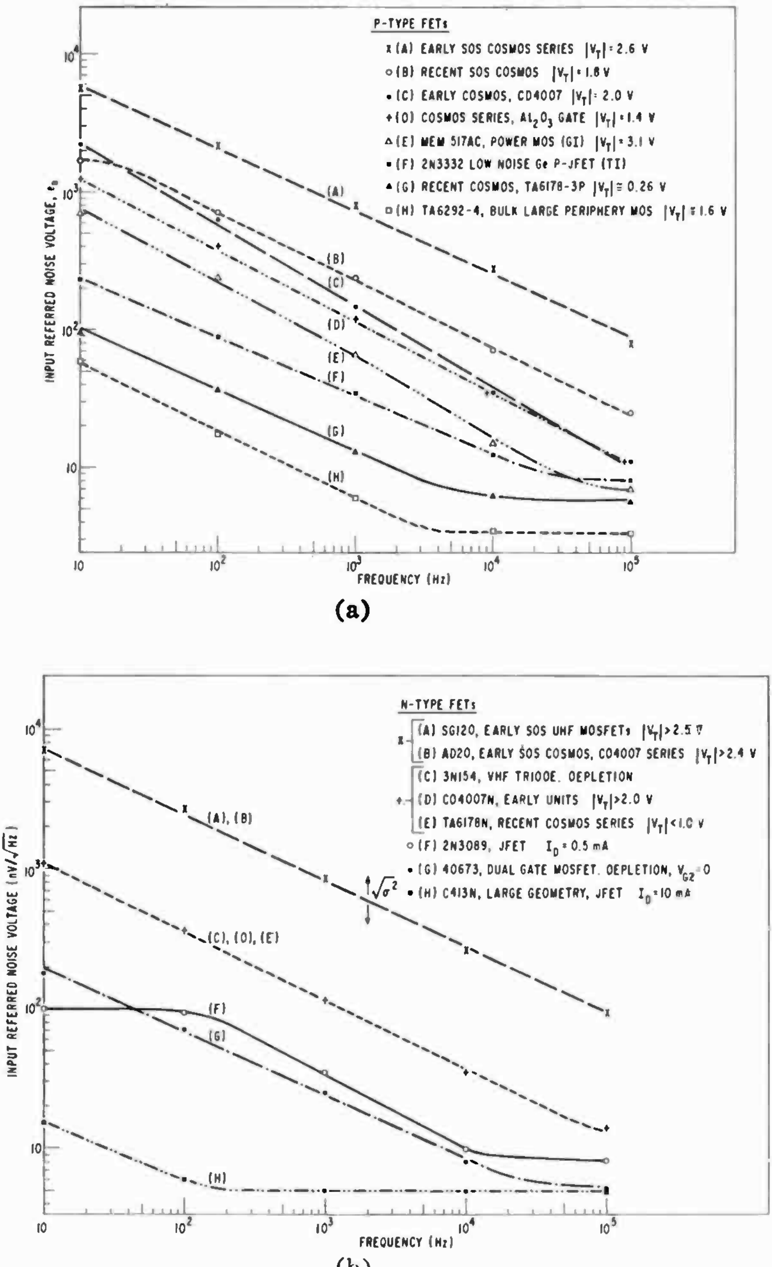

(a)

(b)

Fig. 11—Low-frequency noise (a) in various p-type FET's and MOSFET's in saturation and (b) in various n-type JFETs and MOSFETs in saturation.

therefore ignore $\bar{i}_{n2}$. Also, a load resistance that will cause a 3-dB drop in SNR is

$$R > (4kT/\bar{i}_{ns}^2) = 1.6 \times 10^{-20}/(25 \times 10^{-28}) = 6.4 \text{ megohms} \quad [10]$$

This value immediately rules out any bipolar transistor. In fact, for best matching, one would prefer an amplifier whose input is purely capacitive, with $R_i \rightarrow \infty$; however, $R_i > 6.4$ megohms is sufficient to maintain a high SNR. Looking at the amplifier input, we can convert $\tilde{e}_n$ into a parallel current source $\bar{i}_{ni}$ (Fig. 12(b)) by a Norton transformation $\bar{i}_{ni}^2 = \tilde{e}_n^2 |Y|^2$, where Y is the appropriate admittance. Hence, the total noise-current spectral density at the gate is

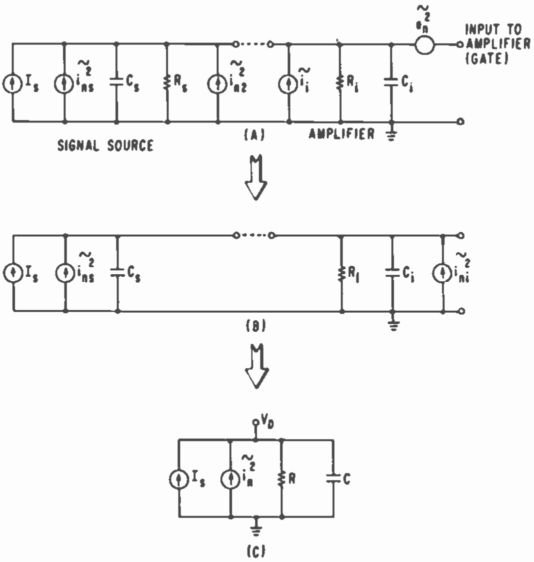

Fig. 12—Small signal and noise equivalents: (a) signal source and amplifier, (b) a simplified circuit, and (c) overall equivalent circuit.

$$\bar{i}_n^2 = \bar{i}_{ns} + \bar{i}_i^2 + e_n^2 |Y|^2 = \bar{i}_{ns}^2 + \frac{4RT}{R_i} + \bar{\gamma} \frac{qV_{GT}}{C_i f} \left[\frac{1}{R_1^2} + (WC) \right]^2 \quad [11]$$

where $C_i = C_g$, $C = C_s + C_i$, and e_n^2 is defined by Eq. [6].

To minimize the noise we note two conditions: (1) $R_i \rightarrow \infty$, but from Eq. [1], $R_i \gg 6.4$ megohms will eliminate the i_i^2 term; (2) $C_s = C_i$ minimizes the equation with respect to C. These two conditions restate the requirement that the amplifier have a purely capacitive input, with $C_i = C_s$. Assume that $C_i = C_s$ and $\bar{i}_n \neq f(\omega)$ and calculate the quantities of interest:

$$I_n^2 = \int_0^{f_u} \bar{i}_n^2 \, df = \int_0^{f_u} \left[\bar{i}_n^2 + \overline{\gamma} \frac{qV_{GT}}{C_i f} (4\pi C_i f)^2 \right] df. \qquad [12]$$

Performing the integration, we obtain

$$\tilde{I}_n^2 = I_{ns}^2 \left[1 + \frac{\tilde{e}_n^2 \, (f_u)}{\bar{i}_n^2 / 2(\omega_u C_i)^2} \right] \equiv I_{ns}^2 \, [1 + \beta]. \qquad [13]$$

Ideally, $\beta = 0$ and the system SNR is unchanged. $\beta = 1$ produces a 3-dB drop in SNR. With the previously given parameters and $e_n \cong 50$ nV/Hz; $f_u = 4000$ Hz, we obtain

$$I_n^2 = I_{ns}^2 \, [1 + 0.01]. \qquad [14]$$

This analysis suggests that the additional noise in this system is negligible. The simplified equivalent circuit is shown in Fig. 12(c). With $R \cong 2 \times 10^7$ ohms, the total noise voltage at the input is $E_{ns} = I_{ns} R = 0.5 \mu$V. A quieter source used with the same device will result in a higher β; e.g., with $E_x = 50$ nV, the deterioration is approximately 3 dB. We can take the analysis further to include considerations of impedance matching and flat response with Δf. Such an analysis is simple but not within the scope of this paper. From the requirements of specific $\tilde{e}_n$ and C_i to minimize SNR, the restrictions of impedance matching, and the gain–bandwidth specifications, one can proceed to choose the geometry of the MOSFET. Subject to the minimum product $N_{ss} t_{ox}$ obtainable in processing, it is possible to design a MOSFET amplifier for low-noise high-impedance systems. Specific guidelines are offered by various authors, e.g., Das.[27]

The foregoing analysis suggests that MOSFET's similar to the bulk silicon variety can be designed to meet specific gain and SNR requirements in complex LSI arrays, and to exhibit high uniformity and yield that surpass any performance offered heretofore by JFET's or bipolars. Furthermore, improvement in SOS devices can make it possible to place total systems (sources and amplifiers) on a chip, and to operate them under varying temperature and bias conditions.

Acknowledgment

The author is grateful to D. O. North and A. Rose for many interesting discussions. The support of C. W. Mueller and G. L. Schnable are appreciated. SOS films were supplied by Y. S. Chiang and P. A. Crossley, and some SOS devices were fabricated by C. F. Arasim and D. W. Flatley. S. T. Hsu supplied interesting comments and reviewed the manuscript.

References:

[1] A. Van der Ziel, "Noise in Solid State Devices and Lasers," **Proc. IEEE,** Vol. 58, p. 1178, Aug. 1970. This is a general condensed discussion of noise in devices and includes an extensive list of references.

[2] W. H. Fonger, "A Determination of 1/f Noise Sources in Semiconductor Diodes and Transistors," **Transistors I,** RCA Laboratories, Princeton, N.J., 1956, p. 239.

[3] A. L. McWhorter, **1/f Noise and Related Surface Effects in Germanium,** MIT Lincoln Laboratory, Lexington, Mass., Report No. 80, May 1955.

[4] General theory of the various noise sources in MOSFET's has been derived by A. G. Jordan and N. A. Jordan in, "Theory of Noise In Metal Oxide Semiconductor Devices," **IEEE Trans. Electron Devices,** Vol. ED–12, p. 148, March, 1965. It can also be found in Ref. [12].

[5] S. Christenson, I. Lundstrom, and C. Svenson, "Low Frequency Noise in MOS Transistors, I. Theory," **Solid-State Electronics,** Vol. 11, p. 797, Sept. 1968.

[6] E. A. Leventhal, "Derivation of 1/f Noise in Silicon Inversion Layers From Carrier Motion in Surface Band, "**Solid-State Electronics,** Vol. 11, p. 979, Aug. 1968.

[7] S. T. Hsu, "Surface State Related 1/f Noise in MOS Transistors," **Solid-State Electronics,** Vol. 13, p. 1451, Aug. 1970.

[8] F. M. Klaassen, "Characterization of 1/f Noise in MOS Transistors," **IEEE Trans. Electron Devices,** Vol. ED–18, p. 887, Oct. 1971.

[9] H. S. Fu and C. T. Sah, "Theory and Experiments on Surface 1/f Noise," **IEEE Trans. Electron Devices,** Vol. ED–19, p. 273, Feb. 1972.

[10] R. J. Hawkins and G. G. Bloodworth, "Two Components of 1/f Noise in MOS Transistors," **Solid-State Electronics,** Vol. 14, p. 929, 1971.

[11] I. R. Mansour, et al, "Measurement of Current Noise Spectrum in MOS Transistors," **Radio Electron. Eng.,** Vol. 35, p. 212, April 1968.

[12] A. Van der Ziel, **Noise: Source, Characterization, Measurements,** Prentice-Hall, Englewood Cliffs, N.J., (1970).

[13] F. P. Heiman and G. Warfield, "The Effects of Oxide Traps on the MOS Capacitance," **IEEE Trans. Electron Devices,** Vol. ED–12, p. 167 (1965).

[14] A. Rose, RCA Laboratories, private communication.

[15] A. Rose, "An Analysis of Photoconductive Photon Counting," in **Proc. 3rd Photoconductivity Conf.,** Stanford, p. 7, Aug. 1969.

[16] D. O. North, RCA Laboratories, private communications.

[17] S. Christenson, I. Lundstrom, and C. Svenson, "Low Frequency Noise in MOS Transistor, II. Experiments," **Solid-State Electronics,** Vol. 11, p. 813, Sept. 1968.

[18] C. G. Rogers, "Low Frequency Noise in MOST's at Cryogenic Temperatures," **Solid-State Electronics,** Vol. 11, p. 1099, 1968.

[19] D. A. Elliott, "Low Temperature Noise in MOST Amplifiers," **Solid-State Electronics,** Vol. 14, p. 1042, 1971.

[20] R. S. Ronen, "SOS Circuit Technology," Final Contract Report, Contract No. F36615–71–C–1748, Project #4159, Oct. 1972.

[21] P. Norris and F. Micheletti, RCA Laboratories, private communication.

[22] K. Takagi and A. Van der Ziel, "Non-thermal Noise in MOSFET's and MOS Tetrodes," **Solid-State Electronics,** Vol. 12, p. 907, Nov. 1969.

[23] L. D. Yau and C. T. Sah, "On the 'Excess White Noise' in MOS Transistors," **Solid-State Electronics,** Vol. 12, p. 928, Nov. 1969.

[24] F. M. Klaassen, "High-Frequency Noise of the Junction FET," **IEEE Trans. Electron Devices**, Vol. ED–14, p. 368, July 1967.

[25] R. S. Ronen, to be published.

[26] F. M. Klaassen, "On the Geometrical Dependence of 1/f Noise in MOSFET's," **Phillips Res. Repts**, Vol. 25, p. 171 (1970).

[27] D. M. Das, "FET Noise Sources and Their Effects on Amplifier Performance at Low Frequencies," **IEEE Trans. Electron Devices**, Vol. ED–19, p. 338, March 1972.

[28] F. Leuenberger, "Charge Pumping and Low-Frequency Noise in MOS Structures," **Phys. Stat. Sol. B**, Vol. 8, p. 545 (1971).

[29] R. S. Ronen, J. E. Carnes, unpublished work.

[30] J. F. Allison et al, "Thin Film Silicon: Preparation, Properties and Device Applications," **Proc. IEEE**, Vol. 57, p. 1490 (1969).

[31] C. W. Mueller, "Thin Film Devices on Dielectric Substrates," **J. Vacuum Soc. and Tech.**, Vol. 7, p. 147 (1970).

[32] G. E. Gottlieb, J. F. Corboy, G. W. Cullen, and J. H. Scott, "The Epitaxial Deposition of Silicon on Insulating Substrates for MOS Circuitry," **Met. Trans.**, Vol. 2, p. 653 (1971).

[33] R. S. Ronen and P. Robinson, "Recent Advances in Thin Film Silicon Devices on Insulating Substrates," **Proc. IEEE**, Vol. 59, p. 1506 (1971).

[34] R. S. Ronen, Ph.D. Dissertation, Polytechnic Institute of Brooklyn, 1973.

[35] F. P. Heiman, "Donor Surface States and Bulk Acceptor Traps in Silicon-On-Sapphire Films," **Appl. Phys. Letters**, Vol. 11, p. 132 (1967).

[36] D. J. Dumin and P. H. Robinson, "Electrically and Optically Active Defects in Silicon-on-Sapphire Films," **J. Crystal Growth**, Vol. 3, p. 214 (1968).

[37] D. J. Dumin, "Deep Levels Within the Forbidden Gap of SOS Films," **Solid-State Electronics**, Vol. 13, p. 415 (1970).

[38] E. J. Boleky, private communication.

[39] G. W. Culen, J. F. Corboy, W. W. Claus, "Silicon on Sapphire Transistor Development," Interim Tech. Report, Air Force Avionics Laboratory, Wright-Patterson Air Force Base, Dayton, Ohio, Report #F33615–72–C–1695, Oct. 1972.

[40] D. J. Dumin, "Electrical Properties of Silicon Films Grown Epitaxially on Sapphire," **J. Appl. Phys.**, Vol. 38, p. 1909 (1967).

[41] J. H. Scott and J. R. Burns, "Low Temperature Processing of C/MOS Integrated Circuits on Insulating Substrates," Presentation, Electrochem. Soc. Mtg., Los Angeles. 1970, abstract #139, p. 359.

Equilibrium Properties of Schiff-Base Liquid-Crystal Mixtures

Howard Sorkin and Arthur Denny

RCA Solid State Division, Somerville, N. J.

Abstract—Some liquid-crystal mixtures developed at RCA are described; these materials are mixtures of Schiff bases and are used in display devices. The formation of the Schiff base is discussed. It was discovered that the aldehyde and amine moieties of each Schiff base in a mixture can interchange and lead to the formation of additional Schiff bases, unless either all the aldehyde or all the amine moieties are the same. The interchange takes place through the presence of free aldehyde and amine. This interchange explains the irreproducibility of certain published data, and is of fundamental importance in the establishment of guidelines for formulating liquid-crystal mixtures. Kinetics of the exchange for one system are presented. The rate is low, but increases with increasing water content.

Finally, the equilibrium between p-methoxybenzylidene-p′-n-butylaniline (MBBA) and water is investigated. The equilibrium constant is 5.9 at 30°C. The effect of this equilibrium on display devices is discussed.

1. Introduction

Liquid crystals are organic compounds that exhibit various degrees of long-range intermolecular order in the liquid state. The majority of these materials attain their ordered state immediately upon melting.

Upon further heating, all liquid crystals undergo a transition from their ordered fluid state (mesomorphic state) to the normal disordered state (isotropic state). The temperature at which a material melts and becomes isotropic is a function of its molecular structure. The temperature range between the melting point and the isotropic point is the mesomorphic range of the material.

There are three types of mesomorphism—nematic, smectic, and cholesteric. These terms are descriptive of the nature of the ordering of the molecules. *Nematic* materials may be compared to pencils in a box that is several times as long as the pencils. The pencils lie parallel to one another but are free to slide past each other. A descriptive model for *smectic* materials is similar except that the box would be only as long as the pencils; the boxes would lie end to end and the pencils (molecules) would be confined in layers that could glide over each other. In both cases, nematic and smectic, the molecules can rotate around their axis of alignment. The *cholesteric* state is a special case of the nematic state. Continuing the box and pencil analogy, in the cholesteric state, the boxes are stacked one above the other with each box slightly twisted with respect to the box below to form a helix of definite pitch at a given temperature. Of greatest interest to the electronics industry are the nematic materials. R. Williams[1] and G. Heilmeier et al[2] of RCA Laboratories discovered that the application of an electric field to a thin layer of nematic material confined between transparent, conductive electrodes produces a change in the appearance of the liquid from transparent to opaque. This effect, called the dynamic scattering mode (DSM), is useful to engineers and designers interested in the control of light and in the display of information electronically. Many classes of organic compounds show nematic behavior; the RCA effort was centered mainly on the class of compounds called Schiff bases (structure I).

The nematic materials available at the time of the discovery of DSM exhibited melting points well above room temperature. Goldmacher, Castellano, et al[3] synthesized hundreds of new nematic materials in an effort to develop materials that would be nematic at ambient temperatures. It was not until they started preparing mixtures of different nematic compounds that they were able to obtain nematic materials with extended mesomorphic ranges. A mixture called APAPA-RT was developed that has a reported nematic range of 22° to 108°C; the mixture consists of an equimolar mixture of three Schiff bases. Later, another mixture of three different Schiff bases was prepared; this mixture, called LT liquid crystal, has a nematic range from −22° to 63°C. These two materials, APAPA-RT and LT, became the focus of an intensive study oriented toward processes and techniques for the synthesis, purification, and quality control of the individual materials and their mixtures.

This paper is concerned mainly with some basic chemistry of Schiff base mixtures that was elucidated during this study and is a direct outcome of the work performed to develop quality-control techniques. The main method of analysis used was liquid-liquid chromatography.

2. Schiff-Base Chemistry

The liquid-crystal compounds used in RCA devices are aromatic Schiff bases. They have the structure I. Changes in the substituents, X and Y, result in materials with different nematic temperature ranges. Not all Schiff bases, however, are liquid crystals.

Structure I

Schiff bases are formed by the reaction between an aldehyde and an amine. Water, which is also formed in the reaction, must be removed from the system so that the reverse reaction, hydrolysis, is minimized. The formation of a Schiff base is shown in reaction 1.

Reaction 1

It has long been established that reaction 1 is an equilibrium reaction; i.e., if water is added to a Schiff base, the compound will hydrolyze to give the original aldehyde and amine. For any equilibrium reaction, the following relation holds:

$$K = \frac{\Pi\ [\text{products}]}{\Pi\ [\text{reactants}]} \qquad [1]$$

where the square brackets denote concentrations. K is the equilibrium constant and is constant for a given temperature; the value of K changes with temperature in the following way:

$$\frac{d(\ln K)}{dT} = \frac{\Delta H}{RT^2}, \quad [2]$$

where ΔH is the heat of reaction and R is the gas constant. For the Schiff base reaction

$$K = \frac{[\text{Schiff base}]\,[\text{H}_2\text{O}]}{[\text{Aldehyde}]\,[\text{Amine}]}. \quad [3]$$

A Schiff base will always contain some free aldehyde and free amine; the amount of each depends on the value of K and on the water content. Every Schiff base examined by liquid–liquid chromatography showed the presence of the corresponding aldehyde. However, the amine was only detected in two cases, MBBA and EBBA. The reason for this distribution is not known; it may occur because the amines are fairly polar and so will be retained strongly by the column used. The amine retention time will be long and the peak very broad and of negligible height.

3. Liquid-Crystal Materials

3.1 Characterization

Most of the early work at RCA was based on anisylidene-p-aminophenyl acetate (I, $X{=}CH_3O{-}$, $Y{=}CH_3COO{-}$). For convenience, this and similar materials are called APAPA. This family name is suffixed with a two-digit numeral that defines X and Y. The first digit represents the number of carbon atoms in X; the second digit is two less than the number of carbon atoms in Y. For example, APAPA-12 has the structure II:

Structure II

The APAPA-RT liquid crystal is composed of APAPA 10, 12, and 40.

The LT material is composed of an equimolar mixture of three Schiff-base compounds that do not fit into the APAPA nomenclature but that do have the structure I. These materials are listed in Table 1.

Table 1—Compounds That Do Not Fit APAPA Nomenclature But That Have Structure I

Compound	Code	*X*	*Y*
p-Methoxybenzylidene-p'-n-Butylaniline	MBBA	CH_3O-	$-CH$
p-Ethoxybenzylidene-p'-Butylaniline	EBBA	CH_3CH_2O-	$-CH_2CH_2CH_2CH_3$
p-Methoxybenzylidene-p'-Aminophenyl 3-Methyl-Valerate	MBV	CH_3O-	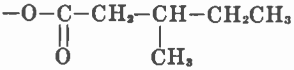 $-O-\underset{\underset{O}{\Vert}}{C}-CH_2-\underset{\underset{CH_3}{\vert}}{CH}-CH_2CH_3$
p-Ethoxybenzylidene-p'-Aminophenyl 3-Methyl-Valerate	EBV	CH_3CH_2O-	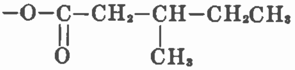 $-O-\underset{\underset{O}{\Vert}}{C}-CH_2-\underset{\underset{CH_3}{\vert}}{CH}-CH_2CH_3$

A third mixture, APAPA-WRT, was also used in later work. This mixture is composed of the same three compounds (A10, A12, and A40) used in the APAPA-RT material but in the following molar proportions: A10, 32.5%; A12, 47.5%; and A40, 20.0%. The APAPA-WRT mixture had a wider transition-temperature range than the APAPA-RT mixture. All of the Schiff-base materials were characterized by liquid–liquid chromatography methods as to their retention times. The corresponding aldehydes were seen and, in the case of MBBA and EBBA, the butyl aniline could also be detected. Retention times of all the materials are listed in Table 2.

3.2 Purity

After the individual liquid-crystal compounds had been characterized, examination of liquid-crystal mixtures was begun to determine the purity of production materials. Various batches of APAPA-RT and APAPA-WRT material were analyzed; all chromagraphs exhibited a major peak (at least several percent) that is not present in the chromatographs of any of the individual APAPA compounds used to prepare the blend; i.e., four peaks were seen where one would only expect to see three. To explain this unexpected observation, a hypothesis involving dynamic equilibrium between pairs of Schiff base molecules was developed. The hypothesis assumes that the aldehyde moiety of two molecules can interchange. The two Schiff bases are

Table 2—Retention Time of Liquid-Crystal Components

Compound	Retention Time (minutes)
p-Methoxybenzylidene-p′-Butylaniline (MBBA)	6.7
p-Ethoxybenzylidene-p′-Butylaniline (EBBA)	6.7
Butylaniline (BA)	7.0
Butoxybenzaldehyde	7.4
Ethoxy Valerate (EBV)	7.6
APAPA 42 (A42)	7.7
Methoxy Valerate (MBV)	8.2
p-Ethoxybenzaldehyde (EBA)	8.3
APAPA 40 (A40)	9.3
APAPA 13 (A13)	9.3
APAPA 12 (A12)	9.9
p-Methoxybenzaldehyde (MBA)	10.0
APAPA 10 (A10)	16.0

Chromatograph Conditions:

Column: β,β′-Oxydipropionitrile (BOP) 1 meter long, 2.1 millimeters ID.
Mobile Phase: Heptane saturated with BOP
Pressure: 150 psi
Temperature: Ambient
Detector: UV Photometer at 254 nanometers

in equilibrium with the aldehyde and amine, as shown in the following two equations:

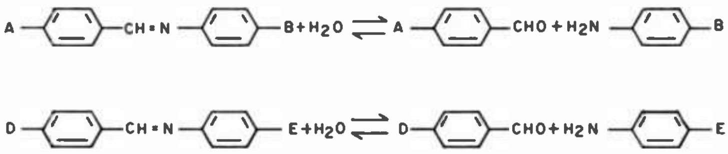

The free aldehydes and amines can recombine in two additional ways:

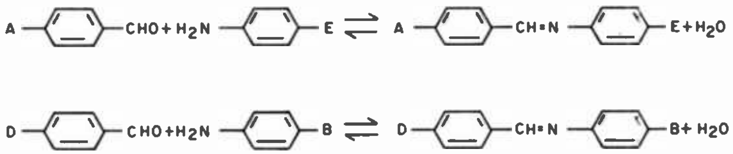

In this way, two new Schiff bases can be formed. Overall, the following equilibrium will be set up:

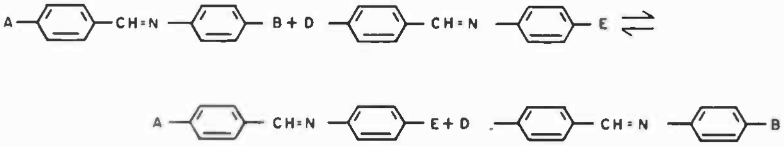

The original binary mixture may change into a four-component mixture; however, if A and D or B and E are the same, then no change can occur. This process can be described, for convenience, by means of the APAPA notations. For the APAPA 10, 12, and 40 systems, one can write;

$$\begin{aligned} &A10 + A12 \leftrightharpoons A10 + A12 \\ &A10 + A40 \leftrightharpoons A10 + A40 \\ &A12 + A40 \leftrightharpoons A10 + A42 \end{aligned}$$

The original ternary system will change to a four-component system. The amount of A42 formed will be governed by the relation

$$K = \frac{[A10]\ [A42]}{[A12]\ [A40]} \qquad [4]$$

but will depend on the original composition of the mixture. Since all the compounds are structurally similar, the value of the equilibrium constant K will probably be approximately unity. The formation of A42 could then explain the appearance of the fourth, unidentified peak in the chromatographs of the APAPA-RT and APAPA-WRT liquid-crystal mixtures.

Of the three possible binary mixtures of A10, A12, and A40, only the A12 and A40 mixtures will cause the formation of additional compounds. This fact was experimentally verified; the results are shown in Table 3. The possibility that the chemical reaction was catalyzed by the chromatographic column or that it only occurred when the APAPA compounds contacted the mobile phase was readily eliminated by the fact that freshly prepared mixtures of A12 and A40 or of A10, A12, and A40 did not show the presence of A42.

These mixtures only showed A42 after an aging period of several days; the amount of A42 in the mixture increased slowly with time. The final proof of the hypothesis concerning the interchange of the aldehyde moiety of two molecules was the independent synthesis of A42 by an unambiguous method. The A42 thus prepared was found to have the same retention time as the peak that developed in the mixtures.

Table 3—Results of Mixing A10, A12, and A40

Mixture	Retention Time of Major Components (minutes)			
	A42	A40	A12	A10
A10+A12			9.9	16.0
A10+A40		9.3		16.0
A12+A40	7.7	9.3	9.9	16.0
A10+A12+A40	7.7	9.3	9.9	16.0

The LT material, which is a mixture of MBBA, EBBA, and MBV, would be expected to yield only two peaks, as MBBA and EBBA have the same retention times. In fact, however, the mixture showed three main peaks. The additional peak was predicted to be the result of the formation of EBV from the reaction between EBBA and MBV. A sample of EBV was synthesized and found to have the same retention time as the unknown peak in the LT mixture. Also, of the three possible binary mixtures of MBBA, EBBA, and MBV, only one mixture, that of EBBA and MBV, showed the formation of the extra peak. In addition, some A40 was formed in a mixture of A10 and butoxybenzaldehyde, while some A10 was formed from a mixture of A40 and anisaldeyde. Recently, Nagy[5] showed that the amine moiety of a Schiff base can exchange with a free amine in aqueous solution.

4. Exchange Reactions

Sufficient experimental evidence exists to show that mixtures of Schiff bases undergo exchange reactions to form a new mixture composed of all possible combinations of aldehyde and amine moieties present. The exchange takes place through the presence of the free aldehydes and amines. The original mixture will only remain unchanged if either all of the original aldehyde or all of the original amine moieties are the same.

During the course of research into the development of wide-temperature-range nematic materials, a material called DOCA (structure III) was synthesized for incorporation into mixtures.

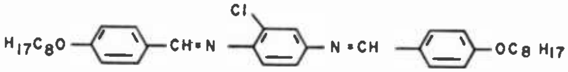

Structure III

Mixtures of DOCA, MBBA, and EBBA were prepared. However, different batches of the mixture showed different transition temperatures. Since DOCA is a di-Schiff base with an unsymmetrical amine moiety, a large number of new Schiff bases could be formed from it. It was predicted that nine new compounds would appear to make a total of 12 components in the mixture. Liquid–liquid chromatography showed the presence of at least 8 resolvable components. It is believed that the other components are present, but that they could not be resolved under the conditions used. The DOCA compound was approximately 70% by weight of the original blend. It was probably less than about 5% in the equilibrated mixture.

It has been assumed that exchange takes place because of the presence of the free aldehyde and amine rather than by any other mechanism, e.g., a four-center reaction, as this seems the most plausible mechanism. The exchange reactions are slow and the rate depends on the water content. An increase in the water content results in an increase in the concentration of the aldehyde and amine and causes the exchange to proceed more rapidly. Kinetic data presented in the next section confirm that the reaction rate increases with increasing water content.

The melting point and the nematic–isotropic transition point are generally different for each Schiff base. For any mixture of two or more Schiff bases, the temperatures corresponding to these points depends on the composition of the mixture. If the mixture changes in composition through the interconversion described above, the nematic range of the mixture changes. For instance, a freshly prepared sample of APAPA-WRT (No A42) becomes isotropic at 107.5°C.; at equilibrium, the transition temperature falls to 102°C. The equilibrium also accounts for the irreproducibility of the data of Pohl and Steinstrasser.[4] These authors presented data for 22 "binary" mixtures. However, only three of these mixtures were truly binary; the remainder were all four-component systems of indeterminate composition. The transition temperatures change as a function of the time elapsed between the preparation of the mixture and the determination of these temperatures. It should be pointed out that the behavior discussed is applicable to Schiff bases in general, whether or not they are liquid crystals.

5. Kinetics of the Exchange

If the exchange in the APAPA-WRT is through the presence of the free aldehyde and amine, then an increase in their concentrations will cause an increase in the rate of exchange. The addition of water will increase the aldehyde and amine concentrations and, hence, should cause an increase in the exchange rate. It was decided to investigate the effect of water content on the exchange rate. The APAPA-WRT mixture was chosen for the study and the rate of formation of A42 was monitored. The components of the WRT blend were prepared in the following way:

APAPA-10 (A10)—APAPA-phenol (structure IV) was reacted with acetic anhydride in pyridine. The crystalline product was recrystallized from hexane until constant transition temperatures were obtained.

Structure IV

APAPA-12 (A12)—Same as A10 except that butyric anhydride was used.

APAPA-40 (A40)—Butoxybenzaldehyde was mixed with p-aminophenol in benzene and the water removed by azeotropic distillation. The product was recrystallized from benezene and then reacted with acetic anhydride in pyridine. The product was recrystallized from hexane until constant transition temperatures were obtained.

The three materials met the criteria shown in Table 4. The resistivity in Table 4 is the geometrical resistivity measured between indium-oxide-coated glass electrodes spaced 1 mil apart. The cell is 3.175 cm square. The voltage imposed on the cell was 20 volts dc and the cell was kept at a temperature of 85°C for the measurement.

The blend was made by mixing the components in the following molar concentrations: A10, 32.5%; A12, 47.5%; and A40, 20.0%. The mixture was heated in a glass beaker and stirred magnetically until the isotropic liquid was obtained at about 120°C. The mixture was heated for approximately 30 minutes and was then set aside to cool; all heating and cooling took place in a nitrogen-filled dry-box. When the mixture was cool, it was filtered through a 0.25-μm millipore filter. All individual compounds and the finished fluid were checked for purity by liquid–liquid chromatography. The blend did not show any A42 after the mixing.

Table 4—Characteristics of Materials Used in APAPA-WRT Blend

Characteristic	A10	A12	A40
Melting Point	83-84°	52-53°	81-82°
Nematic-Isotropic Point	107-108°	109-110°	112°
Resistivity at 85°C (ohm-cm)	2.5×10^9	5×10^{10}	2.5×10^{10}

Fifteen grams of the mixture were weighed into six clean 50-milliliter serum vials. One vial, No. 2, was degassed at 65°C for four hours in a vacuum oven. Deionized water was added to four other vials, Nos. 3, 4, 5, and 6, to give the desired water content; the greatest amount added was 0.8%. Vial No. 1 contained the original blend. All of the vials were then flushed with nitrogen, sealed with Viton serum caps and aluminum closures, and placed in an environmental chamber at 30°C. Samples were removed with a hypodermic syringe at the desired intervals. Analysis for the A42 content was carried out by liquid–liquid chromatography under the conditions shown in Table 2. The external standard method was used; pure A42 was the standard. The external standard method is not particularly accurate, because the sensitivity of the chromatograph varies with each run; accuracy is probably no better than ±10%. It was not possible to analyze for A12 or A42, as the peaks for these compounds overlapped; A10 was not measured. At the end of the test, the water content was measured by the Karl Fischer method. The final water content was always less than the initial value, as some of the water was consumed in the formation of the aldehyde and amine.

The overall reaction is simplified to

$$A12 + A40 \leftrightharpoons A10 + A42.$$

The rate equation for this reaction is

$$\frac{d[\mathrm{A42}]}{dt} = k_1[\mathrm{A12}]\ [\mathrm{A40}] - k_2[\mathrm{A10}]\ [\mathrm{A42}], \qquad [5]$$

where k_1 is the rate constant for the forward reaction and k_2 the constant for the reverse reaction. The equation does not indicate which process is dominant, the hydrolysis of the A12 or A40 or the recombination of the aldehydes and amines to form A10 and A42. Of course, both reactions may occur at the same speed.

5.1 Rate and Equilibrium Constants

In stating kinetic results, concentrations are usually expressed in moles per liter. The density of the WRT mixture is initially 1.1 g/cm^3. The weight of one liter is, therefore, 1100 grams. It is assumed that the density of the WRT mixture does not change during the formation of A42. Therefore, the total weight and the total number of moles in one liter remains unchanged. Concentrations are expressed in moles per liter and the rate constants have dimensions of liters per mole-second.

Let the concentration of A42 at time t be x. The initial concentration of A12 is B, of A40 D, and of A10 E. The initial concentration of A42 is, of course, zero. Then, at time t, the concentrations are

A12	$(B\text{-}x)$
A40	$(D\text{-}x)$
A10	$(E+x)$
A42	x

as one mole each of A10 and A42 are formed for each mole of A12 and A40 that disappear. Eq. [5] then becomes:

$$\frac{dx}{dt} = k_1(B\text{-}x)\,(D\text{-}x) - k_2(E+x)\,x. \qquad [6]$$

The equilibrium constant for the reaction is

$$K = \frac{k_1}{k_2} = \frac{[\mathrm{A10}]\ [\mathrm{A42}]}{[\mathrm{A12}]\ [\mathrm{A40}]}.$$

Then Eq. [6] becomes

$$\frac{dx}{dt} = k_1(B\text{-}x)(D\text{-}x) - \frac{k_1}{K}(E+x)x. \qquad [7]$$

This expression reduces to

$$\frac{dx}{a + bx + cx^2} = k_1(dt), \qquad [8]$$

where $a = B \cdot D$

$$b = -\left(B + D + \frac{E}{K}\right)$$

$$c = \left(1 - \frac{1}{K}\right)$$

$$q = b^2 - 4ac.$$

Integration of Eq. [8] gives:

$$\ln \frac{2cx + b - q^{1/2}}{2cx + b + q^{1/2}} = q^{1/2} k_1 t + \text{constant}. \qquad [9]$$

The initial conditions are $x = 0$ at $t = 0$. Then Eq. [9] becomes

$$\log \frac{x + (b - q^{1/2})/2c}{x + (b + q^{1/2})/2c} = \frac{k_1 q^{1/2} t}{2.303} + \log \frac{(b - q^{1/2})}{(b + q^{1/2})}. \qquad [10]$$

However, the A42 concentration is determined in weight-percent. These values must be converted to moles per liter before they can be used in the rate equation, Eq. [11]. Initially, the WRT mixture has the composition shown in Table 5. The mean molecular weight of the mixture is 291.05 grams, and 100 grams contain 0.3436 mole. The molecular weight of A42 is 339.4 grams. If, at time t, the concentration of A42 is S weight-percent, then the number of moles of A42 in 100 grams is $S/339.4$. Now, because 1 liter contains 1100 grams, the concentrations of the compounds in the mixture at time t,

Table 5—Initial Composition of WRT Mixture

Component	Mole-Percent	Weight-Percent	Molecular Weight	Number of Moles in 100 Grams
A10(E)	32.5	30.07	269.3	0.1117
A12(B)	47.5	48.53	297.4	0.1632
A40(D)	20.0	21.40	311.4	0.0687

in moles per liter, are:

A10	$(1.229 + 11S/339.4)$
A12	$(1.795 - 11S/339.4)$
A40	$(0.7557 - 11S/339.4)$
A42	$11S/339.4$

The total number of moles in 1 liter remains unchanged if one neglects aldehyde and amine concentrations. The concentration of A42 in weight-percent and in moles per liter is shown in Table 6. The value in moles per liter is plotted against time in Fig. 1. The concentration increases with time and reaches an equilibrium value at about 0.5 mole per liter or 15 weight-percent.

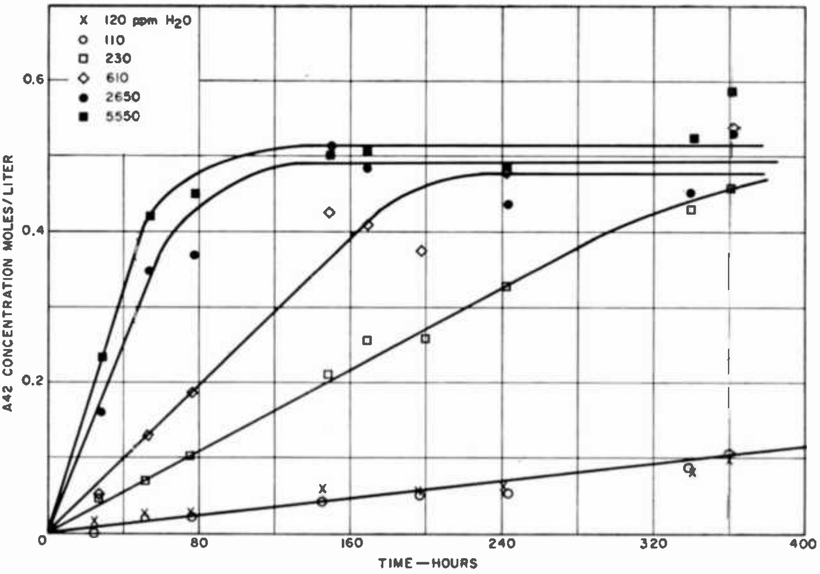

Fig. 1—Concentration of A42 in moles per liter as a function of time.

Table 6—Effect of Water and Time on A42 Formation

Sample Number	Time (Hours)	A42 Weight (Percent)	A42 Moles/ Liter
1 Control—no water added. Final water content 131 W/V ppm or 120 W/W ppm	24.75	0.47	0.0154
	51	0.82	0.0264
	75.5	0.86	0.0275
	145	1.80	0.0583
	196	1.76	0.0572
	241.5	1.92	0.0627
	341	2.67	0.0869
	360	3.05	0.0990
2 Degassed—Final water content 112W/V ppm or 110 W/W ppm.	24.75	BARELY DETECTABLE	
	51.5	0.66	0.0220
	76	0.75	0.0242
	145	1.34	0.0429
	196	1.68	0.0539
	243	1.70	0.0550
	339.5	2.73	0.0880
	360	3.31	0.1078
3 0.06 percent added water. Final water content 252 W/V ppm or 230 W/W ppm.	27	1.46	0.0473
	52	2.13	0.0693
	76	3.22	0.1045
	147.5	6.53	0.2112
	169	7.90	0.2552
	197	8.01	0.2596
	243	10.20	0.3300
	340	13.27	0.4301
	360	14.16	0.4587
4 0.15 percent added water. Final water content 670 W/V ppm or 610 W/W ppm.	27.5	1.88	0.0517
	53	3.96	0.1287
	76.5	5.73	0.1859
	148	13.12	0.4257
	168.5	12.71	0.4114
	197	11.58	0.3715
	241	14.75	0.4785
	341	13.99	0.4532
	361	16.62	0.5390
5 0.32 percent added water. Final water content 2920 W/V ppm or 2650 W/W ppm.	28	4.98	0.1617
	53.5	10.76	0.3487
	77	11.41	0.3696
	148.5	15.87	0.5148
	168.5	15.01	0.4862
	243	13.55	0.4389
	340	14.01	0.4547
	361	16.48	0.5346
6 0.75 percent added water. Final water content 6000 W/V ppm or 5555 W/W ppm.	28.5	7.30	0.2365
	54	13.01	0.4213
	77	13.86	0.4488
	149	15.52	0.5027
	169	15.68	0.5082
	242	15.03	0.4873
	341	16.14	0.5225
	361	18.78	0.5885

Before the rate constant can be determined, however, the value of K, the equilibrium constant, must be found. K is found from the value of the A42 concentration at the points of equilibrium. If the A42 concentration is known, then the concentrations of all other major components can be calculated. Values of K are shown in Table 7; the average value is 2.56. Since a, b, c, and q can be found from the initial concentrations and K, Eq. [10] reduces to

Table 7—Values of the Equilibrium Constant

Sample Number	Time (Hours)	Equilibrium Constant, K
4	241	2.24
	341	1.88
	361	3.50
5	148.5	2.91
	168.5	2.36
	243	1.70
	340	1.89
	361	3.38
6	149	2.66
	169	2.77
	242	2.38
	341	3.08
	Mean	2.56

$$\log \frac{x - 4.476}{x - 0.4976} = 1.053 k_1 t + 0.955. \qquad [11]$$

k_1 can be found by plotting $\log x - 4.476/(x - 0.4976)$ against time t as shown in Fig. 2. The slope is $1.053k_1$. Obviously, as x approaches 0.4976, any error in x will be greatly compounded. Some experimental points had to be omitted because x exceeded 0.4976. For this reason, only the lower experimental values of x are used for samples 5 and 6. The reaction in these cases is also completed quickly. If k_1 is known, then k_2 can be found since $K = k_1/k_2$. The rate constants are shown in Table 8 and Fig. 3. The rate constants increase with increasing water content, but the rate of increase falls off at the higher water content. This effect, if real, may be caused by the fact that the saturation level for water in the WRT liquid crystal is being reached.

No attempt was made to fit the data to any other rate equation. Also, it is not known if either of the two reactions, hydrolysis of the

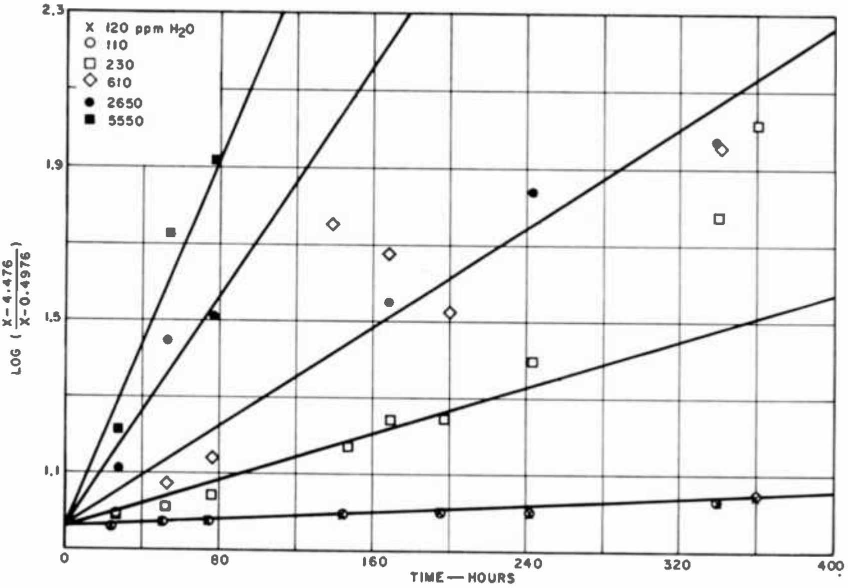

Fig. 2—Graph used to determine value of k_1.

Schiff bases or combination of the aldehydes and amines, is the rate-determining step. Of course, both may be of the same rate. Some work was carried out on the equilibrium between p-methoxybenzylidene-p-butylaniline (MBBA) and water. Qualitatively, the rate was about the same as that observed for the formation of A42. The addition of

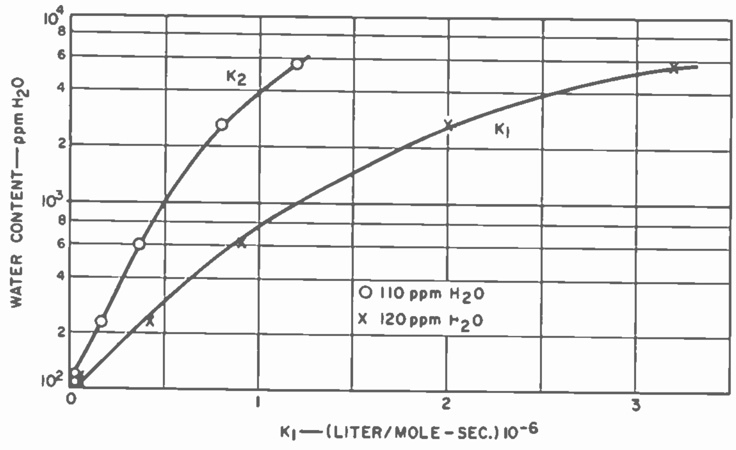

Fig. 3—Plot of values of rate constants.

water also increases the rate. In the kinetic study of WRT, the water content decreased during the course of the study; the effect of this decrease on the rate is not known. Also, the sample containers were not stirred continuously. The WRT mixture used in this study was specially made for the study, but it was the second batch made. The components of the first batch were slightly substandard. Analysis conducted immediately after the blending showed that the equilibrium amount of A42 had been formed. Apparently something in the substandard components had catalyzed the exchange, but the catalyst is not known.

Table 8—Values of the Rate Constants

	Water Concentration (ppm)			
Sample	W/V	W/W	K_1	K_2
1	131	120	6.9×10^{-8}	2.7×10^{-8}
2	122	110	6.9×10^{-8}	2.7×10^{-8}
3	252	230	4.3×10^{-7}	1.7×10^{-7}
4	670	610	9.1×10^{-7}	3.6×10^{-7}
5	2920	2650	2.0×10^{-6}	8.0×10^{-7}
6	6000	5555	3.2×10^{-6}	1.2×10^{-6}

The weight/volume concentration was determined experimentally.
The weight/weight concentration was obtained using a mixture density of 1.1 g/cm^3.

For all of the reasons given, care should be taken in applying the kinetic results described. Even though the data fit a second-order equilibrium reaction, they could conceivably fit some of the other rate equations and should not, therefore, be applied too strictly. However, the results give a reasonable indication of the exchange rates for good-quality Schiff bases, although those rates can be higher if suitable catalysts can be found. Substandard materials do cause alignment problems and result in displays with poor lifetimes.

6. MBBA–Water Equilibrium

Since the equilibrium between a Schiff base and water is one of the basic properties of the Schiff base, it was decided to study such an equilibrium. The Schiff base chosen was p-methoxybenzylidene-p′-n-butylaniline (MBBA). MBBA was prepared by mixing anisaldehyde and p-butylaniline and removing the water formed by drying with anhydrous magnesium sulfate. The liquid was purified by molecular distillation until the nematic-isotropic temperature was at least 45°C and the resistivity was greater than 10^{11} ohm-cm. The resistivity was measured by the same method as used for the APAPA compounds in the previous section except that measurements were made at 25°C. About 10 grams of MBBA were weighed into a clean 30-milliliter serum vial. Deionized water was added to the vial to yield the required water content; the highest concentration was 0.8 weight-percent. The water content always decreased during the study as some water was always consumed during the hydrolysis of the Schiff base. The vials were then flushed with nitrogen and capped with Viton serum caps and aluminum closures. Samples were removed with a hypodermic syringe. The mixtures were allowed to stand for three months at 30°C and were shaken periodically. The anisaldehyde and butylaniline contents were measured by liquid–liquid chromatography under the conditions shown in Table 2 with benzyl alcohol as an internal standard. Measurement by this method is the most accurate. Table 9 shows the excellent reproducibility of this method. The final water content was measured by the Karl Fischer method. It was assumed

Table 9—Analytical Results for MBBA–H_2O Mixtures

Sample	H_2O	Anisaldehyde	Butylaniline	MBBA
1	0.0833	0.99	1.24	97.6867
	0.0846	0.99	1.07	97.8554
AVERAGE	0.0840	0.99	1.15	97.7710
2	0.208	1.89	1.90	96.002
	0.211	1.74	1.88	96.169
AVERAGE	0.210	1.82	1.89	96.086
3	0.111	1.14	1.41	97.339
	0.104	1.14	1.37	97.386
AVERAGE	0.108	1.14	1.39	97.362
4	0.126	1.67	1.53	96.674
	0.128	1.59	1.57	96.712
AVERAGE	0.127	1.63	1.55	96.693
5	0.203	2.01	1.99	95.797
	0.214	1.77	1.90	96.116
AVERAGE	0.209	1.89	1.95	95.956
6	0.467	2.75	2.87	93.913
	0.480	2.71	2.92	93.890
AVERAGE	0.474	2.73	2.90	93.902

All concentrations are given in weight-percent. Water contents are measured on a weight/volume basis. The values are converted to a weight/weight basis under the assumption that MBBA has a density of 1.05 g/cm³. The water concentration given is that measured at the conclusion of the test.

Table 10—Equilibrium Constant for MBBA—H_2O

Sample	H_2O Concentration	Equilibrium Constant, K
1	0.084	7.2
2	0.210	5.9
3	0.108	6.6
4	0.127	4.9
5	0.209	5.4
6	0.474	5.6
		Mean 5.9
		$\sigma = \pm 0.77$

that MBBA made up the remainder of the mixture. Values of the equilibrium constant defined in Eq. [3] are listed in Table 10. Eq. [3] assumes that the activity coefficients are unity. The higher the water content, the higher the aldehyde and amine concentration, and the lower the nematic-isotropic temperature. Typically, MBBA prepared to the specifications cited above contains approximately 100 ppm of water, approximately 0.4% each of anisaldehyde and butylaniline, and has a transition temperature of 45°C. Pure MBBA would probably have a transition temperature of 48°C, but this temperature had not been attained because some water is always present.

The Schiff base reaction is exothermic; by bond-energy calculations it is 6 kilocalories exothermic. Substitution of the known values into Eq. [2] yields a value for K of 2.4 at 60°C. The importance of the equilibrium data is that most display devices contain Schiff bases; many, in fact, contain MBBA. The equilibrium is low and decreases with increasing temperature. Table 11 shows the equilibrium concentrations of anisaldehyde and butylaniline in MBBA as water content varies. It seems reasonable to assume that most other Schiff bases would have constants of about the same value.

Table 11—Calculated Equilibrium Concentrations

Anisaldehyde (Weight-Percent)	Butylaniline (Weight-Percent)	MBBA (Weight-Percent)	H_2O (ppm)
0.5	0.5	99.0	150
0.4	0.4	99.2	100
0.3	0.3	99.4	54
0.2	0.2	99.6	24
0.1	0.1	99.8	6
0.05	0.05	99.9	1.5

All concentrations are in weight-percent except for water which is in ppm.

7. Conclusions

A Schiff base is in equilibrium with the corresponding aldehyde and amine. This study shows that, in a mixture of Schiff bases, the individual aldehydes and amines can combine in every possible combination. These combinations lead to the formation of additional Schiff bases unless the original aldehyde or amine moieties are the same. Unless such mixtures are fully equilibrated their physical properties are subject to change.

The kinetics of exchange in one system were studied. The rate is low and increases with increasing water concentration.

Finally, the equilibrium existing between one Schiff base (p-methoxybenzylidine-p′-n-butylaniline) and water was studied and the constant found to be 5.9 at 30°C.

References:

[1] R. Williams, "Domains in Liquid Crystals," **J. Chem. Phys.,** Vol. 39, p. 384, 15 July 1963.

[2] G. H. Heilmeier, L. A. Zanoni, and L. A. Barton, "Dynamic Scattering: A New Electrooptic Effect in Certain Classes of Nematic Liquid Crystals," **Proc. IEEE,** Vol. 56, p. 1162 (1968).

[3] J. Goldmacher, J. Castellano, and M. McCaffery, private communication.

[4] R. Steinstrasser and L. Pohl, **Z. Naturforsch. B,** Vol. 26, No. 2, p. 87 (1971).

[5] P. Nagy, "Reaction of Schiff Bases with Primary Amines," **Magy. Kem. Foly.,** Vol. 77(1), p. 53 (1971) (**Chem. Abs.,** Vol. 74, 1971, Abs. No. 141133).

Fluorescence Switching by Means of Liquid Crystals

Robert D. Larrabee

RCA Advanced Technology Laboratories, Somerville, N.J.

Abstract—A feasibility study was undertaken to determine whether some of the techniques currently used to control visible light adsorption in nematic liquid crystal systems could be adapted for use in controlling fluorescence intensity. It was found that some materials are highly fluorescent and somewhat pleochroic when dissolved in (heated) nematic p-n-butoxybenzoic acid, but no materials were found that exhibit both of these properties when dissolved in presently available room-temperature nematics.

Introduction

Although the phenomenon of photoluminescence (or, as it is more often called, fluorescence) has been a laboratory curiosity for many years, it has become, only recently, an important analytical laboratory tool. This is clearly indicated by the rapidly increasing number of scientific papers and reviews on fluorometry published each year in such diverse fields as analytical chemistry, clinical pathology, oceanography, biochemistry, geology, pharmacology, forensic chemistry, and many others. The commercial exploitation of fluorescence phenomena however, lags far behind present use in the laboratory. Industry has made good use of other types of luminescence (e.g., cathodoluminescence and electroluminescence), but only recently has it begun to look favorably upon photoluminescence as a way to make new and/or better products.

One potential use for fluorescent phenomena is in displays. The increasing use of fluorescence in passive displays portends application in active displays provided a scheme could be found for varying the fluorescent intensity of some material by electronic means. In such a system, the energy for the light emitted by the display could be supplied easily and efficiently by invisible near-ultraviolet light. Hopefully, the electronic energy required to control the fluorescent intensity of the display would be small and compatible with integrated circuits. A fluorescent display of this type may be particularly useful in those applications where the display should stand out brightly against a background illuminated with only a small amount of visible ambient light (e.g., airplane cockpits, automotive dashboards, and control consoles on ships). In addition, it may also be possible to make use of the natural ultraviolet in sunlight or the artificially generated ultraviolet in fluorescent lamps to augment any display using ambient visible light (e.g., liquid-crystal displays utilizing dynamic scattering[1]) to make the display appear brighter.

Some structurally unsymmetrical dyes have the property (called pleochroism) that their optical absorption is a strong function of the electric field direction of the light relative to their molecular axes. When such a pleochroic dye is dissolved in a nematic liquid-crystal solvent, any orientation of the liquid-crystal solvent can also orient the dissolved dye, thereby affording a way to control its ultraviolet absorption and, thus, its fluorescence. Switching of the absorption of visible polarized light has already been demonstrated by G. H. Heilmeier et al[2] in solutions of *nonfluorescent*, pleochroic dyes in nematic liquid-crystal solvents. The present scheme to control fluorescence is an application for this mechanism at ultraviolet wavelengths.

The initial experiments clearly indicated the difficulty in finding materials that are strongly fluorescent when dissolved in the present room-temperature nematics and the fact that the present room-temperature nematics are all relatively opaque to near-ultraviolet light. G. Heilmeier[3] suggested that the higher temperature, single aromatic-ring liquid crystals may be virtually transparent in the near ultraviolet and that the presence of a -COOH group on some of these materials (such as p-n-butoxybenzoic acid) increases the polar nature of the molecule, thus increasing the tendency of a dissolved dye to fluoresce. These predictions proved to be correct and, as discussed below, several materials were found that were both strongly fluorescent and somewhat pleochroic when dissolved in nematic p-n-butoxybenzoic acid. Visible fluorescence switching in conventional liquid-crystal cells illuminated by *unpolarized* near-ultraviolet light was demonstrated, but, when using the best materials found, the fluorescent intensity varied by a factor of three at most. It was concluded, therefore, that any application of the present scheme to practical displays will have to await the discovery of more pleochroic fluorescent materials.

Fluorescence in the Host-Liquid Crystals

For a nematic liquid crystal to be acceptable for the present purpose, it must exhibit two basic properties in addition to liquid crystallinity:

[1] It must be relatively transparent in the near ultraviolet in order to allow the exciting radiation to reach the dissolved fluorescent dye.

[2] It must provide a suitable molecular environment for the dissolved dye molecules so that they will fluoresce strongly when excited by near-ultraviolet light.

Experiments with room-temperature nematics manufactured by several companies* indicated that they did not satisfy either of these criteria.

G. Heilmeier suggested[3] that the undesirable near ultraviolet adsorption of the room-temperature nematics might be due to the coupled, multiple-aromatic-ring structure of these materials. He suggested that p-n-butoxybenzoic acid, which is nematic between 147°C and 161°C and has only one aromatic ring, might have its ultraviolet absorption shifted to shorter wavelengths and, perhaps, would be relatively transparent in the near ultraviolet. This hypothesis was tested by comparing the absorption of p-n-butoxybenzoic acid with the now classical liquid crystal, p-azoxyanisole, which has two coupled aromatic rings (See Fig. 1). Indeed, as shown in Fig. 2., the shift to a shorter wavelength does occur and p-n-butoxybenzoic acid is relatively transparent at the 366 nm wavelength of the desired fluorescence exciting radiation. Simple comparative qualitative tests with the room-temperature nematics reveal that p-n-butoxybenzoic acid is much more transparent in the near ultraviolet.

About half of 182 selected organic materials tested were visibly fluorescent when dissolved in nematic p-n-butoxybenzoic acid. Table 1 lists those materials exhibiting the strongest fluorescence intensity as

---

* Type LCI-1 liquid crystal manufactured by Liquid Crystal Industries, Turtle Creek, Pa.; Type VL-1047-N Liquid Crystal manufactured by Vari-Light Corp., Cincinnati, Ohio; and a proprietary RCA material.

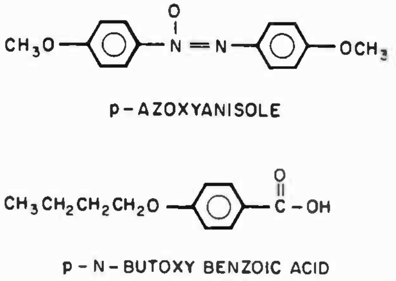

Fig. 1—Structural formulas for p-azoxyanisole and p-n-butoxybenzoic acid.

judged subjectively by comparison to a standard reference (Azosol Brilliant Yellow, listed on the first line of Table 1). There were many materials that had visible fluorescence that was lower in intensity than those listed at the bottom of Table 1 and were judged too low to be considered as useful for display purposes. It is also significant to note

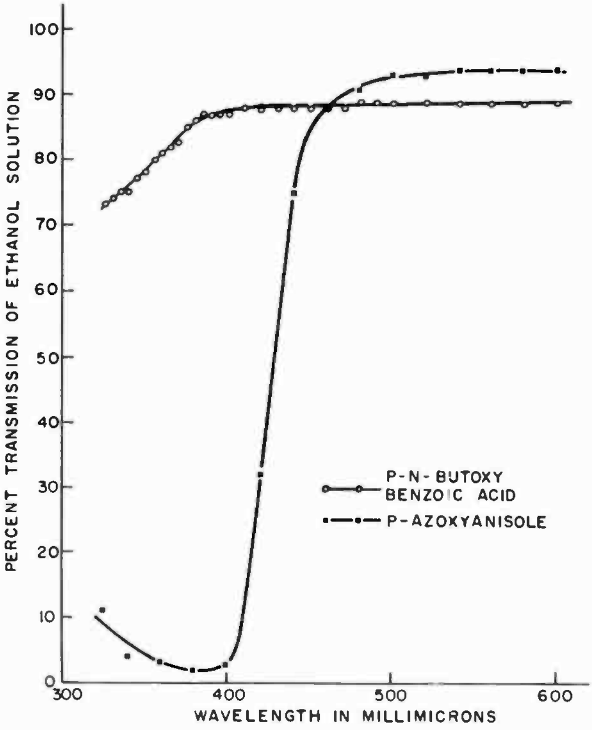

Fig. 2—Transmission of ethanol solutions of the liquid crystals of Fig. 1 as a function of wavelength.

that none of these materials were visibly fluorescent in p-azoxyanisole, or any of the room-temperature nematics mentioned above.

Consequently, p-n-butoxybenzoic acid satisfies both of the basic requirements listed above and, except for the inconvenience of having to heat it to its 147°C to 161°C nematic range, seems to be quite suitable for fluorescence switching experiments.

Table 1—Strongly Fluorescent Materials in Nematic p-Butoxybenzoic Acid

Material	Source*	Relative Fluorescence	Observed Pleochroism
Azosol Brilliant Yellow	GAF	Reference	None
Samaron Brilliant Yellow H6GL	Hoechst	Stronger	Strong
Perylene	Aldrich	Stronger	Fair
Brilliant Sulfo Flavine	Chroma	Stronger	None
p-Quinquiphenyl	K & K	Stronger	None
Fluoranthene	?	Stronger	None
9,10-Diphenylanthracene	Aldrich	Stronger	None
p-Sexiphenyl	K & K	Stronger	None
Brilliant Phosphine	Chroma	Same	Strong
Primulin 0	Chroma	Same	Strong
1,8-Diphenyl-1,3,5,7-octatetraene	K & K	Same	Strong
Acridine Yellow	Chroma	Same	Fair
Thioflavine S	Chroma	Same	Fair
Pyronin GS	Chroma	Same	Fair
1,12-Benzperylene	K & K	Same	Fair
Acriflavine	Chroma	Same	Poor
Ovalene	K & K	Same	Poor
Anthanthrene	K & K	Same	None
3,4,9,10-Dibenzpyrene	K & K	Same	None
3,4,8,9-Dibenzypyrene	K & K	Same	None
Rhodamine 6G	GAF	Poorer	Fair
Rhodamine 3G0	Chroma	Poorer	Fair
Rhodamine 6GD	Gurr	Poorer	Fair
Rhodamine B	Chroma	Poorer	Poor
Sulpho Rhodamine B	Hoechst	Poorer	Poor
Sulpho Rhodamine G	Hoechst	Poorer	Poor

* Address of sources as follows:

GAF—GAF Corp., Dyestuff and Chemical Div., 140 W. 51st St., N. Y., N. Y. 10020

Hoechst—American Hoeschst Corp., Dyes and Pigments Div., 270 Sheffield St., Mountainside, N. J. 07092

Aldrich—Aldrich Chemical Co., 10 Ridgedale Ave., Cedar Knolls, N. J. 07927

Chroma—Roboz Surgical Instrument Co., 810 18th St. NW, Wash., D.C. 20006

K & K—K and K Laboratories, Plainview, N. Y.

Gurr—George T. Gurr, Ltd., London S.W. 6, England

Pleochroism

For a fluorescent solute to be useful in the present fluorescence switching scheme, it must be pleochroic in the following sense. Its ultraviolet absorption, when aligned by the host nematic solvent, must be a strong function of the direction of the electric field of the incident light. Since such absorption is a prerequisite for fluorescence, its fluorescence emission will likewise be a similar function of the electric field direction of its exciting ultraviolet radiation. Perhaps the most practical scheme utilizing these ideas involves a fluorescent molecule with a long linear aspect wherein the ultraviolet absorption is greatest when the electric field of the exciting radiation is aligned parallel to the long axis of the molecule and least when perpendicular to it. With such a material, one can use front or rear *unpolarized* ultraviolet excitation of a flat liquid crystal cell and have *minimum* fluorescence with the voltage applied, thus aligning the long molecular axes perpendicular to the electrodes and, at the same time, perpendicular to the electric field direction of the incident ultraviolet light. Removal of the voltage allows the nematic liquid to realign itself (and the fluorescent solute) parallel to the rubbed electrode surfaces, thus causing the fluorescent molecules to strongly absorb one component of the unpolarized excitation radiation. This increased absorption will then be evident as an increased fluorescence.

All of the materials listed in Table 1 were tested for pleochroism in a conventional 2-mil thick, tic-coated, rubbed liquid-crystal cell at a concentration in p-n-butoxybenzoic acid where they fluoresced brightly with no voltage applied. The decrease in fluorescence (if any) with applied voltage was noted and subjectively compared to a standard (perylene). Four materials were found that were judged more pleochroic than the standard and are thus rated strongly pleochroic in Table 1. The pleochroism of these four materials was then measured more quantitatively using a photocell to measure the change in fluorescence when a saturating voltage (about 40 volts) was applied to the same liquid-crystal cell. For these quantitative measurements, the weight concentration of fluorescent material was held constant at 0.01%, a value found to be optimum for the fluorescence of 1,8-diphenyl-1,3,5,7-octatetraene. Although the decrease in fluorescence with applied voltage could easily be seen by the eye and clearly illustrated the principle involved, it is judged too small for most display applications (see Table 2). Therefore, it was concluded that no material tested was both highly fluorescent and sufficiently pleochroic for display applications when dissolved in p-n-butoxybenzoic acid.

Conclusion

It was concluded that practical applications for this scheme will depend upon finding more strongly pleochroic materials that are also strongly fluorescent, not only in p-n-butoxybenzoic acid, but also in room temperature nematics as well. However, the basic principle of this scheme of fluorescence control has been demonstrated and the magnitude of the effect in some readily available materials has been measured.

Table 2—Measurements of Fluorescence Switching in p-n-Butoxybenzoic Acid Liquid-Crystal Cells

Fluorescent Material	*Ratio of on-to-off Fluorescent Intensities*
Brilliant Phosphine	3.0 to 1
Primulin 0	1.7 to 1
1,8-diphenyl-1,3,5,7-octatetraene	1.5 to 1
Samaron Brilliant Yellow H6GL	1.3 to 1

Acknowledgments

The author wishes to thank J. Castellano, S. Harrison, and D. L. Ross for supplying many of the materials used in this study and for their discussions relating to this project. In addition, the author wishes to thank G. Heilmeier, W. A. Hichinbothem, P. M. Schwartz, M. C. Steele, and R. Williams for many encouraging discussions.

References:

[1] G. H. Heilmeier, L. A. Zanoni, and L. A. Barton, "Dynamic Scattering: A New Electro-optic Effect in Certain Classes of Nematic Liquid Crystals," **Proc. IEEE**, Vol. 56, p. 1162 (1968).

[2] G. H. Heilmeier, J. A. Castellano, and L. A. Zanoni, "Guest-Host Interactions in Nematic Liquid Crystals," **Molecular Crystals and Liquid Crystals**, Vol. 8, p. 293 (1969).

[3] G. H. Heilmeier, Private Communication.

Blue-Green Numeric Display Using Electroluminescent GaN

J. I. Pankove

RCA Laboratories, Princeton, N.J.

Abstract—GaN Offers the possibility for dc electroluminescence over a broad range of wavelengths extending over the visible spectrum at room temperature. In particular, blue-green luminescence has been observed at 5190 Å with a power efficiency of 0.1% and a quantum efficiency of 1%. There is no evidence of gradual degradation over several months of continuous operation. For display purposes, the desired pattern is determined by the configuration of the evaporated electrodes.

Introduction

In commercial numerical displays made of $GaAs_{1-x}P_x$ or GaP, both the n- and p-type regions are highly conducting. Hence, to confine the luminescent area to the desired shape, the crystal must be segmented into small dots or narrow bars that are later reassembled on an insulating substrate.[1] In monolithic displays, this difficulty is replaced by a diffusion procedure. With GaN, on the other hand, the light is emitted under the electrode and therefore the luminous area is determined by the shape of the electrode.

Semiconductors used in commercial numeric displays are usually partly absorbing to the radiation they emit. To minimize this undesirable property, it is customary to use either "edge" emitters", in which one edge of the p-n junction faces the viewer, or "surface emitters", in which the viewer looks at the light scattered around the electrode while the electrode blocks a portion of the light. In the GaN numeric display, the light is viewed through a perfectly transparent crystal; all the electrodes are attached at the rear surface of the crystal.

Displays made of powdered or sputtered II-IV compounds require a high voltage (about 200 volts) for operation and suffer from gradual degradation. The GaN display can operate at less than 30 volts and shows no tendency to degrade its performance.

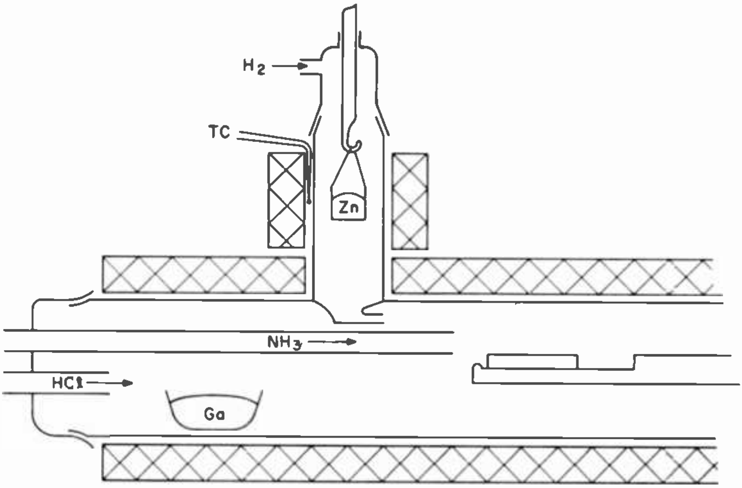

Fig. 1—Furnace for growing GaN.

Fabrication

The GaN is synthesized according to the method of Maruska and Tietjen[2] by reacting vapors of GaCl and ammonia in an open flow system, as illustrated in Fig. 1. The GaCl is produced inside the furnace by passing HCl over Ga. The GaN forms as a single crystal growing on a sapphire substrate. The growth rate is about 2 microns per minute. The undoped GaN is conducting n-type with a carrier concentration of about $2 \times 10^{18}\,\text{cm}^{-3}$ and a mobility of 130 cm^2/Vsec. After the first layer of undoped conducting n-type GaN has been grown, zinc is introduced into the growth chamber to dope the GaN with compensating acceptors. The resulting Zn-doped crystal is insulating. Then, metallic electrodes are evaporated on the Zn-doped layer to form the desired 7-bar pattern (Fig. 2). The crystal is cut into rectangles, leads are soldered to the evaporated electrodes, and an ohmic connection is made to the n-type layer. The device is ready to operate. However, to secure the leads beyond the strength of the soldered contact, a layer of epoxy is poured on the GaN crystal, thus embedding the ends of the leads. Black epoxy is used to minimize the reflection of ambient light. The light is emitted through the sapphire substrate, which results in a high contrast ratio against the black background of the epoxy.

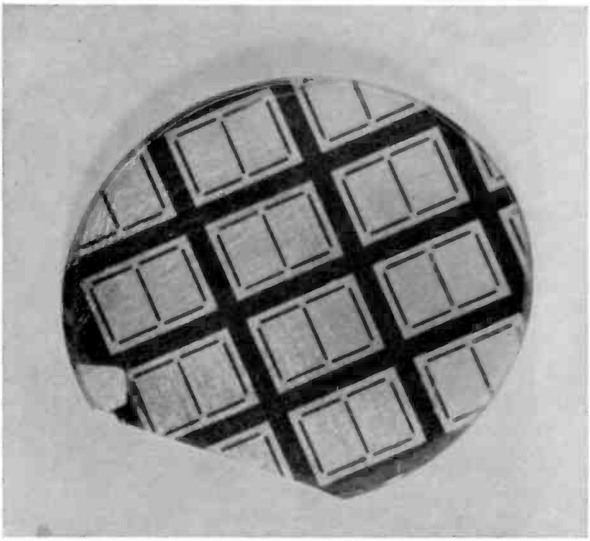

Fig. 2—Photograph of seven-bar numeric patterns on a GaN wafer viewed through the sapphire substrate. The wafer is about ¾-inch in the long dimension.

Device Physics

The structure of the device is essentially an M-i-n (metal-insulating-n-type) diode. Light is emitted inside the insulating layer at the cathode, i.e., under the metal electrode if the latter is biased negatively, or at the i-n interface if the metal is biased positively. Light is generated by a radiative transition of electrons from near the conduction band edge to a deep center consisting of a zinc acceptor-like complex (Fig. 3). This zinc center, which is normally occupied by an electron in the unbiased condition, becomes empty by field emission when a bias is applied. Only centers near the cathode are emptied, because the high electric field is localized at the cathode. Hence, it is at the cathode that field emission of the trapped electrons occurs. The emitted electrons appear in the conduction band and drift towards the anode. Some of the electrons that tunnel from the cathode to the conduction band in the high-field region make a radiative transition to the empty centers. The efficiency of this process is expected to be limited by the ratio of the transit time of the electron through the high-field region to the recombination time. Quantum efficiencies of 1% have been obtained, indicating that the capture cross section of this zinc center is very large.

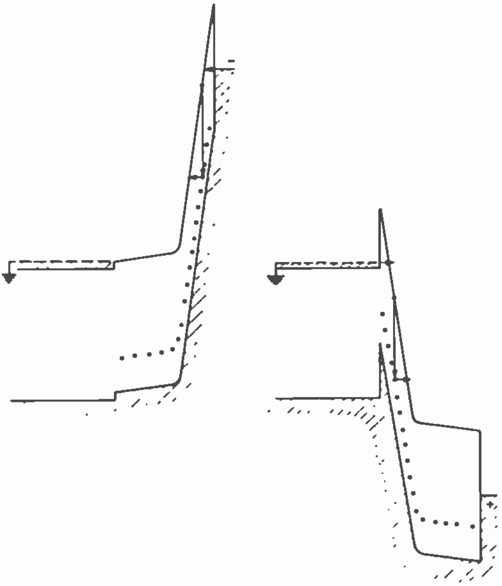

Fig. 3—Model of the physical principles involved in the electroluminescence of GaN.

The electroluminescence spectrum often depends on the polarity of the bias.[3] This variation may be attributed to a nonuniformity of doping along the direction of growth. Depending on doping conditions, electroluminescent peaks ranging from red to blue have been obtained, as shown in Fig. 4.

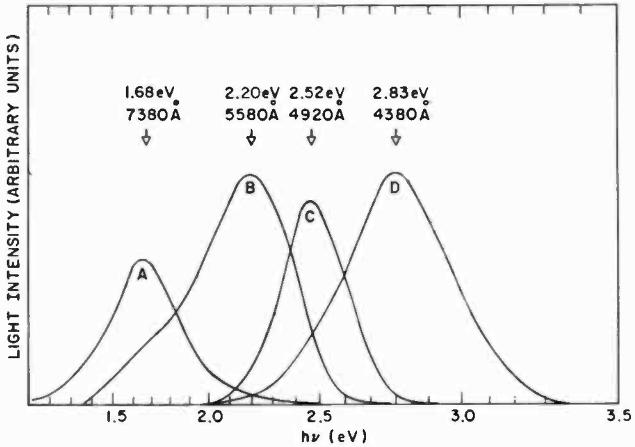

Fig. 4—Spectra obtained from variously doped GaN LED.

Device Characteristics

The *I(V)* characteristic of a gallium nitride M-i-n diode is shown in Fig. 5. The current rises rapidly with voltage until ~ 10 volts where an approximately quadratic dependence is obtained. Light is emitted in this quadratic region.

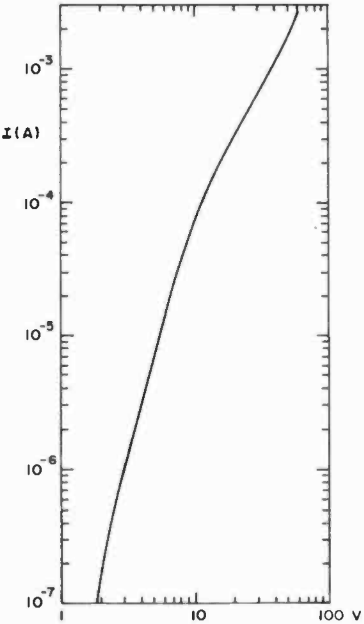

Fig. 5—*I(V)* characteristic of a GaN LED.

The light output rises rapidly at first and then becomes nearly linear with the input power (current × voltage) until ~ 0.1 watts, beyond which heating increases the efficiency of competing non-radiative transitions (Fig. 6). If the device is pulsed to prevent the diode from heating, the linear dependence of the output-input relation is extended to higher powers.

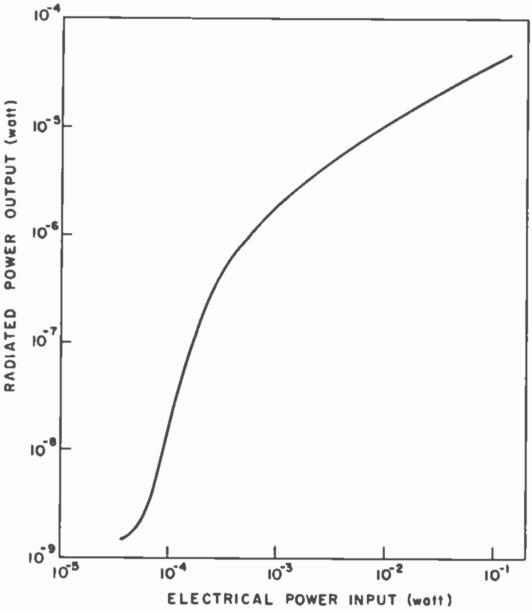

Fig. 6—Radiated power output at 5190 Å versus electrical power input for the GaN LED of Fig. 5.

From the data of Fig. 6, one can see that the highest power efficiency of the device is about 10^{-3}. Since each electron that emits a 2.5-eV photon is subjected to an approximately 20 volts drop, the quantum efficiency is ten times higher than the power efficiency, i.e., about 1%. For the application engineer, it is the power efficiency that matters. A power efficiency of 0.1% for the blue-green GaN emission compares favorably in brightness with the performance of the average commercial light-emitting display.

The emission spectrum of the blue-green-light-emitting GaN light-emitting diode (LED) is shown in Fig. 7. It peaks at 2.39 eV (5190 Å), and its linewidth is 0.41 eV. Because of the width of the emission spectrum, it is possible to increase the "blueness" of the display by covering the device with a suitable gelatin filter.

The brightness, or luminance, of the GaN LED is difficult to measure because of the small area of the emitter. However, a diode fabricated with a circular contact 400 μm in diameter produced a luminance of 300 fL (10^3 cd/m^2) at a current level of 2 mA and an applied voltage of 50 volts. This luminance value was confirmed by illuminating a white surface with a GaN lamp and then comparing the intensity of the illuminated surface with that from a filtered adjustable microscope illuminator. Another diode, having also a contact area of about 1×10^{-3}cm^2, had a luminance of 850 fL at 600 μA and 22.5 Volts.

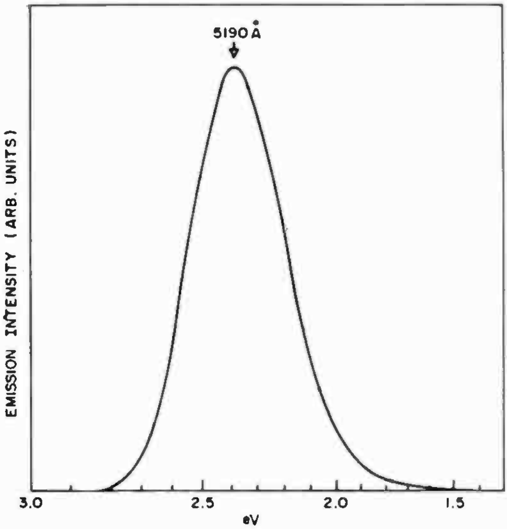

Fig. 7—Emission spectrum of GaN LED of Figs. 5 and 6 at 30 V and 450 μA.

Several diodes made from different wafers were subjected to a life test. Two diodes made from early crystals (one blue, the other green) showed unchanged performance over a period of four months. A third diode, made from a later crystal of the same material as the diode of Figs. 5 to 7, was tested for six months while running at an input power of 32 mW (Fig. 8) and showed no evidence of degradation.

Monolithic seven-bar numeric displays were fabricated as described above using other crystals. They were driven directly by a COS/MOS integrated circuit (an RCA CD4033 decade counter/divider). A bias of 17 volts was used to deliver about 300 μA per bar. Each bar measures 2 × 0.1 mm. A brightness of 150 fL ($\sim 5 \times 10^2$ cd/m^2) was obtained, with the emission peaking at 5165 Å. The brightness was fairly uniform over the surface of each crystal (within a factor of two) except for a few linear faults along which crystal growth appeared inhibited.

GaN promises a new class of numeric displays generating previously unattainable colors with highly acceptable brightness. The device technology is basically simple and the structure with back surface connections is a further advantage.

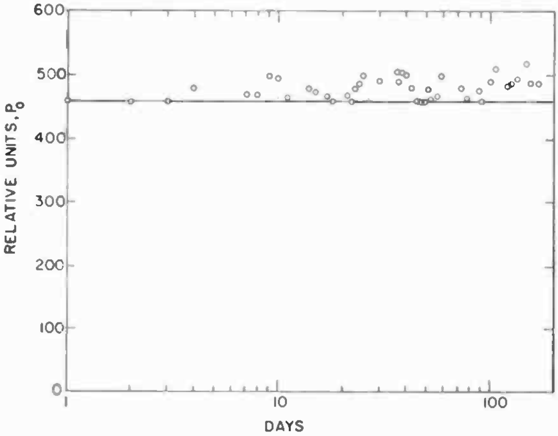

Fig. 8—Life test data for GaN LED. The instability is attributed to a noisy contact.

Acknowledgments

The author is grateful to E. A. Miller for growing the material, to M. Harvey for device processing, to J. E. Berkeyheiser for assistance with the measurements, and to H. Kressel, I. Ladany, and M. A. Leedom for valuable discussions.

References:

[1] A. A. Bergh and P. J. Dean, "Light-Emitting Diodes," **Proc. IEEE,** Vol. 60, p. 156, Feb. 1972; C. J. Nuese, H. Kressel, and I. Ladany, "The Future for LEDs," **IEEE Spectrum,** Vol. 9, p. 28, May 1972; R. K. Jurgen, "What's New in Small Displays," **IEEE Spectrum,** Vol. 9, p. 19, Nov. 1972.

[2] H. P. Maruska and J. J. Tietjen, "The Preparation and Properties of Vapor-Deposited Single Crystalline GaN," **Appl. Phys. Letters,** Vol. 15, p. 327 (1969).

[3] J. L. Pankove, E. A. Miller, and J. E. Berkeyheiser, "GaN Yellow-Light Emitting Diodes," **J. Luminescence,** Vol. 6, p. 54, Jan. 1973; J. I. Pankove, "Luminescence in GaN," Proc. Conf. Physics and Tech. of Light Emitters and Detectors, Pugnochiuso, Italy, 1972 (to be published in **J. Luminescence**).

Fast Five-Stage Photomultiplier with GaP(Cs) Dynodes

D. E. Persyk and D. D. Crawshaw
RCA Electronic Components, Lancaster, Pa.

Abstract—The use of negative-electron-affinity materials as secondary emitters results in marked performance improvements in photomultiplier detectors. This paper treats the developmental type C31024 photomultiplier, which utilizes five GaP(Cs) dynodes to provide gains of the order of 5×10^6. The high secondary-emission ratio (greater than 20) of the GaP(Cs) dynodes permits the electron-multiplier section of the device to resolve photoelectron inputs consisting of 1, 2, 3, or 4 electrons as discrete events. The single-electron anode pulse rise time is 800 ps. Data are presented on time- and frequency-domain measurements, and a comparison of measurement techniques is presented. Applications in the fields of laser-light detection and medical electronics are discussed.

Introduction

There is an increasing need for photomultiplier detectors with fast response. Laser technology requires fast photomultiplier tubes (PMT's) for the investigation of picosecond pulses and the detection of radio-frequency-modulated laser light. The expanding field of medical electronics requires PMT's with fast pulse response. These fast PMT's, along with the concept of pulse-shape discrimination between signal and noise events, allow the design of a liquid scintillation system using only a single tube. In the area of high-energy physics, the accelerator at the National Accelerator Laboratory, Batavia, Ill., produces particle fluxes that tax the count-rate capability of most existing conventional PMT's, indicating additional need for faster detectors with greater counting capabilities.

A PMT has been designed to meet these needs. It is designated the developmental type C31024 and utilizes negative-electron-affinity (NEA) GaP(Cs) dynodes in the electron-multiplier section of the detector. This paper reviews the development of the GaP(Cs) electron multiplier, cites recent data on C31024 performance, and discusses areas of applications for the device. An outline of intended future work on GaP(Cs) PMT's is also included.

GaP—A Secondary Emitter

The secondary emitters used in photomultiplier electron-multiplier sections have changed drastically in the last five years. This change has been the result of the discovery of the concept of Negative Electron Affinity (NEA) and the introduction of NEA materials as secondary emitters. The most promising, commercially, of these NEA materials are III-V compounds and foremost among these is GaP. GaP has been in use as a secondary emitter in PMT's for over four years. It is superior to any previously used secondary emitter in that the gain increases linearly with primary electron energy up to very high voltages.[1]

The advantages of an NEA secondary emitter can best be seen by examining the physical processes associated with the emission of secondary electrons. Briefly, secondary emission can be described as the result of three processes:

[1] Primary electrons provide enough energy (in excess of bandgap energy E_G) to excite electrons in the solid from the valence band into the conduction band.

[2] Some of the excited electrons move toward the solid–vacuum interface.

[3] Electrons with energy greater than the potential barrier (E_A) at the surface are emitted as secondary electrons.

Thus, for an excited electron to be emitted, it must acquire energy greater than $E_G + E_A$ (Fig. 1). The amount of energy in excess of

$E_G + E_A$ needed for emission will depend upon the depth from the surface at which the secondary is excited. As long as the secondary electrons are produced near the surface, the secondary-emission yield increases with increasing primary electron energy. As the depth of penetration of the primary electrons increases, the number of secondaries increases; however, because many secondary electrons are produced deep in the material, where the escape probability is small, the secondary-emission yield decreases. The relationship between primary energy and secondary emission ratio is shown for one conventional emitter, BeO, in Fig. 2. The escape depth for secondary electrons in BeO is limited by collisions with other electrons or with the lattice, as they diffuse through the lattice. Energy losses incurred during these inelastic collisions greatly decrease the path length of an electron.

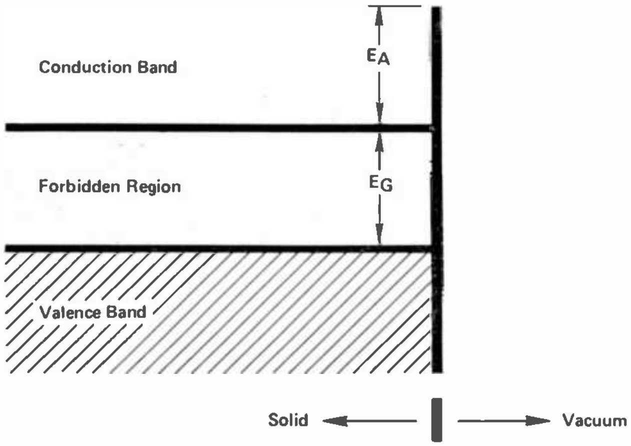

Fig. 1—Simplified energy diagram for a conventional secondary emitter.

The limitation on secondary emission yield is considerably reduced by the use of NEA secondary emitters.[1] These emitters use the reduction of the surface barrier and band bending that occur when an electropositive material such as cesium is deposited on a heavily doped, p-type semiconductor. Under these conditions, the conduction band in the bulk material is made to lie entirely above the vacuum level, as shown in Fig. 3. Therefore, electrons excited into the conduction band of the semiconductor can still be emitted even after they have become thermal electrons.

With NEA materials, electrons can escape from distances at least

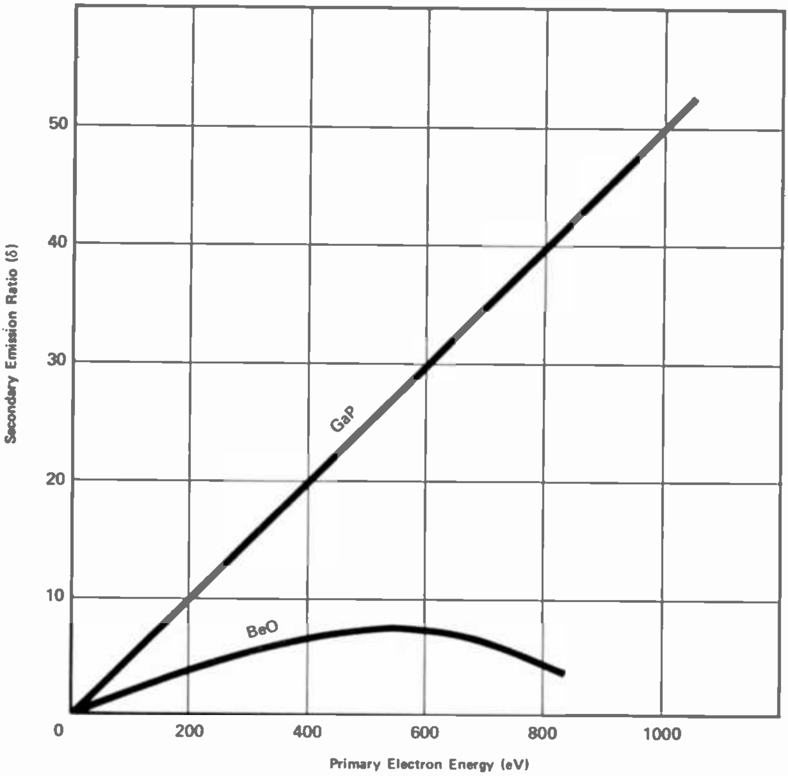

Fig. 2—Secondary-emission ratio versus primary-electron energy for BeO and GaP.

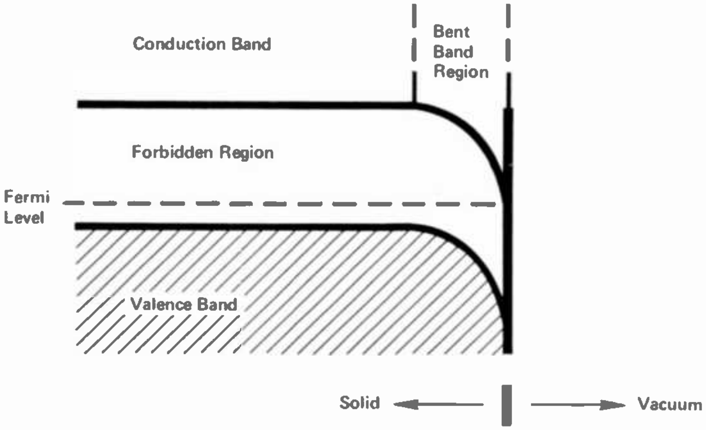

Fig. 3—Simplified energy diagram for an NEA secondary emitter.

an order of magnitude greater than that in conventional secondary emitters. Furthermore, most electrons excited into the conduction band, with the exception of some excited in the bent-band region, can be emitted into the vacuum. Such an emitter should, based on this information, have not only a high maximum secondary-emission ratio (Fig. 2) but also high efficiency. This improvement is in fact borne out by experiment. As an example, at 600 volts, secondary gains as high as 50 have been obtained in the C31024; in contrast, the maximum gain possible[2] for a conventional dynode material at that voltage is about 8.

Time Response of a GaP(Cs) PMT

Due to the higher gains, PMT's having NEA dynodes require fewer stages than do conventional electron multipliers. This advantage allows a more compact multiplier structure and, at the same time, provides faster response. Computer simulation yields a detailed analysis of the time broadening of an electron charge cloud as it goes through the multiplier chain. Qualitatively, if each dynode broadens the charge cloud by some amount, one would expect that fewer dynodes would result in less electron pulse broadening and, hence, faster response.

A study of the electron-optical properties of a photomultiplier requires the solution of the Laplace equation $\nabla^2 V = 0$ for the region of interest. The solution is customarily obtained by first applying symmetry relationships to the electrostatic region to reduce the 3-dimensional problem to a 2-dimensional one. After the boundary conditions and the general geometric layout are specified, the numerical solution to the Laplace equation is obtained by iterative relaxation methods.[3] Once the solution is obtained to sufficient accuracy, the calculations of equipotential surfaces, electric field lines, and electron trajectories can be made with relative ease. Thus, the computer simulation of an entire electrostatic PMT is practical and, in fact, is used to study fast photomultipliers.

The first important source of time broadening is the geometrical effect.[4] Here, differences in transit times are due not only to variations in the path lengths of individual electrons but also to nonuniform electric field strengths between various sections of any two dynodes. To solve this problem, it is possible to design the multiplier so that, in general, those electrons that have shorter than average transit times between any two dynodes will be compensated for and have longer than average transit times between the next two dynodes, and vice versa. In practice, this effect is achieved by varying path lengths between dynodes as shown in Fig. 4.

Another method for minimizing the geometrical time dispersion is to increase the potential difference between stages of the PMT.[5] When this is done, the fractional dispersion of the transit time may remain the same, but the total dispersion is less because the actual transit time has been lowered. The practical upper limit to the interstage potential in a GaP(Cs) PMT is set by field emission of the elements and electroluminescence of the insulating materials, both of which give rise to objectionable dark current.

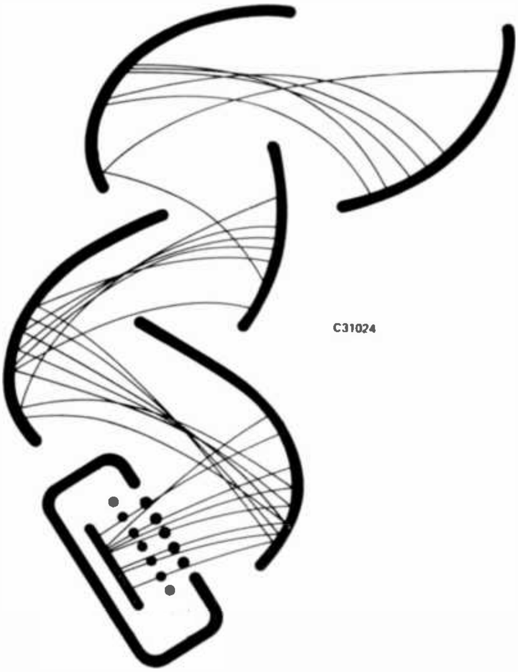

Fig. 4—Computer simulation of C31024 showing electron trajectory "compensation".

The second important source of time broadening in the electron multiplier is that due to the initial velocity differences of the secondary electrons. Computer analysis shows that initial velocity broadening becomes appreciable only when secondary electrons are emitted with energies greater than 4 eV.[5] Thus the energy distribution of the secondary electrons determines, in part, the severity of the time broadening. It is believed, however, that secondaries emitted from GaP(Cs) dynodes are essentially thermal electrons.[6] This is different from conventional secondary emitters whose emission energy distributions exhibit a peak around 3 eV.[7] Because most present-day PMT's are limited by geometrical time broadening and anode design, the effect of the "thermalized" electrons is not readily apparent. As with geometrical broadening, the velocity broadening effect can also be lessened by employing high interstage potentials.

Any multipliers designed to have fast responses require anodes with matched-impedance transmission lines. Most high-speed circuits are designed to utilize a 50-ohm impedance, which requires a 50-ohm transmission line within the tube and a suitable connector outside the tube to permit proper interface. Anode configurations and internal transmission lines may be analyzed by the use of standard methods of cavity and transmission-line analysis. These methods yield approximate design parameters,[8] which are then optimized experimentally by means of time-domain reflectometry (TDR).[9,10] TDR provides information about the discontinuities in the characteristic impedance of a system as a function of electrical length and is an extremely useful approach, not only in anode design but also in the design of voltage-divider circuits and mating sockets, neither of which lend themselves to mathematical analysis.

Electron Resolution

A second advantage of the high-gain GaP(Cs) dynode is reflected in the greatly enhanced electron resolution. Electron resolution is the ability of the electron multiplier section to distinguish between inputs that consist of 1, 2, 3 or up to 6 electrons simultaneously incident on the first stage of the multiplier.

The pulse-height distributions of multipliers with high-gain first dynodes, i.e., for low light levels, are entirely different from those obtained with a conventional multiplier.[11] Instead of having a single broad peak with its maximum at the average pulse height, the electron spectrum is resolved into a series of separate peaks corresponding to the times the signal produced just one photoelectron, two photoelectrons, three photoelectrons, and so on, as shown in the distribution in Fig. 5. With this high resolution of the single-electron peak and the multielectron peaks, it is evident that very effective separation of spurious single electrons (thermionic, cold discharge, and others) and the desired multielectron signals can be achieved. The C31024 has shown resolution of four distinct electron peaks.[12]

Dark-Noise Measurements

For each electron emitted from the photocathode of a PMT, a charge pulse of magnitude *Ge* appears at the anode, where *G* is the multiplier gain and *e* is the basic electronic charge (this is the basis of photon counting or, more properly, photoelectron counting). Because PMT noise originates at the photocathode in the form of dark emission, a useful figure of merit is the dark-count rate of the PMT as measured at the anode. The dark-count rate of a PMT is most readily measured with a multichannel pulse-height analyzer. The PMT is illuminated with weak dc light and the position of the single-electron peak is noted. The light is turned off and the dark-count rate is determined by integrating over (typically) the 1/8 electron-equivalent channel to 32 electron-equivalent channel. (The dark noise is predominantly single-electron in nature, but multiple-electron events are observed due to a number of different effects, one of which is cosmic-ray-induced Cerenkov light in the PMT glass).[13]

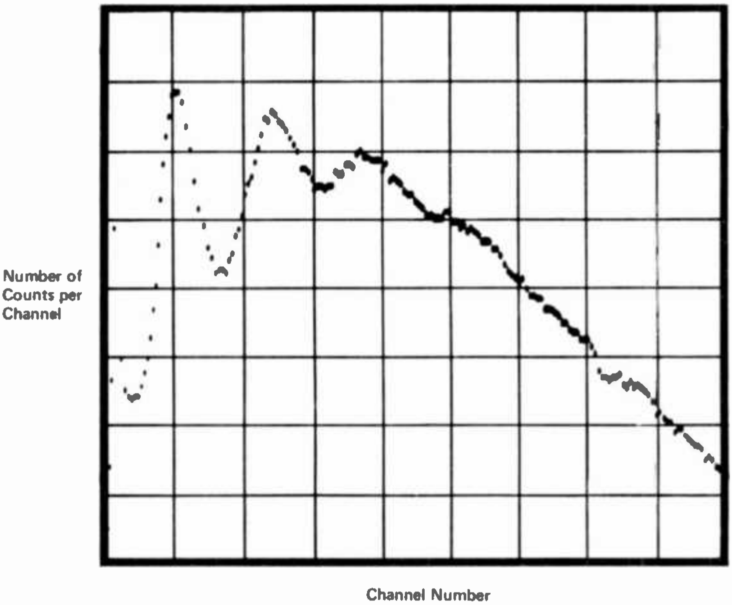

Fig. 5—Multichannel analyzer display of C31024 PMT illustrating 1, 2, and 3 electron peaks.

Early C31024 PMT's had dark count rates as high as 10^5 counts per second. The photocathode used is a (blue-sensitive) bialkali that exhibits dark emission rates of the order of two electrons/cm^2-second at room temperature; thus the dark noise rate of 10^5 per second was anomalously high for the 20 cm^2 photocathode area. Investigations revealed that the high dark-noise rate was due to two effects: (1) regenerative light feedback from the anode region and (2) field-emission-related effects within the multiplier structure.

Light production in PMT's was measured and photographed for a conventional-dynode 12-stage PMT.[14] However, in a 5-stage PMT the optical attenuation between anode region and photocathode is orders of magnitude less than for a 12-stage PMT of similar geometry. By improving the optical attenuation and modifying the internal structure, the dark-count rate of C31024 PMT has been reduced to <400 per second, indicating that the noise is now due mainly to dark emission at the photocathode.

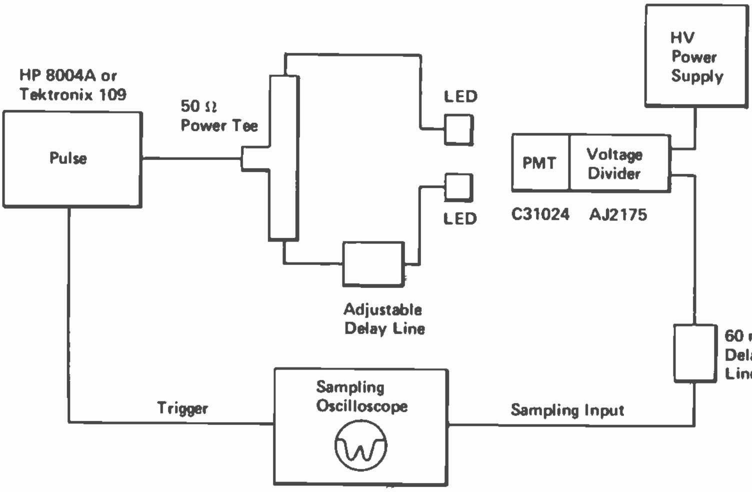

Fig. 6—Pulse-pair resolution instrumentation.

Pulse-Pair Resolution

A useful measure of the PMT's performance in fast timing or fast counting applications is pulse-pair resolution, i.e., the minimum time interval between two optical delta functions that can be resolved as distinct pulses at the anode of the PMT.[15] Measurement of pulse-pair resolution usually requires a mode-locked laser and optical splitter/delay apparatus, or else a double-pulse mode-locked laser. A simpler means for measuring pulse-pair resolution would be to employ a readily available pulser, two light-emitting diodes, and an adjustable delay line to vary the optical pulse spacing (See Fig. 6). The delay line is then adjusted to provide a 50%-above-baseline valley between the two pulses. The time can then be read directly from the oscilloscope display. The C31024 has a pulse resolution of 4 ns at a voltage of 3300 V when illuminating a 4-mm-diameter spot on the photocathode (See Fig. 7).

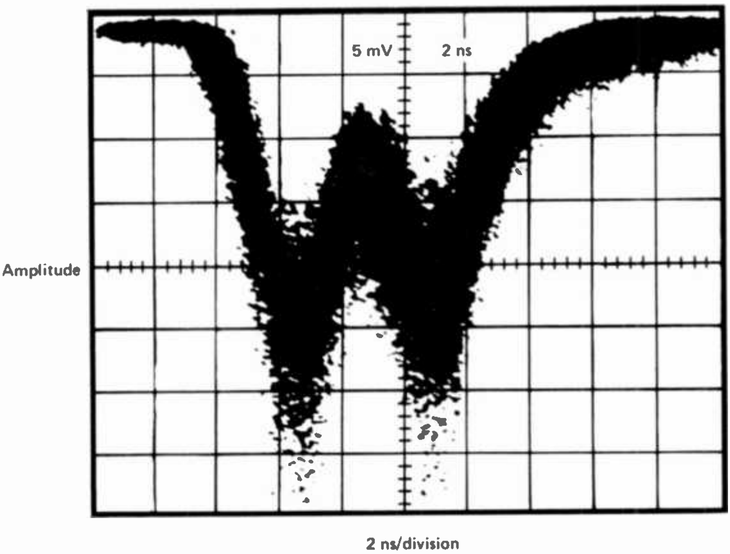

Fig. 7—Pulse-pair resolution of C31024 PMT.

This method is satisfactory for PMT's having rise times of 800 ps or greater, but the ~500 ps rise time of the Monsanto MV10A LED limits the usefulness of the technique in the case of faster PMT's. For IR-sensitive photocathodes, however, a pair of injection-laser diodes could probably be employed with good success.[16]

The pulser must be adjusted to provide pulse widths of a nanosecond or less and the light-emitting diodes must be driven to just slightly above threshold to ensure optimally narrow optical pulses.[17] The LED-to-PMT distance must be adjusted to yield equal-amplitude signals from each LED.

Single Electron Rise-Time Measurements

The fastest possible rise time of a PMT is the single-electron rise time.[15] By using single electrons liberated at the photocathode as the signal source, the need for a costly delta-function light source is eliminated.[5] The single-electron rise time for the developmental type C31024 PMT is 800 ps; the pulse form is shown in Fig. 8. Note the absence of ringing or other aberrations on the anode output pulse shown in Fig. 8.

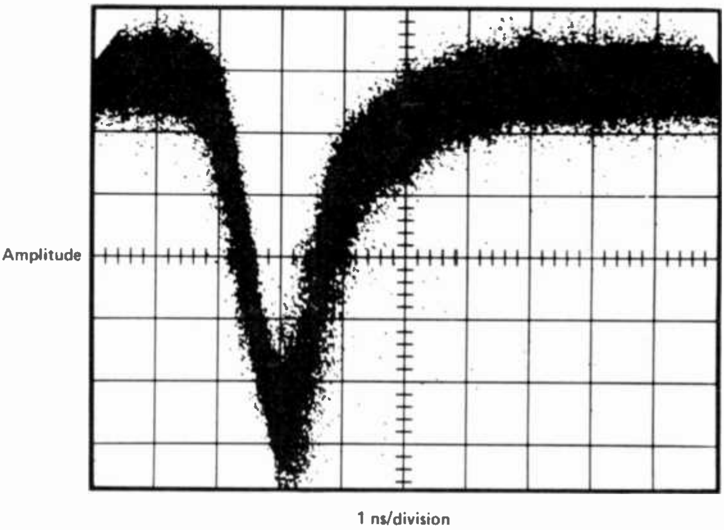

Fig. 8—Single-electron rise time of C31024 PMT.

Frequency-Domain Measurements

Historically, PMT time response has been defined and measured in terms of delta-function light excitation, resulting from one of the first applications of PMT's—that of scintillation counting. Today, PMT's are used to detect frequency-modulated laser signals and, therefore, frequency-domain measurements are of considerable interest. Ideally, a sine-wave-modulated laser should be employed to measure the frequency response of the PMT. In lieu of this, the PMT can be illuminated with dc light and its output current analyzed on a spectrum analyzer. The rf spectrum of the C31024 output is shown in Fig. 9. It should be noted that with the PMT removed from the system, there is an inherent noise level associated with the input electronics, as indicated in the figure. The one-half-amplitude point in current is 250 MHz. In general, most PMT's to date have been designed to provide optimum response to optical delta-function signals and, therefore, are not necessarily optimized for flat frequency response.

Applications of the C31024 PMT

Fast photomultipliers are commonly used in laser ranging experiments. The single-electron time resolution (popularly called jitter) of the C31024 is of the order of 570 ps,[12] allowing distance resolution of the order of 6 cm for return signals that produce only one photoelectron.

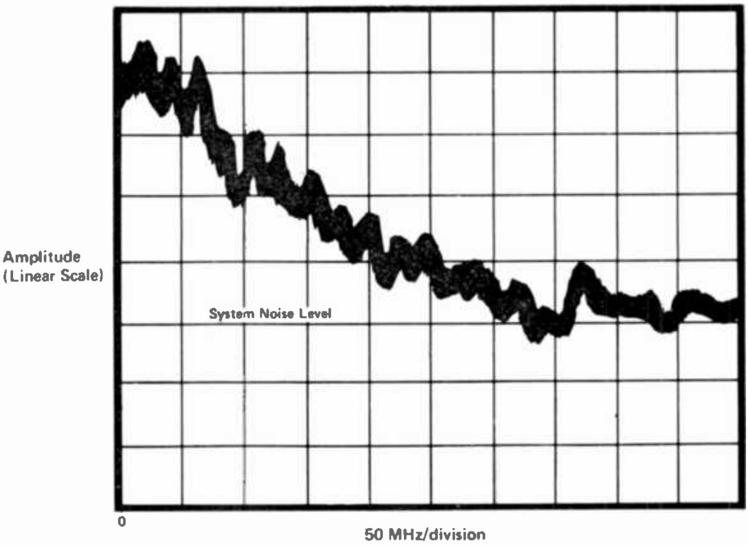

Fig. 9—Noise spectrum of C31024 PMT.

In the field of medical electronics, it is customary to employ a pair of PMT's in coincidence in liquid scintillation spectrometers used to determine extremely low activity levels of tritium and carbon. The use of NEA PMT's with GaP(Cs) dynodes allows better energy resolution between tritium and carbon samples. More important, however, is the potential for distinguishing between signal events and background events by employing pulse-shape discrimination.[18] This powerful technique could enhance the usefulness of liquid scintillation spectrometers used in medical applications. Similar applications of pulse-shape discrimination have, of course, been employed in the past on a slower time scale in NaI(Tl) scintillation counting experiments in physics.

In Raman spectroscopy, fluorescence of the sample often masks the Raman line, whose intensity is far less than that of the fluorescence. It has been suggested[19] that a pulsed laser and fast PMT can be employed to do fast photon counting of the Raman signal before the fluorescence intensity begins to obscure the Raman line. A fast PMT and linear gate could thus advantageously be used to enhance the signal-to-noise ratio in Raman Spectroscopy.

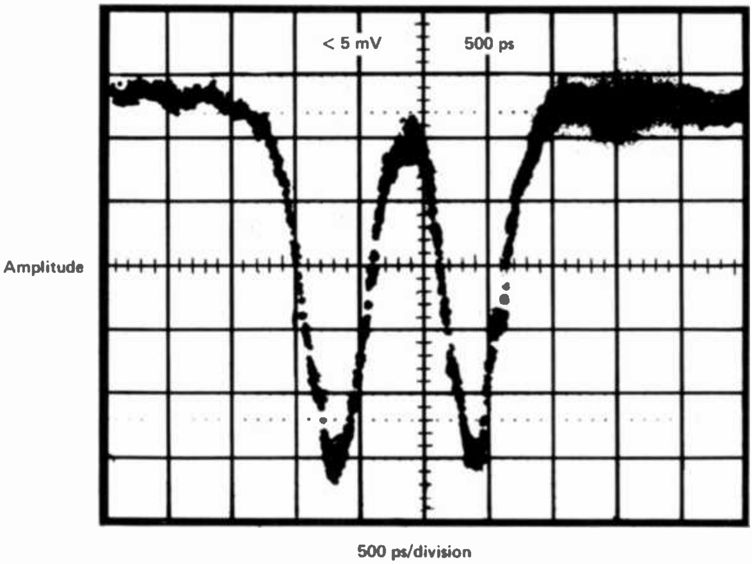

Fig. 10—Pulse-pair resolution of C31050 PMT excited by double-pulse argon laser.

Future Research

With the increased interest in faster PMT's, it has become evident that more research is required to improve methods of characterizing the performance of these fast PMT's. (Testing the rise time of the PMT when excited with a step-function light source rather than the more common delta-function light source can be considered as one example of such characterization.) Efforts are now under way to define meaningful tests for the specification of fast PMT's, as well as to provide state-of-the-art devices. At the same time, other fast NEA PMT's are also being researched. There are presently two devices in development. The first is the C34002, a 50-ps-rise-time photodiode utilizing an NEA cathode (either GaAsP or GaAs) for use with mode-locked lasers. The second is the C31050,* a three-stage PMT

---

* Development in part supported by Wright-Patterson Air Force Base, Contract F33615-71-C-1473, with the ADP/405B Space Data Relay/Laser Communications group.

having GaP(Cs) dynodes and a GaAsP photocathode, for use in optical communications. The C34002 is still in the design stages; Fig. 10 shows the response of the recently fabricated C31050 to a double-pulse argon laser.

Acknowledgement

The authors would like to thank J. L. Ibaugh and R. E. McHose for their assistance in collection of data on the C31024, and J. Heitman (Wright-Patterson Air Force Base) for his aid in evaluating the C31050.

References:

[1] R. E. Simon and B. F. Williams, "Secondary Electron Emission," **IEEE Trans. Nuclear Sc.**, Vol., NS-15, No. 3, p. 167, June 1968.

[2] N. R. Whetten and A. B. Laponsky, "Secondary Electron Emission of Single Crystals of MgO," **J. Appl. Phys.**, Vol. 28, p. 515, April 1957.

[3] H. E. Kulsrud, "A Programming System for Electron Optical Simulation," **RCA Rev.**, Vol. 28, No. 2, p. 351, June 1967.

[4] R. C. Miller and N. C. Wittwer, "Secondary Emission Amplification at Microwave Frequencies," **IEEE J. Quant. Elect.**, Vol. QE-1, No. 1, p. 49, April 1965.

[5] H. R. Krall and D. E. Persyk, **IEEE Trans. Nuclear Sc.**, Vol. NS-19, p. 45 (1972)

[6] B. F. Williams, **IEEE Trans. Nuclear Sc.**, Vol. NS-19, p. 39 (1972).

[7] R. Kollath, "Elektron Secundarelektronen-Emission fester Korper bei Vestrahlung mit Elektronen," **Handbuch der Physik**, ed. by S. Flugge, Springer-Verlag (1956) Vol. 21, pp. 232–303.

[8] I. A. D. Lewis and F. H. Wells, **Millimicrosecond Pulse Techniques**, 2nd. ed., Pergamon Press, New York (1959).

[9] Time Domain Reflectometry, Hewlett-Packard Application Note 62.

[10] Time Domain Reflectometry, Tektronix Publication 062–0703–00.

[11] G. A. Morton, H. M. Smith, and H. R. Krall, "Pulse Height Resolution of High-Gain First Dynode Photomultipliers," **Appl. Phys. Letters**, Vol. 13, p. 356, 15 Nov. 1968.

[12] B. Leskovar and C. C. Lo, **IEEE Trans. Nuclear Sc.**, Vol. NS-19, No. 3, p. 50 (1972).

[13] A. T. Young, "Cosmic Ray Induced Dark Current in Photomultipliers," **Rev Sci. Instr.**, Vol. 37, p. 1472, Nov. 1966.

[14] H. R. Krall, "Extraneous Light Emission from Photomultipliers," **IEEE Trans. Nuclear Sc.**, Vol. NS-14, No. 1, p. 455 (1967).

[15] IEEE Standard Test Procedures for Photomultiplier for Scintillation Counting and Glossary for Scintillation Counting Field, ANSI N429–1972, Sept. 20, 1972.

[16] E. Fischer, "Laser Diode as Source of Radiant Flux," RCA Application Note AN–4553.

[17] H. R. Krall, F. A. Helvy, and D. E. Persyk, "Recent Developments in GaP (Cs)–Dynode Photomultipliers," **IEEE Trans. Nuclear Sci.**, Vol. NS–17, No. 3, p. 71, June 1970.

[18] D. L. Horrocks, "Pulse Shape Discrimination with Organic Liquid Scintillator Solutions," **Appl. Spectroscopy**, Vol. 24, No. 4, p. 397 (1970).

[19] P. R. Reed, private communication.

Epitaxial Growth of Silicon Using Dichlorosilane: Growth on Single-Crystal Hemispheres

N. Goldsmith and P. H. Robinson
RCA Laboratories, Princeton, N.J.

Abstract—Dichlorosilane has been used to deposit silicon on single-crystal silicon substrates and hemispheres. The growth rate using single-crystal substrates was found to be orientation independent, unlike results reported for silicon tetrachloride. The growth morphology on the major low-index planes using hemispheres is significantly different, and was found to be dependent on surface preparation. The growth rate on the hemispheres seemed to be controlled mainly by the geometry of the sample, the fastest growth occurring at the apex of the hemisphere. This observation is explained in terms of a simple boundary-layer model.

Introduction

In a recent series of papers it has been shown that the reduction of dichlorosilane (SiH_2Cl_2) in hydrogen at elevated temperatures can be used for the epitaxial deposition of silicon on silicon.[1-3] Among the attractive features of this method for the growth of epitaxial silicon films is the relative ease of obtaining high growth rates and an in-sensitivity of the rate to changes in growth temperature. Our preliminary experiments using oriented single-crystal wafers showed that the growth rate was not orientation dependent, in contrast to results reported in which other members of the chlorosilane series were used as the source. We observed, however, that there were important differences in the morphology of the surfaces that were obtained on the various crystallographic orientations. In order to study the growth morphology in more detail, we have deposited layers of silicon on oriented single-crystal hemispheres of silicon.

Experimental

All of the work described in this paper was carried out in a commercially available expitaxial reactor of the "pancake" design in which there is no large lateral component of the gas flow past the growing surface. This minimizes considerations of circumferential asymmetric flow past the growing hemispheres, as shown later. The wafers or hemispheres were placed on a 5-inch-diameter silicon-carbide-coated graphite susceptor that is heated by r-f induction and rotates at 15 rpm while the layers are growing. The gases are contained within a 6-in-diameter quartz bell jar, with the gases fed upward through a central column. Hydrogen was obtained from a Pd-Ag diffusion cell, doping gases were arsine or diborane diluted with hydrogen, and dichlorosilane was metered as a gas directly from the cylinder. Temperatures were read using an optical pyrometer of the disappearing-filament type and are not corrected for emissivity or for absorption losses due to the quartz bell jar.

Single-crystal hemispheres of high-resistivity silicon were prepared by grinding from rods in a manner similar to that described by Gualtieri et al.[4] The hemipsheres were 10 mm in diameter and were oriented so that the base of the hemisphere was within 1° of the (100) or (111) plane. Depositions were carried out on hemispheres that were left with the lapped surface as well as on hemispheres that were chemically polished. Chemical polishing was accomplished using either nitric/hydrofluoric acid mixtures or by vapor etching with HCl. Heavily doped control wafers of the same conductivity type as the hemispheres were included with each run as a check on the previously determined growth rate of the system. The grown layers were doped to produce layers of opposite conductivity type with a doping density of approximately 1×10^{16} cm^{-3}. The reactor conditions were chosen such that the deposition rate on the control wafers was 1.7 μm/min.

The temperature at the top of the hemisphere was approximately 70°C cooler than the hemisphere–susceptor interface. For the temperature range used in these experiments, no significant difference in growth rate is observed in this system on control wafers for such a 70° change. One hour growth times, at a susceptor temperature of 1130°C, were used for all samples with the exception of those that were HCl polished. In the latter case, the growth time was 30 minutes at 1180°C. The HCl-etched hemispheres did show some degree of faceting prior to growth, although HCl etching of hemispheres has been reported to be non-preferential.[4] For the etching experiments, an HCl concentration of 1% in hydrogen[5] was used. A control wafer with a 100-μm-thick expitaxial layer was reduced in thickness by 25 μm after 30 minutes of etching. In all cases, the hemispheres were held at the deposition temperature for 15 minutes before growth was started and then were HCl etched so as to remove approximately 1 μm from the surface. Thickness measurements on the control wafers were obtained from the infrared interference reflection spectrum. The layer thickness on the hemispheres was determined by sectioning and polishing, followed by copper staining to delineate the grown junction. The stained cross section was accurately aligned on a rotating substage in such a way that the epitaxial interface could be rotated directly beneath the microscope objective without stage translation. The angular measurements are estimated to be correct within ± 2°. Thickness measurements on the hemispheres are estimated to be correct to within ± 5 μm.

Crystallinity of the growth was determined from Laue back-reflection x-ray patterns at various positions on the surface of the hemisphere. Photomicrographs of the surface morphology were obtained by fastening the sample onto a stage that could be rotated about an axis parallel to the plane of observation so as to place the point of interest perpendicular to the viewing axis of the microscope.

Results

Photographs of the as-grown hemispheres are shown in Fig. 1(a) to 1(d). The growth morphology on the nitric/hydrofluoric acid polished surfaces was essentially the same as that on the lapped surfaces and so are not shown. The growth on the HCl etched surfaces was distinctly different as can be seen by comparing Figs. 1(a) and 1(c). Although the deposition on the HCl etched sample took place at a higher temperature than those on the lapped surfaces, this factor is not considered to be significant in terms of the present experiments.

Laue patterns taken on the smooth areas show that these are indeed single-crystal regions. The rough areas, such as those marked A on Fig. 1(b) are polycrystalline. The Laue pattern taken at the apex of this hemisphere with the base oriented to the (100) plane, Fig. 2(a), was found to be twinned about the (111) plane producing a (210) pattern. The gowth on the (111) plane of both spheres was decidedly polcycrystalline. The Laue pattern shown in Fig. 2(b) was taken approximately 5° off the (111) in the direction of the (110), that is along the band of smooth growth marked B in Fig. 1(b). This pattern corresponds to that of single-crystal material. A similar result is obtained when the sphere is cut so that the (111) plane is at the

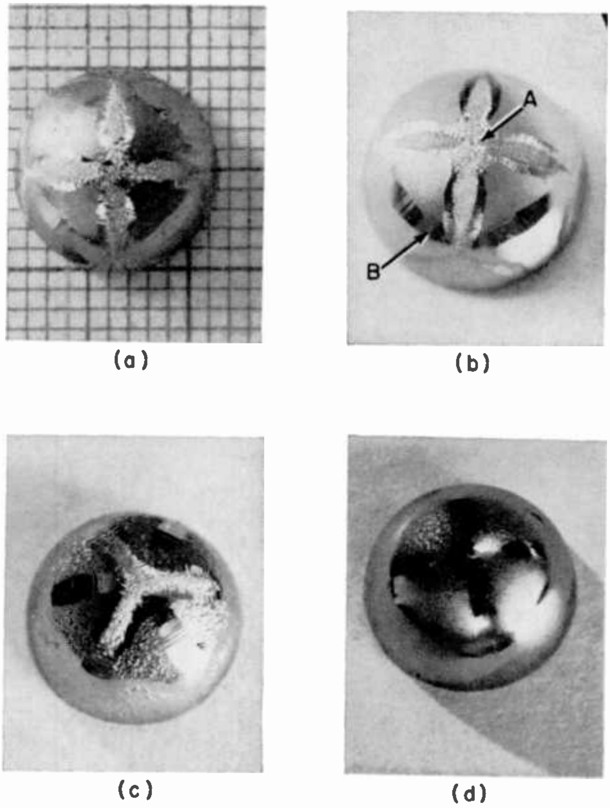

(a) (b)

(c) (d)

Fig. 1—Photographs of surfaces of hemispheres after deposition on lapped surfaces (a), (b), and (c), and on HCl etched surface (d). Photographs (b), (c), and (d) are taken 23° from the normal. Photograph (a) is taken normal to the back plane against a 1-mm grid. Hemisphere (c) has a back plane orientation of (111), all others are (100).

apex. In this case, however, the three smooth growing, single-crystal regions project toward (100) planes instead of toward (110) planes. However, as the (110) plane is reached, there is a broad region of very flat single-crystal growth.

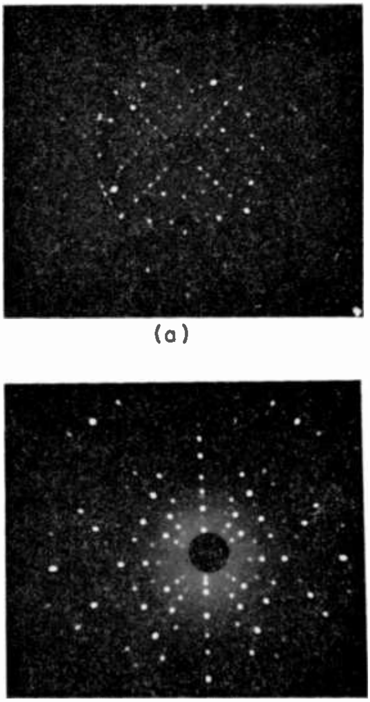

(a)

(b)

Fig. 2—Laue patterns of growth on sphere shown in Fig. 1(a). Photograph (a) taken at apex hemisphere and photograph (b) 5° off (111) toward nearest (110).

Figs. 3(a) to 3(f) are photomicrographs of the growth on the major planes of a hemisphere whose base was oriented to the (100). The photographs are shown in pairs, with the growth on the lapped surfaces in the left column and the growth on the HCl etched surfaces in the right column. All of the photographs were taken at an original magnification of × 68, which corresponds to an included field of view of approximately 10° from the central plane. The sequence in each column is (100), (111), (110). The original surfaces, photographed at the same magnification, are shown in Figs. 4(a) to 4(d).

It is apparent from the photographs that there is a consistent

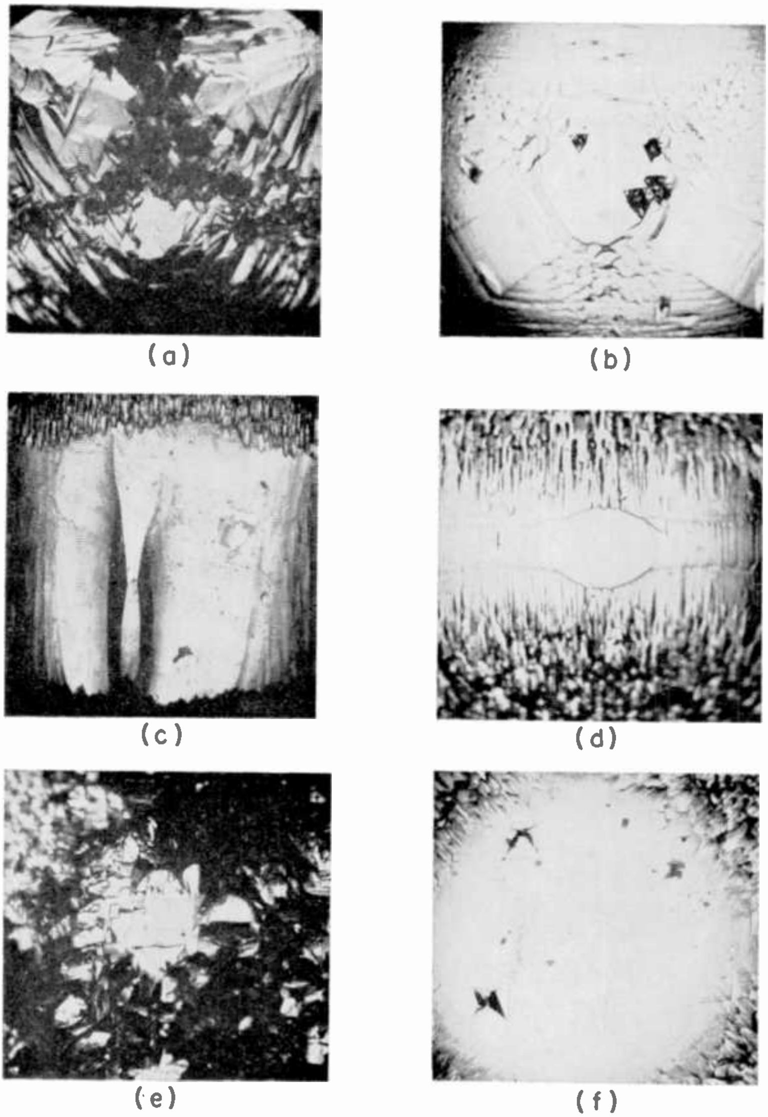

(a) (b) (c) (d) (e) (f)

Fig. 3—Photomicrographs of as-grown surfaces on the three major planes. Original magnification is ×68, corresponding to an included field of view of approximately 10° from the central plane. Photographs in the left column are growths on lapped surfaces; those in the right column, growths on HCl etched surfaces. Orientations are (111), (a) and (b); (110), (c) and (d); (100), (e) and (f). All growths were on hemispheres having a (100) back plane.

tendency to obtain very smooth single-crystal growth on or near the (110) plane in all cases. It is well known that for epitaxial growth the substrate should be oriented several degrees off the major plane if smooth, unfaceted growth is to be obtained.[6] From Fig. 3(a) it can be argued that the tilt should be approximately 4° off the (111) plane toward the nearest (110), which is the direction of tilt curently used for epitaxial substrates in conjunction with epitaxial deposition from silicon tetrachloride. The degree of tilt is greater than that currently used. This is in agreement with studies on pattern washout in integrated circuits, where a tilt of 3.5° is suggested.[6,7] Contadictory evidence is obtained from Fig. 1(c), where the direction of tilt would have to be toward the (100), since the growth toward the (110) is

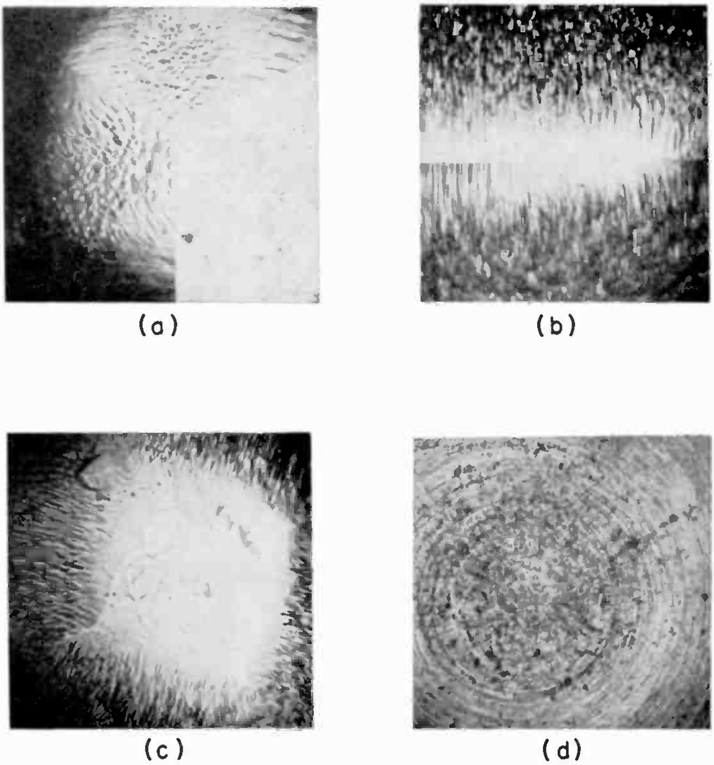
(a) (b)
(c) (d)

Fig. 4—Photomicrographs of surfaces before growth, at the same magnification as Fig. 3. Photographs (a), (b), and (c) are (111), (110), and (100) surfaces, respectively, on the surface of a hemisphere oriented to a (100) back plane after HCl etching. Photograph (d) is the unetched surface.

polycrystalline. These data are, of course, influenced by the fact that the growth on the (111) plane of the two hemipsheres took place at different temperatures and with the growth plane at a different angle to the gas stream. The first case more nearly approximates the growth in a standard horizontal reactor.

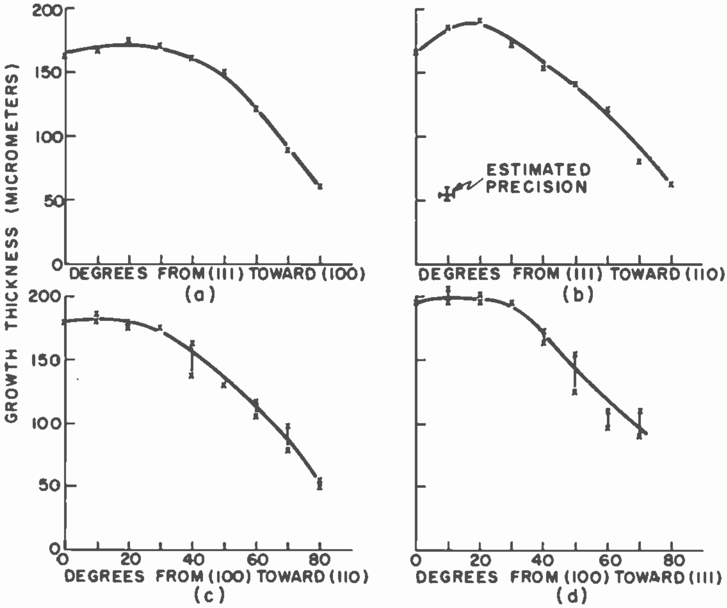

Fig. 5—Thickness versus angle from the apex of the hemisphere for depositions on unetched surfaces, using hemispheres with a back plane corresponding to a (100) plane, (a) and (c), and a hemiphere with a (111) back plane, (b) and (d).

The data on thickness versus angle from the central plane for the lapped samples are plotted in Figs. 5(a) to 5(d). From these curves, it can be seen that the growth decreases in thickness from the upper surface of the sphere toward the equator, so that under these deposition conditions, the rate is not principally controlled by the orientation of the substrate. The data for the four curves were obtained from three different samples. A hemisphere oriented with its back plane a (100) surface can be cut so that the section passes through two (111) or two (110) planes located on opposite sides of the hemisphere. The error bars in Figs. 5(c) and 5(d) indicate the maximum and minimum values obtained on either side of the hemisphere. A hemisphere that has its back plane oriented to the (111) can be cut in half so that the section is directed toward a (110) plane on one side and a (100) plane on the other side. The data on the (111) hemisphere were taken this way, so that only single values for the thickness are reported. A typical stained section through the apex of the (111) hemisphere is shown in Fig. 6. Although the growth appears to have been single crystal in the initial stages, it is clearly polycrystalline throughout the majority of the deposit.

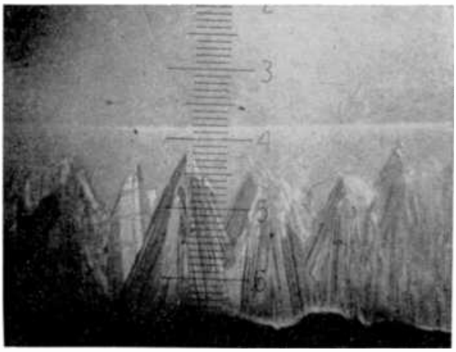

Fig. 6—Polished and stained section through apex of hemisphere oriented to (111) back plane. Each division of superimposed scale corresponds to 7μm. The substrate is the upper portion of this photograph.

Using both lapped and polished surfaces, the regions of smoothest growth were, in general, along the zones that connect the three major low-index planes. Using lapped surfaces, single-crystal growth was never obtained on (111) planes, while single-crystal growth was obtained for growth on the (100) and (110) planes. From comparison with the results obtained using HCl etched spheres, it is apparent that the morphology of growth has reproduced the preferential etching of the hemisphere so that the angular deviations and directions in which the smoothest growth is obtained are a reflection of the initial conditions of the hemisphere. This is borne out by the experiments in which the sphere was polished using nitric/hydrofluoric acid prior to growth. In this case, the results were essentially the same as growing on lapped surfaces. It is not possible to compare our HCl etching results with those of Gualtieri et al,[4] as they ran their experiments in nitrogen at unspecified values of temperature and HCl concentration. Our surface preparation is similar, however, to that reported by them.

As was anticipated from the preliminary results on single-crystal wafers, the growth rate on the surface of a hemispherical single crystal was not controlled by the crystallographic orientation. The total thickness from the top of the hemisphere to the bottom varies by a factor of three, being thicker at the top in all cases, even though several areas of the surface are polycrystalline. It is apparent, therefore that the hemispherical shape of the sample itself is the most important factor in determining the shape of the thickness versus angle curves. Were the orientation of the substrate the controlling factor, the thickness curves directed from (100) to (111), for example, would be the same whether or not the (100) or the (111) plane was at the top or side of the hemisphere. This is not the case as can be seen from a comparison of Figs. 5(a) and 5(d). The temperature gradient across the sample is, of course, in the wrong direction to account for the thickness curves, since the thickest growth was obtained on the coolest portions of the hemisphere. The oriented single-crystal wafers that were used as controls during the deposition of the hemispheres had an average layer thickness of 106 μm, in agreement with the previously determined deposition rate for this system.

A possible explanation for the observed thickness results involves an argument similar to that advanced by Green[8] to explain fast-growing protrusions from epitaxial surfaces. Basic to this argument is the concept of diffusion of the reactants to the growing surface through a stagnant boundary layer as the rate-limiting step in the growth process. The reactant concentration in the boundary layer is taken, as a first approximation, as decreasing linearly from the outer edge of the boundary layer toward the growing surface.[9] Thus a deposition site that projects into the boundary layer will see a higher concentration of reactants, and so grow faster, than one at the bottom of the boundary layer. Several workers have attempted to measure the boundary layer thickness[9,10] and have concluded that, even under conditions of high gas velocity, which tend to reduce the boundary layer thickness, boundary layers in typical reactors are on the order of 5 mm. In the case of our experiments, the hemispheres project 5 mm above the susceptor surface, and thus may not only grow faster because of the higher local concentration of reactants, but also serve to strip reactants from the boundary layer so that the growth rate at the base of the hemisphere is lower than that found on control wafers lying in the plane of the susceptor. A similar effect has been noted in the case of fast growing protusions on epitaxial silicon wafers, where a distinct depression is found surrounding the base of the protrusion[11].

Acknowledgments

The authors wish to thank R. Smith for the Laue back reflection analyses, P. Messineo for the sectioning work, and J. Jaklik and R. Wance for their technical assistance.

References:

[1] W. C. Benzing, A. E. Ozias, I. M. Helmer, "The Rate of Epitaxial Film Growth from Dichlorosilane," Applied Materials Inc., Technical Report.

[2] W. C. Benzing, A. E. Ozias, H. B. Bradley, "Dichlorosilane: A New Approach to Epitaxial Silicon," Extended Abstracts of the Spring 1971 Meeting of the Electrochemical Society, p. 184.

[3] M. Van Hoy, "Dichlorosilane Epitaxial Layers for Integrated Circuits," 71st National Meeting of the American Institute of Chemical Engineers, Feb. 20-23, 1972.

[4] J. G. Gualtieri, M. J. Katz, and G. A. Wolff, "Gas Etching and its Effect on Semiconductor Surfaces," **Z. Kristall.**, Vol. 114, p. 6 (1960).

[5] G. A. Lang and T. Stavish, "Chemical Polishing of Silicon with Anhydrous Hydrogen Chloride," **RCA Review,** Vol. 24, No. 4, p. 488 (1963).

[6] S. K. Tung, "The Effects of Substrate Orientation on Epitaxial Growth," **J. Electrochem. Soc.,** Vol. 112, No. 4, p. 436 (1965).

[7] D. C. Gupta, "Improved Methods of Depositing Vapor-Phase Homoepitaxial Silicon," **Solid State Tech.,** Vol. 4, No. 10, p. 33 (1971).

[8] J. M. Green, "Fast Growing Protrusions from Epitaxial Semiconductor Surfaces," **Metallurgical Trans.,** Vol. 1, p. 648 (1970).

[9] F. C. Eversteyn, P. J. W. Severin, C. H. J. v. d. Brekel, and H. L. Peek, "A Stagnant Layer Model for the Epitaxial Growth of Silicon from Silane in a Horizontal Reactor," **J. Electrochem. Soc.,** Vol. 117, No. 7, p. 925 (1970).

[10] R. Takahashi, K. Sugawara, Y. Nakazawa and Y. Koga, "Convective Mass-Transfer Analyses of Silicon Epitaxial Deposition, Part 1. Observation of Gas Flow Patterns in Reactors," **Proc. Second International Conf. on Chemical Vapor Deposition,** Los Angeles, Calif., May 10-15, 1970, p. 695.

[11] P. H. Robinson, unpublished results.

A Room-Temperature Non-Indium Metallic Bond Tested by Welding Acoustic Shear-Wave Transducers to Paratellurite

J. D. Knox

RCA Laboratories, Princeton, N. J.

Abstract—A room-temperature metallic bonding process used to weld ultrasonic transducers without the need for indium has been developed for ultrasonic device applications. The bond has been tested by welding shear-wave transducers to anisotropic paratellurite for light-deflection applications. The rf frequency was 100 MHz and under; however, there is positive indication that this bond can extend the useful operating frequency to the microwave range.

Introduction

A room-temperature metallic bonding technique aimed at eliminating the lossy rf indium layer has been developed and successfully tested by welding shear wave $LiNbO_3$ transducers to paratellurite (TeO_2) for light-deflection applications. The bonds are made by evaporating thin films of chrome, aluminum, and gold to optically polished surfaces and then welding the films by compression. The performance figures for the bonding technique reported in this note involve acoustic frequencies less than 100 MHz. However, with the indium layer eliminated, there is clear indication* that efficient operating frequencies can be extended to the microwave range.

---

* A collaborative effort is underway between the author and H. Huang and Z. Turski to utilize this welding technique to fabricate acoustic microwave delay lines. Preliminary results indicate that acoustic transducers bonded with this method can operate efficiently up to 5 GHz. The details of this work will be published shortly. We are optimistic that the operating frequency can be extended to 10 GHz.

Results

The bonding process is similar to the cold indium weld[1] except that the indium control layer is eliminated. The two crystals, or materials to be bonded, are processed by having their respective contact faces optically polished to a quarter-wave flatness or better and vacuum deposited with a metallic combination of chrome, aluminum, and gold.

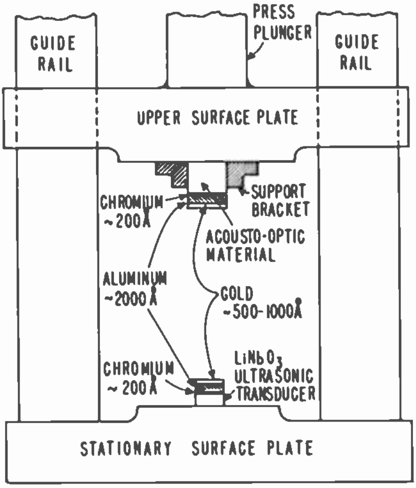

Fig. 1—Press arrangement. Acousto-optic material is bonded to the ultrasonic transducer when the metallic films are brought into contact and compressed in vacuum.

A flash of chrome (~ 200 Å) followed by a relatively thick aluminum layer (~ 2000 Å) and a thin layer of gold (500-1000 Å) provides a sandwiched control-layer thickness of about one-half micron. The chrome is used as an adhesion layer to assure that the aluminum and gold will adhere to the crystals. The two metallized surfaces are brought into contact in vacuum and compressed together (see Fig. 1). The relatively thick layer of aluminum provides padding that enables the two crystals to mesh together making uniform contact and resulting in a homogeneous bond. During a press time of approximately 60 minutes, the freshly deposited gold layers fuse together forming a weld under a moderate compression of 1200 psi.†

---

† It may be desirable to replace the aluminum layers with gold, making an all gold bond, in order to achieve a more favorable acoustic impedance match between the bonded crystals. This can be accomplished by depositing 2000 Å of gold onto each contact surface; however, it has been found that the compression should be extended to 2500 psi to achieve a strong weld.

The performance of this bond has been tested by welding $LiNbO_3$ shear-wave transducers to the 110 face of paratellurite. The transducers were thinned to the appropriate resonant frequency and the paratellurite was used as an anisotropic Bragg deflector.[2] The deflection efficiency versus rf input power, at a constant drive frequency of 80 MHz, is shown in Fig. 2. With an interaction length of 0.225 cm, about

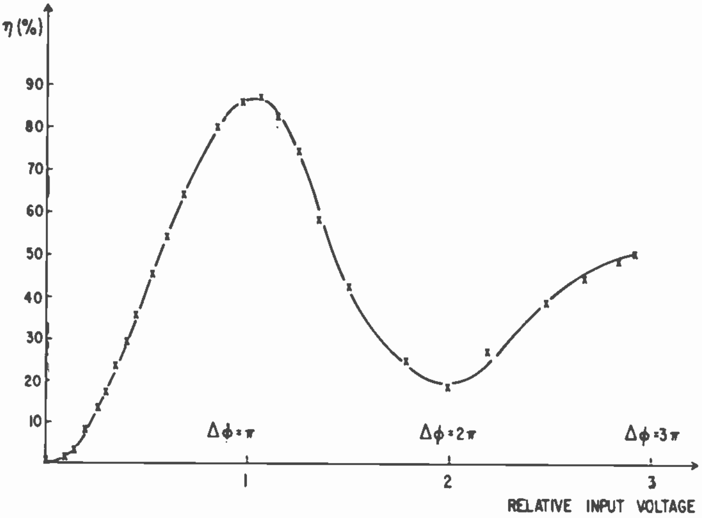

Fig. 2—Deflection efficiency versus rf drive power at a constant drive frequency of 80 MHz. As shown, the deflection efficiency could be driven past two maxima, indicating a total phase shift of 3π. A peak deflection efficiency of 87% was achieved with 70 milliwatts of rf drive power.

70 milliwatts of rf drive power was required to deflect 87% of the incident light (circularly polarized 4880 Å). These measurements indicate that the bond loss is about 3 dB. This deflector has been incorporated in a television-rate laser scanner[2] as the horizontal deflector, and the bond has shown no signs of fatigue after almost one year of heavy use.

Conclusion

Since the indium lyer has been eliminated from cold-weld metallic bonds, we now anticipate extending the useful acoustic operating frequency of such bonds to the microwave region. Without indium, the reduced bond losses* will result in less heat dissipation, allowing the acoustic device to be driven harder without over-heating and subsequent damage.

---

* This bonding procedure has also been used to weld longitudinal wave transducer to amorphous materials such as fused quartz and high index glasses as well as other single-crystal materials for modulation and cavity dumping applications. Preliminary measurements indicate the bond losses to be more reflective than heat dissipative.

References:

[1] E. K. Sittig and H. D. Cook, "A Method for Preparing and Bonding Ultrasonic Transducers Used in High Frequency Digital Delay Lines," **Proc. IEEE,** Vol. 56, pp. 1375-6 (1968).
[2] I. Gorog, J. D. Knox, P. V. Goedertier, and I. Shidlovsky, "A Television Rate Laser Scanner, II. Recent Developments," **RCA Review,** Vol. 33, No. 4, p. 667, Dec. 1972.

Recent Papers by RCA Authors

Listing is alphabetical by name of publication. For copies of reprints, the reader should contact the publication directly.

S. Larach and R. E. Shrader, "Cathode-Ray Excited Emission Spectrometry of Trace Rare Earths in Yttrium Oxide Via Yttrium Oxysulfide Conversion," **Analytica Chimica Act.**, Vol. 63, p. 459, 1973

H. Kressel and I. Ladany, "Photocurrent Measurements on GaP:N Green Light Emitting Diodes," **Applied Physics Lett.**, Vol. 22, p. 224, March 1, 1973

M. Ettenberg, H. Kressel, and S. L. Gilbert, "Minority Carrier Diffusion Length and Recombination Lifetime in GaAs:Ge Prepared by Liquid-Phase Epitaxy," **Applied Physics, J. of**, Vol. 44, p. 827, Feb. 1973

A. C. Ipri and J. N. Zemel, "Impurity Centers in Silicon Films on Sapphire," **Applied Physics, J. of**, Vol. 44, p. 744, Feb. 1973

A. Rothwarf, "Plasmon Theory of Electron–Hole Pair Production: Efficiency of Cathode-Ray Phosphors," **Applied Physics, J. of**, Vol. 44, p. 752, Feb. 1973

H. S. Somers, Jr., "Experimental Properties of Injection Lasers: Modal Distribution of Laser Power," **Applied Physics, J. of**, Vol. 44, p. 1263, March 1973

R. Williams and M. H. Woods, "High Electric Fields in Silicon Dioxide Produced by Corona Charging," **Applied Physics, J. of**, Vol. 44, p. 1026, March 1973

W. M. Yim, E. J. Stofko, P. J. Zanzucchi, J. I. Pankove, M. Ettenberg, and S. L. Gilbert, "Epitaxially Grown AIN and Its Optical Band Gap," **Applied Physics, J. of**, Vol. 44, p. 292, Jan. 1973

J. A. Castellano and G. H. Brown, "Thermotropic Liquid Crystals," **Chemical Technology**, Vol. 3, p. 47, Jan. 1973

W. M. Yim, A. K. Fan, E. J. Stofko, "Preparation and Properties of II-Ln$_2$-S$_4$ Ternary Sulfides," **Electrochem. Soc., J. of**, Vol. 120, p. 441, March 1973

B. R. Schwartz, "Interconnections," **Electromechanical Design**, March 1973

M. T. Duffy, C. C. Wang, G. D. O'Clock, Jr., S. H. McFarlane III, and P. J. Zanzucchi, "Epitaxial Growth and Piezoelectric Properties of AIN, GaN, GaAs on Sapphire or Spinel," **Electronic Materials, J. of**, Vol. 2, p. 359, 1973

R. Feryska, J. O. Preisig, and E. D. Menkes, "COS/MOS Phase Comparator," 1973 **IEEE Intl. Solid-State Circuits Conf. Proc.**, p. 184

M. S. Corrington, "Design of Two-Dimensional Recursive Filters," **IEEE, '73 Intl. Symp. on Circuit Theory**, April 1973

H. Urkowitz, "The Effect of Limiting Upon the Mean Cross Section of Lognormal Radar Clutter," **IEEE Trans. Aerospace and Electronic Systems**, March 1973

A. Waksberg, "FM Laser Noise Effects on Optical Doppler Radar Systems," **IEEE Trans. Aerospace and Electronic Systems**, Vol. AES-8, No. 6, Nov. 1972

C. V. Greenman, "A Simple Analytical Mode for the Envelope Distribution of Sinusoidal Carrier in Atmospheric Radio Noise," **IEEE Trans. Comm. Technology**, Vol. COM-21, p. 254, March 1973

D. Hampel, "Design of Multi-Function Threshold Gates," **IEEE Trans. Computers**, March 1973

K. Arai, O. Kubo, N. Tsuya, F. Okamoto, and P. K. Baltzer, "Ferromagnetic Resonance of Chromium Chalcogenide Ferro-Spinels," **IEEE Trans. Magnetics**, Vol. MAG-8, p. 479, Sept. 1972

P. Bura, "MIC Ku Band Upconverter," **IEEE Trans. Microwave Theory and Techniques,** March 1973

K Sadashige, "Selected Topics on Modern Magnetic Video Recording Technology," **Proc. of the Inst. of Electronic & Radio Engineers Conf. on Video & Data Rec.,** Univ. of Birmingham, England, July 10, 1973

J. I. Pankove, E. A. Miller, and J. E. Berkeyheiser, "GaN Yellow-Light Emitting Diodes," **Luminescence, J. of,** Vol. 6, p. 54, Jan. 1973

F. J. Hughes, Jr., **Application of Optimal Control Techniques to a Dual-Spin Spacecraft Incorporating Flexible Appendages,** MIT Thesis for B.S./M.S. Degrees

R. Klein and R. K. Wehner, "Phonon-Phonon Collisions and Entropy Fluctuations in Dielectric Crystals," **Proc. Intl. Conf. on Phonon Scattering in Solids,** Paris, July 3-6, 1972, p. 18

H. Kiess and T. Freund, "Charge Transfer of Adsorbed Ozone," **Physical Chemistry, J. of,** Vol. 77, p. 556, Feb. 15, 1973

E. S. Sabisky and C. H. Anderson, "Verification of the Lifshitz Theory of the van der Waals Potential Using Liquid-Helium Films," **Phys. Rev. A,** Vol. 7, p. 790, Feb. 1973

H. Kressel, H. F. Lockwood, F. H. Nicoll, and M. Ettenberg, "Spontaneous and Stimulated Recombination in p^+–n–n^+ (AlGa)As-GaAs Heterojunction Laser Diodes," **Quantum Electronics, J. of,** Vol. QE-9, p. 383, Feb. 1973

J. E. Carnes and W. F. Kosonocky, "Sensitivity and Resolution of Charge-Coupled Imagers at Low Light Levels," **RCA Review,** Vol. 33, p. 607, Dec. 1972

L. S. Cosentino and L. S. Stewart, "A Membrane Page Composer," **RCA Review,** Vol. 34, p. 45, March 1973

R. E. Flory, "Applications of the Bivicon Tube," **RCA Review,** Vol. 34, p. 132, March 1973

E. C. Giaimo, Jr., "Magnetoelectric Printing," **RCA Review,** Vol. 34, p. 112, March 1973

I. Gorog, J. D. Knox, P. V. Goedertier, "A Television Rate Laser Scanner—I. General Considerations," **RCA Review,** Vol. 33, p. 623, Dec. 1972

I. Gorog, J. D. Knox, P. V. Goedertier, and I. Shidlovsky, "A Television Rate Laser Scanner—II. Recent Developments," **RCA Review,** Vol. 33, p. 667, Dec. 1972

E. O. Johnson, "The Insulated-Gate Field-Effect Transistor—A Bipolar Transistor in Disguise," **RCA Review,** Vol. 34, p. 80, March 1973

W. F. Kosonocky and J. E. Carnes, "Two-Phase Charge-Coupled Devices with Overlapping Polysilicon and Aluminum Gates," **RCA Review,** Vol. 34, p. 164, March 1973

S. Y. Narayan and J. P. Paczkowski, "Integral Heat Sink Transferred Electron Oscillators," **RCA Review,** Vol. 33, p. 752, Dec. 1972

A. Presser and E. F. Belohoubek, "1-2 GHz High-Power Linear Transistor Amplifier," **RCA Review,** Vol. 33, p. 737, Dec. 1972

A. Rosen, J. F. Reynolds, S. G. Liu, and G. E. Theriault, "Wideband Class-C Trapatt Amplifiers," **RCA Review,** Vol. 33, p. 729, Dec. 1972

A. H. Sommer, "Practical Use of III-V Compound Electron Emitters," **RCA Review,** Vol. 34, p. 95, March 1973

R. L. Spalding, S. A. Ochs, and E. Luedicke, "The Bivicon Camera Tube—A New Double Vidicon," **RCA Review,** Vol. 34, p. 121, March 1973

F. Sterzer, "Information Processing with Transferred-Electron Devices," **RCA Review,** Vol. 34, p. 152, March 1973

W. C. Stewart, R. S. Mezrich, L. S. Cosentino, E. M. Nagle, F. S. Wendt, and R. D. Lohman, "An Experimental Read-Write Holographic Memory," **RCA Review,** Vol. 34, p. 3, March 1973

J. P. Wittke, "Thin-Film Lasers," **RCA Review,** Vol. 33, p. 674, Dec. 1972

R. W. Bernal, "J–K' Bistable Multivibrator," RCA Technical Note No. 930

W. A. Clapp, "LSI Computer Design—SUMC/DV," **Proc. Solid-State Circuits Conf.,** Phila., PA, Feb. 14-16, 1973

A. Feller, "CMOS LSI Computer Fabrication—SUMC/DV," **Proc. Solid-State Circuits Conf.,** Phila., PA, Feb. 14-16, 1973

R. A. Sunshine and J. Assour, "Avalanche Breakdown Voltage of Multiple Epitaxial pn Junctions," **Solid State Electron.,** Vol. 16, p. 459, 1973

G. T. Tseng, "Constant and Variable Amplitude Limit Cycles in Dual-Spin Spacecraft," **Spacecraft and Rockets, J. of,** Nov. 1972

S. L. Corsover, "Color of Multispectral Recording on Black and White Film," **Proc. SPIE—Military Airborne Video Recording Seminar,** Dayton, OH, April 3-5, 1973

B. Goldstein, "LEED, Auger and Plasmon Studies of Negative Electron Affinity on Si Produced by the Adsorption of Cs and O," **Surface Science,** Vol. 35, p. 227, March 1973

J. D. Levine, "Structural and Electronic Model of Negative Electron Affinity on the Si/Cs/O Surface," **Surface Science,** Vol. 34, p. 90, Jan. 1, 1973

H. Kressel, "Liquid Phase Epitaxy—Techniques and Applications," **Vacuum Science and Tech., J. of,** Vol. 10, p. 262, Jan./Feb. 1973

W. M. Maxwell and H. H. Rickert, "A Wide-Band, Short-Backfire, UHF Antenna Array," 23rd Ann. USAF Antenna Symp. Rec.

Patents Issued to RCA Inventors

January

G. A. Alphonse Apparatus for Efficiently Converting Microwave Energy into Acoustic Energy (3,710,283)
A. Bernstein Mechanical Drive Mechanism with Programmable Output Function (3,712,700)
M. G. Brown, Jr., G. J. Guille, Jr., and G. E. Long, III Cathode-Ray Tube with Laminated Safety Panel and Separate Light-Attenuating Layer (3,708,622)
J. Craft Muting Circuit (3,714,583)
A. G. F. Dingwall and J. M. Jorgensen Circuit for Improving Operation of Semiconductor Memory (3,714,638)
J. Dresner and A. M. Goodman Organic Electroluminescent Cells Having a Tunnel Injection Cathode (3,710,167)
W. V. Fitzgerald, Jr. and P. C. Lemmon High Voltage and Width Regulation Circuit (3,711,738)
T. P. Fulton and H. Di Luca Encapsulated Magnetic Memory Element (3,713,886)
J. B. Gallager, Jr. Edge Connector (3,710,303)
E. C. Giaimo, Jr. Magneto-Electric Apparatus for Reproducing an Image on a Recording Element (3,712,733)
J. W. Ham and J. M. Poplin Alignment and Test Fixture Apparatus (3,714,572)
R. D. Kell Luminescent Screen Comprising Phosphor Cores Luminescent in First Color and Phosphor Coatings Luminescent in Second Color (3,714,490)
H. G. Kiess Pyroelectric Photoconductive Elements and Method of Charging Same (3,713,822)
R. A. Kryder Automatic Brightness Control for Image Intensifier Tube (3,711,720)
A. J. Leidich and M. E. Malchow High Frequency Power Transistor Support (3,710,202)
J. J. Maley Method for Preparing a Conductive Coating on a Glass Surface (3,713,884)
R. J. McIntyre and H. C. Sprigings Quadrant Photodiode (3,714,491)
G. J. Meslener Decoder for Delay Modulation Signals (3,713,140)
R. S. Myers Regulated Ignition System (3,709,206)
R. C. Palmer Velocity Adjusting System (3,711,641)
W. R. Peterson Overcurrent Protection Circuit for a Voltage Regulator (3,711,763)
R. E. Quinn Appartus for Etching of Thin Layers of Material by Ion Bombardment (3,708,418)
E. C. Ross Operation of Memory Array Employing Variable Threshold Transistors (3,713,111)
J. F. Schanne Article Identification Apparatus (3,708,655)
J. C. Schopp Web Position Detector Using Temperature Sensing Elements (3,711,001)
J. M. Shaw Semiconductor Device or Monolithic Integrated Circuit with Tungsten Interconnections (3,714,521)
A. H. Sommer Method of Making an Electron Emitter Device (3,712,700)
V. Stachejko High Power Microwave Switch Including a Plurality of Diodes and Conductive Rods (3,711,793)
G. W. Steudel Input Transient Protection for Complementary Insulated-Gate Field-Effect-Transistor Integrated-Circuit Device (3,712,995)
J. A. vanRaalte and V. Christiano Intelligence-Handling Device Having Means for Limiting Induced Electrostatic Potential (3,708,712)
H. H. Volmerange Flip-Flop and Hold Phase Detector (3,710,140)
J. H. Wharton Gama Correction Bandpass Amplifier Circuits (3,708,615)

February

J. K. Allen Service Switch Arrangement for Improved Interlace Performance (3,715,493)
H. Amemiya and S. A. Graf Circuit for Minimizing the Signal Currents Drawn by the Input Stage of an Amplifier (3,717,821)
T. V. Bolger Color Television Recorder-Reproducer System (3,716,663)
J. D. Callaghan and R. Kaysen Indoor Antenna or Similar Article (D226274)
W. V. Fitzgerald, Jr. High Voltage Protection Circuit (3,715,492)
H. E. Haynes Scanning System Which Includes Means for Controlling Picture Sampling Density (3,715,498)
R. C. Heuner and S. J. Niemiec Data Translating Circuit (3,716,723)
J. B. Lerch Threshold Gate Circuits Employing Field-Effect Transistors (3,715,603)
W. H. Liederbach Method of Manufacturing Thick-Film Hybrid Integrated Circuits (3,714,709)
R. S. Lynch and K. B. Ayache Nutation Damper (3,716,206)
L. S. Napoli and J. J. Hughes Method of Making Semiconductor Devices (3,716,429)
C. L. Olson, J. F. Monahan, and R. A. Dischert Video Signal Noise-Limiting Apparatus (3,715,477)
B. S. Perlman Paired Nonlinear Active Elements in a Waveguide Cavity Adapted to Support Orthogonal TE_{10} Mode Waves and TE_{01} Mode Waves (3,715,686)
D. L. Ross Photochromic Display and Storage Device and Method of Operation Thereof (3,715,212)
G. Schiess Transistor Deflection Circuits Utilizing a Class B, Push-Pull Output Stage (3,715,621)
G. K. Sendelweck High Voltage Hold-Down Circuit (3,715,464)
S. A. Steckler Dual Mode Automatic Frequency Controlled Oscillator System (3,715,499)
P. K. Weimer Radiation Sensing and Signal Transfer Circuits (3,715,485)
O. M. Woodward TM_{01} Mode Exciter and a Multimode Exciter Using Same (3,715,688)
H. G. Wright and R. A. Dischert Shuttering Appartus for Television Cameras (3,715,486)

March

W. H. Barkow, and J. Gross Deflection Yoke for Use with In-Line Electron Guns (3,721,930)
B. E. Berson and C. L. Upadhyayula Variable Delay Line Utilizing One Part Reflection Type Amplifier (3,721,924)
N. Feldstein and J. A. Weiner Electroless Copper Plating Solutions with Accelerated Plating Rates (3,720,525)
E. C. Giaimo, Jr. Method of Transferring Magnetic Toner Particles in an Image Configuration and Apparatus Therefor (3,721,553)
J. J. Gibson and D. W. Peterson Physically Small Combined Loop and Dipole All Channel Television Antenna System (3,721,990)
I. Gorog Optically-Scanned Liquid-Crystal Projection Display (3,723,651)
S. Gray, B. J. Levin, and D. J. Miller Electrically Variable Waveguide Phase Shifter Comprising a Slab of Semiconductive Material (3,721,923)
P.Haferl Waveform Generating Circuit (3,721,957)
W. F. Kosonocky Charge Coupled Memory (3,720,922)
H. B. Law Fabrication of Focus Grill Type Cathode Ray Tubes (3,722,044)
A. Rosen and J. F. Reynolds Negative Resistance Semiconductor Coupled Transmission Line Apparatus (3,721,918)
E. C. Ross Memory System Using Variable Threshold Transistors (3,720,925)
L. N. Schiff and H. Staras Disabled Vehicle Signalling System (3,721,955)
J. C. Sondermeyer Load Sensing Circuits (3,721,889)
R. R. Steitz Method of Joining Solder Balls to Solder Bumps (3,719,981)
J. F. Sterner and G. D. Hanchett Dual-Gate MOS-FET Oscillator Circuit with Amplitude Stabilization (3,723,905)
J. H. Wharton Electromagnetic Focusing and Deflection Assembly for Cathode Ray Tubes (3,721,931)
C. F. Wheatley, Jr. Heat Sinking of Semiconductor Integrated Circuit Devices (3,723,833)

AUTHORS

Delbert D. Crawshaw received the M.S. Degree in Physics from Franklin and Marshall College in 1970. He joined the Phototube Product Development Group, RCA Electronic Components, Lancaster the same year, and has since been active in the fields of electron optical simulation techniques and III-V compound photocathode activation techniques. He has designed several metal–ceramic GaAs photodiodes for both spectroscopic and fast laser pulse measurements. Recently he has concentrated his efforts in the field of GaAs reflection-mode photocathode activation. He is currently studying activation techniques leading to very high quantum efficiencies in GaAs and GaInAs photocathodes.

A. F. Denny, a native of Great Britain, received his B.Sc. in chemistry from Liverpool University in 1958 and his Ph.D. in physical chemistry from Imperial College in 1962. He came to the United States in 1966 to work for the General Electric Company at Syracuse, N. Y. In 1970, he joined the RCA Solid-State Division at Somerville, N. J., to work on liquid-crystal display systems. Dr. Denny's research interests have been surface chemistry and adsorption, water chemistry, television systems, coal research, and liquid crystals. Currently, he is employed by Hamlin, Inc., in the manufacture of liquid crystal devices.

Gordon L. Fredendall received the B.S., M.S. and Ph.D. degrees from the University of Wisconsin in 1931, 1932, and 1936, respectively. His doctoral thesis was the culmination of an investigation of re-ignition in the mercury arc rectifier used in the electric power transmission industry. From his first employment in the research laboratory of RCA in 1936 until the present, he has made contributions in a broad field of television research including network theory, TV receivers and transmitters, cameras, tape recording, and large screen displays. In recognition of these contributions he has received five achievement awards from RCA Laboratories. He has also participated in AIEEE and NTSC television standards activity for many years.

He is a Fellow of the AIEEE and a member of Sigma Xi, Tau Beta Pi, and Eta Kappa Nu.

Norman Goldsmith received the B.A. degree with honors in Chemistry from Hunter College in 1959 and M.S. degree in Physical Chemistry from Stevens Institute of Technology in 1964. He joined RCA in 1959 working in the Solid-State Division at Somerville, N. J., on materials and process technology for silicon and gallium arsenide. His work in this capacity included epitaxial-growth materials purification, diffusion, vapor deposition, surface stabilization, clean oxide growth and the development of nondestructive measurement techniques. From 1967 to 1971 he was with Laser Diode Laboratories as executive vice president. He joined RCA Laboratories in 1971 where he is currently concerned with epitaxial growth studies for silicon power devices.

Mr. Goldsmith is a member of the American Chemical Society and the Electrochemical Society.

Joseph D. Knox received his B.S. degree in Electrical Engineering from the University of Dayton in Dayton, Ohio, in 1966 and his M.S. and Ph.D. degrees from Case Institute of Technology in Cleveland, Ohio, in January 1970 and September 1970, respectively. During his stay at Case Institute, Dr. Knox did an extensive study of the absorption of iodine 127 and iodine 129 inside and outside the cavity of a He^3-Ne^{20} laser. In the course of this work, he developed a spectroscopic technique that gave sufficient resolution to observe the actual hyperfine structure (38 lines in all) of iodine 129. Dr. Knox also engaged in a study of the He-Ce laser, high-power CO_2 lasers, the use of cold cathodes in gas lasers, and the design and development of He-Ne lasers for special applications. He joined RCA in September 1970, working on the design and development of a laser deflection display system. His other activities include the design and fabrication of acousto-optic deflectors, modulators, and cavity "dumpers" for visible and infrared lasers. The tellurium dioxide deflectors and latest lead molybdate deflector incorporated in the laser deflection system described were of his design.

Dr. Knox is a member of Tau Beta Pi (Physics and Engineering Honorary), Sigma Xi, the IEEE, and the Optical Society of America.

R. D. Larrabee received the BSEE with Summa Cum Laude honors and the MS in mathematics from Bucknell University in 1953, and the SM and ScD (in Physics) from the Massachusetts Institute of Technology in 1955 and 1957, respectively. While at MIT, he specialized in physical electronics and solid-state physics. He is currently studying for his MBA degree at the Rider College Evening School.

Dr. Larrabee joined the Technical Staff of RCA Laboratories in 1957 and has specialized in research relating to the generation of microwave radiation from bulk semiconductors. He has performed research on negative-effective-mass phenomena, magneto-plasma effects in semiconductors, and on transferred-electron devices. He studied and named the "Oscillistor" effect in germanium and silicon, discovered and characterized a new mode of microwave emission from indium antimonide plasmas, and initiated efforts to understand, characterize, and diagnose the various modes of operation of gallium arsenide transferred-electron devices. He has received two RCA Laboratories Outstanding Achievement Awards for his work in indium antimonide and gallium arsenide. In 1969 he was appointed Sub-Group Head in charge of microwave devices. The following year, he became Research Leader of a group primarily engaged in the development of infrared detectors and arrays for passive thermal imaging. In this position he was responsible for research in a number of diverse areas including Hg-CdTe linear imaging arrays, Pb-SnTe solid-state imaging mosaics, pyroelectric detectors and vidicons, liquid crystal and electro-chemiluminescent display schemes, and the preparation of GaAs by liquid phase epitaxy. In 1972 he became a Senior Engineer in the Applied Physics Group of RCA's Advanced Technology Laboratory where he has specialized in the development of 2-dimensional pyroelectric integrated circuit mosaics for thermal imaging.

Dr. Larrabee is a member of the AAAS, APS, Tau Beta Pi, Phi Mu, and Sigma Xi and a Senior Member of the IEEE. He is listed in American Men and Women of Science.

Jacques I. Pankove obtained his B.S. (1944) and M.S. (1948) degrees from the University of California. He received his doctorate from the University of Paris in 1960 for a study of infrared radiation and germanium. Since 1948, when he joined RCA Laboratories, he has made many contributions to the understanding, technology, and evolution of various semiconductor devices, including large-area photocells and transistors. He has worked in the field of superconductivity, studies of silicon carbide, and investigations of the optical properties of degenerate germanium and the electrical properties of tunnel diodes in germanium, as well as in superconductors and in thin oxide layers. Currently, he is concerned with the study of injection luminescence and laser action in gallium arsenic and other compounds.

Dennis E. Persyk received his B.A. in Physics in 1963, and the M.A. in Physics in 1964 from the University of Wisconsin. He joined RCA Electronic Components, Lancaster, N. J., in June 1965 as an engineer in the Photomultiplier Product Development Activity. Since that time, he has been involved with computer-aided photomultiplier-tube design and development of photomultipliers for laser applications. Presently, he is actively concerned with the development of very fast photomultipliers that utilize negative electron affinity materials. Dr. Persyk became Engineering Leader, Phototube Product Development, in 1972. He is a member of the American Vacuum Society and the Nuclear Instruments and Detectors Committee of the IEEE Group on Nuclear Science.

Dalton H. Pritchard received the BSEE degree, with a major in Electronics, in 1943 from Mississippi State University. Upon graduation he entered the U.S. Army Signal Corps, receiving specialized radar training at Harvard University and at MIT. In 1946, Mr. Pritchard joined RCA Laboratories at Riverhead, New York, where he engaged primarily in research on single-sideband, radio-teletype, multiplex communications systems. In 1950, Mr. Pritchard transferred to the RCA Laboratories at Princeton, New Jersey. For a number of years, he was active in the field of color television, including television systems development, receivers, color kinescopes, transmitting encoders, cameras, and magnetic recording. This work included the planning and testing of systems and circuits proposed for adoption by the National Television Systems Committee (NTSC). More recently, Mr. Pritchard has been engaged in research in the field of information display systems and devices. He is also active in the related fields of vacuum preparation of materials, specialized electron optic devices, lasers, the development of electro-optic materials and techniques for purposes of light control and display, and color-camera special development and evaluation.

Mr. Pritchard is a Senior Member of the IEEE, SID, Sigma Xi, Tau Beta Pi, and Kappa Mu Epsilon and is listed in "American Men of Science" and "Who's Who in the East".

Paul H. Robinson graduated with a Bachelor of Arts in Chemistry, June 1951 from New York University College of Pure Arts and Science and received a Master Degree in Physical Chemistry for Polytechnic Institute of Brooklyn and the Massachusetts Institute of Technology in 1955. He was employed by M.I.T. as a staff member at Lincoln Laboratory from 1952-1959. While at Lincoln Laboratory he was part of a group which was first to determine the oxidation kinetics, thickness, and isosteric heat of adsorption of oxygen on atomically clean germanium surfaces after oxidation. This work was published and presented at the First Conference on Semiconductor Surfaces held in Philadelphia in 1956. He also worked on the electrochemical preparation of manogermane. From 1959 to 1962 he worked at Raytheon's Semiconductor Division Advanced Development Laboratories and was mainly involved with surface studies on silicon and silicon devices. He joined the research staff at RCA Laboratories in February 1962 and developed the closed-spaced technique for the vapor transport of germanium and III-V semiconductors. For the past 7 years he has worked on the epitaxial growth of silicon, silicon device structures, and the characterization of silicon on insulators. He was first to use the silane system for this purpose. He reported along with C. W. Mueller in 1964 the first MOS devices using these films. He also reported the first useful bipolar transistors on insulators using an all epitaxial approach and helped develop a technology for improving minority carrier lifetime in silicon on insulator films. He is a member of the American Chemical Society and the Electrochemical Society.

Ram S. Ronen completed his pre-college education and military service in Israel. He enrolled at the Polytechnic Institute of Brooklyn in 1960, receiving his BSEE, MSEE, and Ph.D. degrees in 1964, 1966, and 1973, respectively. He has lectured at the Polytechnic since 1966. Since 1964, he has been a member of the technical staff at RCA Laboratories, Princeton, N. J. At RCA, he has worked on MOS digital and linear circuits, silicon-on sapphire MOSFET's and bipolar transistors, high frequency and low-noise applications of SOS MOSFET's, and investigation of 1/f noise in MOSFET's. Dr. Ronen is a member of IEEE, Tau Beta Pi, and Eta Kappa Nu.

Howard Sorkin received his B.S. in chemistry from the City College of New York in 1955. He received the M.S. degree and the Ph.D. degree in organic chemistry from Cornell University, Ithaca, N. Y. in 1957 and 1959, respectively. From 1959 to 1968 he was employed as Senior Research Chemist at Airco's Central Research Laboratory, Murray Hill, New Jersey, and worked on a variety of novel polymers and processes. In 1968 Dr. Sorkin joined RCA Solid State Division, Somerville, New Jersey. He has worked in the areas of research and development of liquid-crystal materials and display devices since joining the company.

Dr. Sorkin is a member of the American Chemical Society.